NTNU Trondheim
Norwegian University of Science and Technology
Faculty of Engineering Science and Technology
Department of MarineTechnology

MASTER THESIS IN MARINE TECHNOLOGY

Spring 2019

FOR

Anni Yang Christensen

Analysis of Vortex Induced Motions for Floating Wind Turbines

(Analyse av Vortex Induced Motions for flytende vindturbiner)

Compared with fixed offshore wind turbines, floating offshore wind turbines (FWT) have advantages in terms of economy, convenience of installation, and total capacity. However, they present challenges. Recent studies have highlighted the relevance of vortex-induced motions (VIM), as resonance rigid motions, for FWTs with spar and semi-submersible as floating platforms. When VIM occur on a body with cylindrical parts, the correlation length of the vortex shedding along the body will increase and lead to larger 3D drag and lift forces.
A preliminary project work has been carried out to document the state of the art. Two FWT concepts, a spar and a semisubmersible, have been selected. They were designed to operate with the same wind turbine (the DTU 10 MW Reference wind turbine) and in the same site (West of Barra, Scotland). Relevant environmental conditions of the site were examined. Rough estimations of horizontal-motion natural periods and of the VIM occurrence were carried out. The open-source CFD platform OpenFOAM was selected to study within a strip theory the FWT cross sections. It was applied for the fixed spar cross-section in steady current, in laminar and in turbulent conditions, to assess estimation of the vortex-shedding frequency and other variables.

Objective
The present master thesis aims to investigate the occurrence and features of VIM, as resonance phenomena, for the two selected FWT concepts.

The work should be carried out in steps as follows:

1. Summarize major findings/outcomes from the project thesis and possibly complement the literature survey in order to identify state-of-the-art of the problem. The emphasis should be on the numerical investigations on cases relevant for the present study.
2. Describe the numerical method selected as research tool and its basic assumptions. Perform a systematic study to overcome the numerical issues faced during the project work in turbulent-flow conditions. Use the method to carry on similar studies in steady current for the fixed semi-submersible cross-section, to identify vortex-shedding frequencies and physical features. Investigate the relevance of hydrodynamic interactions of the cylindrical parts of the sub-submersible cross-section.
3. Discuss comparatively the two fixed FWT cross-sections in terms of drag and lift forces in the range of relevant reduced velocities.
4. Perform a systematic study of the VIM possibly for the two FWT cross-sections, each modelled at least as 1-dof in the cross-flow direction under the action of steady current. Discuss the numerical challenges associated with the adopted grid/grids and its/their time evolution.

5. Draw the conclusions from the studies carried out and their results and discuss possible further research steps.

The work may show to be more extensive than anticipated. Some topics may therefore be left out after discussion with the supervisor without any negative influence on the grading.

The candidate should in her report give a personal contribution to the solution of the problem formulated in this text. All assumptions and conclusions must be supported by mathematical models and/or references to physical effects in a logical manner.

The candidate should apply all available sources to find relevant literature and information on the actual problem.

The thesis should be organised in a rational manner to give a clear presentation of the work in terms of exposition of results, assessments, and conclusions. It is important that the text is well written and that tables and figures are used to support the verbal presentation. The thesis should be complete, but still as short as possible. In particular, the text should be brief and to the point, with a clear language. Telegraphic language should be avoided.

The thesis must contain the following elements: the text defining the scope (i.e. this text), preface (outlining project-work steps and acknowledgements), abstract (providing the summary), table of contents, main body of thesis, conclusions with recommendations for further work, list of symbols and acronyms, references and (optional) appendices. All figures, tables and equations shall be numerated.

The supervisor may require that the candidate, in an early stage of the work, present a written plan for the completion of the work. The plan should include budget for the use of computer and laboratory resources that will be charged to the department. Overruns shall be reported to the supervisor.

From the thesis it should be possible to identify the work carried out by the candidate and what has been found in the available literature. It is important to give references to the original source for theories and experimental results.

Supervisor : Marilena Greco
Co-supervisor : Andrea Califano
Co-supervisor : Claudio Lugni
Co-supervisor : Anders Martin Moe

Submitted : January 15th 2019
Deadline : June 11th 2019

Marilena Greco
Supervisor

Preface

This thesis is the result of my final semester of my Master's degree in Marine Technology. The thesis is written at the Institute of Marine Technology at the Norwegian University of Science and Technology in the time period 15th of January 2019 to 11th of June 2019. Vortex induced motion on floating wind turbines with spar and semi-submersible foundations are considered with the used of computational fluid dynamics. Environmental conditions and platform characteristics were first evaluated before numerical analysis were performed. Grid generation is an important part of this work and has taken more time than expected. Both a structural and an unstructured grid is considered for a fixed spar and semi-submersible and dynamic grids are analysed for the spar. This project has been inspiring and the learning outcome has been great.

I would like to thank my supervisors and fellow students for all their support, guidance and help during the project. This work would not have been completed without them.

Firstly, I would like to thank my main supervisor, Marilena Greco, Professor at Department of Marine Technology. Together we defined a scope and an objective for the master thesis. Marilena is a great supervisor, who is engaged in the process and ensure progression. Thank you for all your guidance regarding the topic, critical assessment of my results and constant support both academically and morally.

Secondly, I would like to thank my Co-supervisors Andrea Califano, Claudio Lugni and Anders Martin Moe. Andrea Califano, Principal Engineer at DNV GL, has given me an introduction to OpenFOAM and has been a support when I have faced numerical challenges. Claudio Lugni has been a great support when analysing the results and has contributed with a theoretical foundation. Anders Martin Moe, Project Development Manager at Wood, suggested this topic and provided me with a floating wind turbine concept. I would like to thank all of you for being available for questions and for your valuable replies.

Thirdly, I would like to thank Erin Elizabeth Bachynski, associate professor at Department of Marine Technology and John Marius Hegseth, PhD Candidate at Department of Marine Technology, for providing me with a second floating wind turbine concept and for shearing your knowledge about offshore wind turbines.

A special thanks goes to Mohd Atif Siddiqui, PhD Candidate at Department of Marine Technology, for your precious help regarding OpenFOAM simulations and analysis of the results. Thank you for your time and for letting me sit in your office when I had troubles.

I would also like thank the HPC Group at NTNU for allowing me to use the supercomputer Vilje and Tufan Arslan at the Scientific Computing Group at the IT department at NTNU.

I would further like to thank the great people in my office for making, maybe the toughest semester, the best.

Anni Yang Christensen
Trondheim, June 2019

Abstract

Global warming has been driving the research on renewable energy for years. Wind power is an important contributor among the renewable energy producers and the marked is still growing. The first offshore wind farm was installed in 1991 and was bottom fixed. In 2017 the first floating offshore wind park, Hywind Scotland, started to operate.

Floating structures can experience vortex induced motion (VIM) which can result in large forces and affect the fatigue life of the mooring system. In this project a spar supported and a semi-submersible supported have been studied. The semi-submersible is oriented with two side-by-side cylinders upstream and one cylinder downstream. The two wind turbines are design for the environmental condition at West of Barra, but a larger water depth is assumed.

The current is the most important environmental condition when considering VIM. DNV offshore standards are used to calculate a 50 year return period current profile. The mean of this profile is considered as the maximum current speed that these platforms will experience. This gives a mean current speed on 1.4 m/s for the spar and 2.07 m/s for the semi-submersible. The natural period of the spar and semi-submersible is 128.87 s and 104.17 s.

2D cross-sections of the two platforms are studied with the use of computational fluid dynamic (CFD) and OpenFOAM is chosen as the software. Turbulent flow in the range $7.65 \times 10^5 \leq Re \leq 1.58 \times 10^7$, with turbulence intensity of 1% and a turbulent length scale of 3% of the diameter is studied. A grid convergence study was first preformed for the structural grid generated with blockMesh for a fixed cylinder, but due to numerical challenges an unstructured grid was decided to be more suitable as multiple cylinders also are studied. The unstructured grid was generated with snappyHexMesh for one cylinder before a grid for the semi-submersible was generated. The spar and semi-submersible has been studied as fixed structures and hydrodynamic quantities like C_D, C_L and St are studied, together with the flow features. The effect of low interaction between cylinders has also been studied for the semi-submersible and cancelling effects are observed for the two side-by-side cylinders in the front. The downstream cylinder experiences the largest drag and lift forces. An increase in drag is observe for both structures for increasing Re. This can be a result of the implementation of the wall functions.

Two dynamic grid generation techniques have been tested for the spar supported wind turbine. Decay tests and forced oscillation tests were preformed with two overset grids and one morphing grid. The morphing grid resulted in a natural period of 125 s and the overset grid with an unstructured overset patch resulted in a natural periods of 129.87 s. These two grids are tested with an inlet velocity of $U = 0.4$ m/s which corresponds to a $U_r \approx 3.6$ for both grids. Resonance was observe in both cases as the cylinder oscillates with a period close to the natural period, however the amplitude of oscillation is around 0.7D and higher than expected. The motions are too large for the morphing gird and the flow resolution is suffering from the deformed cells. Most of the free stream simulations are therefore conducted with the overset grid. The lower out-of-lock-in region has been captured and reasonable oscillation amplitudes were obtained. More research is needed on the upper out-of-lock-in region. Two high velocities were tested, but unrealistic high cross-flow amplitudes were observed, due to a large lift force in the transient state. A ramp function and damping was tested and a reduction in the amplitude was observed. However, the grid experiences numerical issues. These issues need to be solved and a grid convergence study should be preformed before the results are reliable and can be validated further.

Sammendrag

Et økende fokus på globale oppvarming har vært den drivende kraften bak forsking på fornybar energi i flere år. Vindkraft er en viktig bidragsyter blant de fornybare energiprodusentene, og markedet for vindkraft er i stadig vekst. Den første offshore vindturbinparken med bunnfaste vindturbiner ble installert i 1991. I 2017 begynte den første flytende offshore vindparken, Hywind Scotland, å operere.

Flytende strukturer kan oppleve bevegelse på grunn av virvelavløsning og dette kan føre til store krefter og påvirke levetiden til forankringssystemet. Dette prosjektet omhandler en spar plattform og en delvis nedsenkbare plattformen som er designet for å være flytende understell for to vindturbiner som skal operere Vest for Barra, utenfor Skottland.

Strømningen i området er den viktigste miljøbetraktningen når bevegelse på grunn av virvelavløsning skal analyseres. DNV offshore standarder har blitt brukt til å regne ut en 50 års strømningsprofil og gjennomsnittsverdien er bruk som en øvre grense for strømningshastigheten. Dette gir en gjennomsnittlig maksimal strømningshastighet på 1.4 m/s for sparen og 2.07 for den delvis nedsenkbare plattformen. Den naturlige egenperioden for sparen og den delvis nedsenkbare plattformen er 128.87 s og 104.17 s.
2D tverrsnittsareal for de to plattformene er studert ved bruk av computational fluid dynamic (CFD) and OpenFOAM er programvaren. Turbulent strømning i området $7.65 \times 10^5 \leq Re \leq 1.58 \times 10^7$, med turbulent intensitet på 1% og turbulent lengde på 3% av diameteren er analysert. En gridkonvergensstudie for en fast sylinder var først gjennomført for et strukturerte grid som ble generert med blockMesh. Numeriske utfordringer førte til at det ble bestemt at et ustrukturert grid ville egne seg bedre spesielt når flere sylindere skal studeres. Det ustrukturerte gridet ble generert med snappyHexMesh for en sylinder før et grid for den delvis nedsenkbare plattformen ble generert. Sparen og den delvis nedsenkbare plattformen ble først studert som fastholdt og hydrodynamiske verdier som C_D, C_L and St ble analysert sammen med strømningskarakteristikken. Effekten av strømningsinteraksjon har også blitt studert for den delvis nedsenkbare plattformen og kanseleringseffekt har blitt observert for løft kreftene for de to sylindrene ved siden av hverandre. Den bakerste sylinderen opplever størst løft og drag krefter. En økning i drag er observert for økende Re for begge strukturer og dette kan være et resultat av implementasjonen av vegg funksjonene.

To dynamiske grid har blitt analysert for spar fundamentet. En fri bevegelses test og en tvungen bevegelses test har blitt utført for å kartlegge egenperioden og tilleggsmassen til systemet. To overlappende grids og et deformerende grid ble testet. Det deformerende gridet ga en egenperiode på 125 s og det overlappende gridet med ustrukturert grid ga egenperiode på 129.87 s. Disse to gridene er testet med innkommende strømningshastighet $U = 0.4$ m/s som korresponderer til $U_r \approx 3.6$ for begge gridene. Resonans ble observert i begge tilfeller da sylinderen svinger med en periode nær den naturlige perioden, men svingningsamplituden er rundt 0.7D og høyere enn forventet. Bevegelsene er for store for det deformerende gridet og de fleste simulieringene med inkommende srøming ble utført med det overlappende gridet. Den nedre lock-in regionen er blitt identifisert og forventede svingningsamplituder ble observert. Det er behov for mer forskning på den øvre lock-in regionen. To høye hastigheter ble testet, men urealistiske høye svingningsamplituder ble observert, på grunn av en stor løftekraft i starten av simuleringen. En rampefunksjon og demping ble testet og en reduksjon i amplituden ble observert. Gridet trenger imidlertid ytterligere tilpasninger, og et grid konvergensstudie bør gjennomføres før resultatene kan valideres ytterligere.

Contents

List of Figures

Nomenclature

Δt	Timestep
Δx	Cell size in x-direction
Δy	Cell size in y-direction
η	Motion
η_1	Surge
η_2	Sway
η_3	Heave
η_4	Roll
η_5	Pitch
η_6	Yaw
η_a	Amplitude of motion
ν	Kinematic viscosity
ω	Turbulence specific dissipation rate
ω_n	Angular natural frequency
ϕ	Phase angle
ρ	Density
A	Area
a	Added mass
A^{2D}	2D added mass
A_{WP}	Water plain area
B	Damping
b	Damping
C	Stiffness
c	Stiffness
C_D	Drag coefficient
C_L	Lift coefficient
$C_{D_{rms}}$	Root-mean-square of drag coefficient
$C_{L_{rms}}$	Root-mean-square of lift coefficient
Co	Courant number
D	Diameter
d	Draft

dt	Timestep
f_0	Natural frequency at zero frequency
F_a	Force amplitude
F_D	Drag force
F_L	Lift force
f_n	Natural frequency
f_v	Vortex shedding frequency
F_x	Force in x-direction
F_y	Force in y-direction
g	Gravity
I	Turbulence intensity
I_{xx}	Second moment of inertia about x-axis
I_{yy}	Second moment of inertia about y-axis
I_{zz}	Second moment of inertia about z-axis
k	Strouhal number
k	Turbulent kinetic energy
k/D	Roughness
M	Mass
m	Mass
m_a	Added mass
m_S	Mass spar
m_T	Mass turbine
R	Stress tensor
r	Radius
Re	Reynolds number
s	Motion of a point on a body
St	Strouhals number
t	Time
T/D	Centre-to-centre transverse pitch ratio
T_0	Natural period at zero frequency
T_v	Vortex shedding period
T_{uL}	Turbulent length scale

U	Free stream velocity
u'	Root-mean-square of turbulent velocity fluctualtions
u_*	Friction velocity at wall
U_c	Current velocity
U_r	Reduced velocity
u_x	Local velocity in x-direction
u_y	Local velocity in y-direction
V	Volume
y^+	Dimensionless wall

Abbreviations

CAD	Computer-Aided Design
CFD	Computational Fluid Dynamics
CFL	Courant–Friedrichs–Lewy
CoG	Centre of Gravity
CoB	Centre of Buoyancy
CPU	Central Processing Unit
FOWT	Floating Offshore Wind Turbine
DES	Detached Eddy Simulation
DNS	Direct Numerical Simulation
DNV	Det Norske Veritas
DoF	Degree of Freedom
DTU	Technical University of Denmark
RWT	Reference Wind Turbine
LES	Large Eddy Simulation
PDS	Power Density Spectrum
RANS	Reynolds-Averaged Navier–Stokes
rms	Root-mean-square
SST	Shear-Stress-Transport
STL	Stereolithography
SWL	Still Water Level
URANS	Unsteady Reynolds-Averaged Navier–Stokes
VIM	Vortex Induced Motion
VIV	Vortex Induced Vibration

Chapter 1

1 Introduction

1.1 Problem Statement

Floating offshore wind turbines (FOWT) are capturing the worlds interest as offshore technology is advancing, and more companies are investing in renewable energy. The world's largest floating wind project, under the name Hywind Scotland, was installed in 2017 by the Norwegian company Equinor. In October 2018, the first part of the installation of the second floating demonstration in Scottish waters, Kincardine, was completed. The Kincardine project is using the semi-submersible foundation windfloat, compared to the Hywind project where floating spar foundations are used.

The global renewable energy generation capacity reached a third of total installed electricity capacity at the end of 2018. Hydropower accounts for the largest share of installed capacity, however the capacity expansions is mostly driven by new installations of solar and wind [8]. Most of the wind power generation today is produced onshore, but the installation of offshore wind turbines are increasing.

The first offshore wind farm was installed in 1991 in Vindeby, Denmark. The wind farm consisted of eleven wind turbines, on monopile foundations, located 2 km from shore in 2-4 m water depth. Europe is today the leading offshore wind turbine market with UK as driving force. 409 new offshore wind turbines, spread across 18 different wind farms, were installed in Europe in 2018 [1]. Figure 1 shows the annual and cumulative installed capacity for some European countries over ten years. An increasing trend is clearly shown.

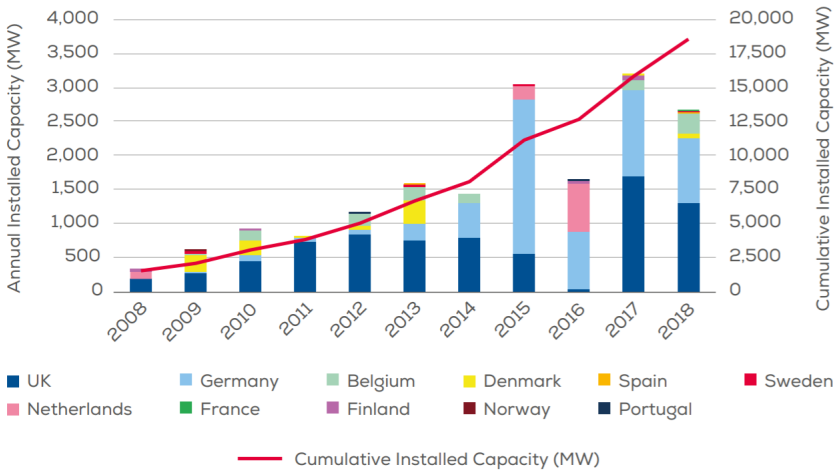

Figure 1: Annual offshore wind installations [1].

Offshore wind turbines have many advantages compared to onshore wind. Larger areas are available offshore for a lower price than onshore. The wind quality is also better at sea, with higher wind velocities and less turbulent wind. This drives the research on larger offshore wind turbine and the average rated capacity of offshore turbines in 2018 was 6.8 MW, 15% larger than in 2017. Onshore turbines has usually a rated capacity on 2.5-5 MW. Transport and installation is also considered easier for offshore wind turbines than for onshore wind turbines.

Most of the offshore wind turbines today are bottom fixed and monopiles represents 74.5% of all in-

stalled foundations in 2018. Other popular bottom fixed foundations are jackets and gravity based foundations. Bottom fixed foundations are considered feasible for shallow water up to approximately 50 m. For countries without a shallow coast line, like Norway and Japan, bottom fixed foundations are a too expensive and various floating wind turbine concepts have been developed for deep water areas. Offshore floating wind turbines is a fast expanding research area.

Deep water installations are also attractive since 80% of the potential offshore wind resources in Europe and 60% of the resources in USA is located at sites with water depth lager than 60 m [28]. In addition, deep water installations further from the coast will benefit the coastal animal life as well as the humans living close to the coast by reducing the noise and visual impact.

Although, offshore wind turbines have many advantages, compared to onshore wind turbines, offshore wind turbines are in general exposed to harsher environmental conditions than onshore installation and larger acting forces needs to be considered in analysis and design.

Offshore wind turbines are designed for large wind power, and the wind induced trust force acting on a floating offshore wind turbine is larger than for conventional offshore platforms. This can cause larger mooring line tension on the upstream side of the wind turbine than on the downstream side. Vortex induced motion (VIM) is a resonant phenomena that can cause additional motion of a floating platform. If VIM is excited under strong wind condition, the impact on the tense mooring chain on the upstream side may be serious. VIM could therefore result in larger forces on the mooring chains for FOWT than for the conventional offshore platforms and should be considered more carefully for these platforms [16]. Most of today's knowledge about VIM is based on research connected to the oil and gas industry. The knowledge about how VIM can affect the global motion and the fatigue life of various FOWT concepts are still insufficient.

1.2 Previous Work

This master thesis contains work that is a continuation of the study conducted in the project thesis and this section will give a brief overview of the previous obtained results. The project thesis includes a literature study of the state-of-the-art on the experimental, theoretical and numerical research on VIM for floating platforms, a study of the environmental conditions in a selected sea region suitable for offshore wind and a convergence study of a circular cylinder in laminar conditions, representing a spar cross section, in current. Preliminary results for a cylinder in turbulent conditions was included, but this work was not finished during this project.

The VIM study was decided to be done in 2D and by the use of CFD and OpenFoam. A structured mesh was made with blockMesh and laminar convergence study was conducted for Re = 100. In this laminar study a pisoFoam solver was used. The study included a mesh refinement study, a domain size dependence study and a timestep dependence study. The convergence study with a laminar case resulted in a $C_D = 1.5$, $C_L = 0.26$ and St = 0.18. The C_D was a little high compared to $C_D \approx 1.3$ which was the result found in the literature. St was close to the results found in literature and not far from the theoretical St = 0.2.

Turbulent simulations were conducted with a pimpleFoam solver and k-ω SST model. The Re for these simulations was $7.65 \cdot 10^6$, the turbulent intensity was 1% and the effect of the turbulent length scale was tested. The results are given in Table 1. The turbulent length scale was chosen as a percentage of the cylinder diameter. 2%, 3% and 4% was tested and a small increase in drag for increasing turbulent length scale was observed.

Table 1: Effect of turbulence length scale.

U [m/s]	k [m^2/s^2]	ω [1/s]	I [%]	T_{u_L} [m]	ν [m^2/s]	C_D [-]	C_L [-]	St [-]
1	1.5E-4	0.04374	1	0.28(2%)	1.83E-6	0.7962	0.6248	0.266
1	1.5E-4	0.02916	1	0.42(3%)	1.83E-6	0.7984	0.6271	0.266
1	1.5E-4	0.02187	1	0.56(4%)	1.83E-6	0.7992	0.6292	0.266

As only small variations was observed a turbulent length scale on 3% was chosen for further work. The turbulent simulations requires a much finer mesh than the laminar case and the computational time was high. A convergence study was therefore not completed, but the results indicates the starting point for the work in this master thesis.

1.3 Structure of the Thesis

The rest of the thesis is organized as follows:

Chapter 1 is an introduction to the background and the motivation for this work. A brief summary of previous work and results are also given in this chapter.

Chapter 2 gives an overview of the relevant theory behind flow around circular cylinders. Some theory of rigid body dynamics and the equation of motion is also given in this chapter. Theory regarding free and forced oscillations are briefly covered.

Chapter 3 gives a description of the used numerical method. The turbulent model, y^+, CFL condition and boundary conditions are discussed.

Chapter 4 gives an overview of the different grid generation methods used in this work. Unstructured grids, structured grids and overset grids are discussed, and strengths and weaknesses with the different methods are described.

Chapter 5 gives an estimation of the current profile and expected current velocities at the site. The two concepts are also presented in this chapter together with the results from a calculation of the natural frequencies of the spar supported wind turbine. A rough calculation of VIM occurrence for the two platforms are also given in this chapter.

Chapter 6 shows the results obtained with two different grids for one cylinder in turbulent flow. The results are discussed and an unstructured grid is chosen for further study.
Chapter 7 shows the results for an unstructured grid for the semi-submersible. An analysis of the flow features and hydrodynamic interaction between the cylinders in the semi-submersible are presented.

Chapter 8 gives the results for the spar and semi-submersible for Re in the range $3.06 \times 10^6 \leq Re \leq 1.58 \times 10^7$. A comparison between the two platforms are also presented.

Chapter 9 presents an analysis of dynamic grid generation techniques. The performance of two overset grids and one morphing mesh are analysed based on decay tests and forced oscillation tests.

Chapter 10 gives the results for a cross-flow analysis of the spar platform. A morphing mesh and an overset grid are used and the inlet velocities in the range from $U = 0.1$ m/s to $U = 2.5$ m/s are tested.

Chapter 11 presents a discussion of the assumptions and approach used in this work.

Chapter 12 gives a conclusion on the presented work.

Chapter 13 presents suggestions for further work based on the findings and challenges encountered during this project.

Chapter 2

2 Theory

The relevant background theory that sets the foundation of this work will be presented in this section. Only theory that is necessary for the understanding of the work and theory directly used in this thesis will be presented. The theory concerns flow around circular cylinders and rigid body dynamics for one or more degrees of freedom.

2.1 Flow Regimes and Vortex Shedding

Flow regimes around a smooth cylinder in steady current can be defined based on the Reynolds number. The Reynolds number is defined as:

$$Re = \frac{UD}{\nu} \tag{1}$$

where U is free stream velocity, D is cylinder diameter and ν is kinematic viscosity. The Reynolds number is one of the main parameters that is used to characterise a flow. Zdravkovich [46] defines four flow regimes for low Re: Creeping regime ($0 < Re < 4$), steady separation regime ($4 < Re < 48$), periodic vortex shedding regime ($48 < Re < 180$) and transition-in-wake regime ($180 < Re < 400$). Faltinsen [14] defines four flow regimes for high Re: subcritical flow ($\approx 2 \times 10^5 >$ Re), critical flow ($\approx 2 \times 10^5 <$ Re $<\approx 5 \times 10^5$), supercritical flow ($\approx 5 \times 10^5 <$ Re $<\approx 3 \times 10^6$) and transcritical flow ($\approx 3 \times 10^6 <$ Re).

Vortex shedding occurs due to separation of the flow. For a cylinder a symmetric wake picture develops first, before instabilities makes the wake asymmetric. This results in an alternating vortex shedding and the development of a vortex street behind the cylinder.

The development of the vortex street behind a cylinder depends on the Re. A laminar vortex street is observed for $40 < Re < 200$. The vortex shedding is two-dimensional, i.e., the shedding does not vary in the spanwise direction [43]. A transition from laminar to turbulent wake region occurs when Re increase. The transition region moves towards the cylinder as Re increase in the range $200 < Re < 300$ [7]. At $Re > 300$ the formed vortices are turbulent and the vortex shedding becomes three-dimensional.

For an idealised vortex street the non-dimensional vortex shedding frequency can be represented by the Strouhal number, St:

$$St = \frac{f_v D}{U} \tag{2}$$

where D is cylinder diameter, U is the free stream velocity and f_v is vortex shedding frequency which is defined as:

$$f_v = \frac{1}{T_v} \tag{3}$$

where T_v is vortex shedding period. A well known graph of the Strouhal number as a function of Re for various roughness was presented by Achenbach and Heinecke in 1981 and is given in Fig. 2.

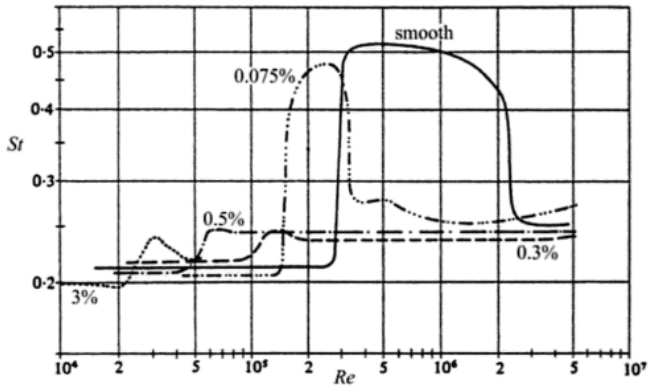

Figure 2: Strouhal numbers for flow past circular cylinders in terms of Re for various roughness. 0.075% corresponds to $k/D = 7.5 \times 10^{-4}$, 0.3% corresponds to $k/D = 3 \times 10^{-2}$, 0.5% corresponds to $k/D = 9 \times 10^{-3}$ and 3% corresponds to $k/D = 3 \times 10^{-2}$ [3].

Vortex shedding causes oscillatory lift and drag on the body, due to the alternating pressure. The lift force on a circular cylinder in uniform flow with vortex shedding will oscillate with a mean value equal zero, while the drag force for the same case will oscillate around a mean value different from zero. The lift force oscillates with the same frequency as the vortex shedding frequency and the drag oscillates with twice the vortex shedding frequency. The lift and drag force amplitudes are normally expressed in terms of lift and drag coefficients:

$$C_L = \frac{F_L}{\frac{1}{2}\rho U^2 D} \qquad\qquad C_D = \frac{F_D}{\frac{1}{2}\rho U^2 D} \tag{4}$$

where F_L and F_D are the lift and drag forces and ρ is the fluid density. Numerous studies has been done to quantify the lift and drag coefficient in terms of Re. For high Re most of the reliable research has been done experimentally in wind tunnels. The root-mean-square (rms) of the lift coefficient from various experiments is given in Fig. 3 and the drag coefficient for various roughness is given in Fig. 4.

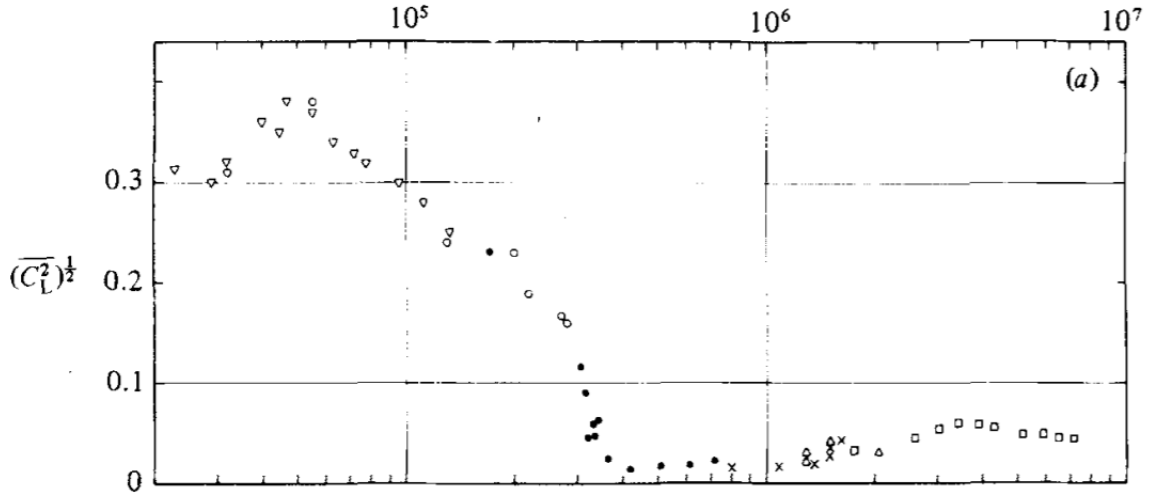

Figure 3: Rms of lift coefficient for circular cylinders in terms of Re [34].

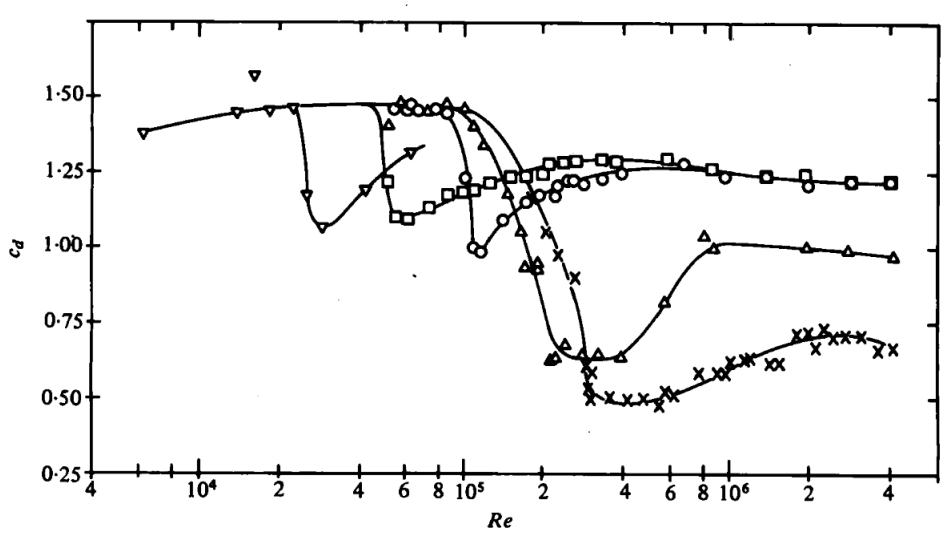

Figure 4: Drag coefficient for circular cylinders in terms of Re for various roughness. $\times$, smooth, $\triangle$, $k/D = 75 \times 10^{-5}$; $\bigcirc$, $k/D = 300 \times 10^{-5}$; $\square$, $k/D = 900 \times 10^{-5}$, $\bigtriangledown$, $k/D = 3000 \times 10^{-5}$ [3].

2.2 Correlation Length

For $Re > 300$ the vortices are turbulent and they are not shed uniformly along the cylinder length. Instead, the vortices are shed in cells in the spanwise direction. The vortex shedding in the cells can be out of phase and the maximum resultant force acting on the cylinder may be smaller than the force acting on the cylinder over the length of a single cell. The average cell length is referred to as the correlation length. The correlation length change with Re for a smooth cylinder. For low Re, where the vortex shedding is two-dimensional, the correlation length should theoretically be infinite. This is not achieved in practice due to existing end conditions. The correlation length increases considerably when the cylinder is oscillated in cross-flow direction.

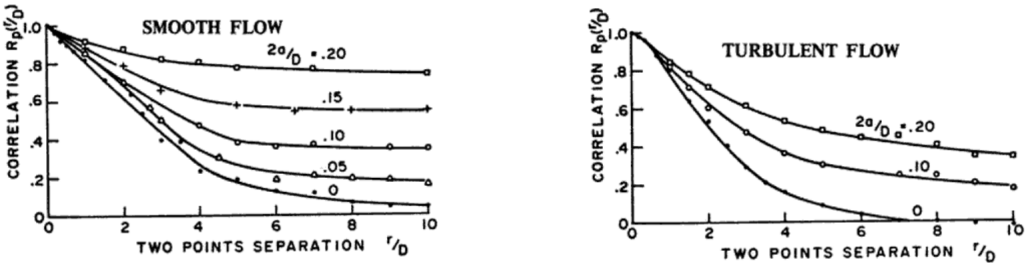

Figure 5: Effect of cross-flow cylinder vibration on correlation coefficient of surface pressure fluctuation for a smooth cylinder in laminar and turbulent flow [25].

Novak and Tanaka [25] observed that the correlation length increased from about 3.5D to more than 40D when the cylinder vibrated in smooth flow. In turbulent flow the correlation length increased from 2.4D to 10.4D. The rapid increase of correlation length started as the amplitude of oscillation reached 5% of cylinder diameter.

2.3 Boundary Layer Theory

In the boundary layer the flow can be either laminar, turbulent or change between these two. For turbulent flows the boundary layer can be divided into three parts: viscous sublayer, buffer layer and log layer. Viscous forces are important in the boundary layer and the boundary layer thickness can be defined as the normal distance from the wall to a point where the tangential velocity in the fluid is 99% of the local free stream velocity. If backflow occurs in the boundary layer the flow will separate from the body and the separation angles are often of interest. The flow field close to the separation point is shown in Fig. 6. The separation happens in the point, S, where there is backflow on the downside and no backflow on the upside. In this point Eq. 5 is true.

$$\frac{\partial u}{\partial y} = 0 \tag{5}$$

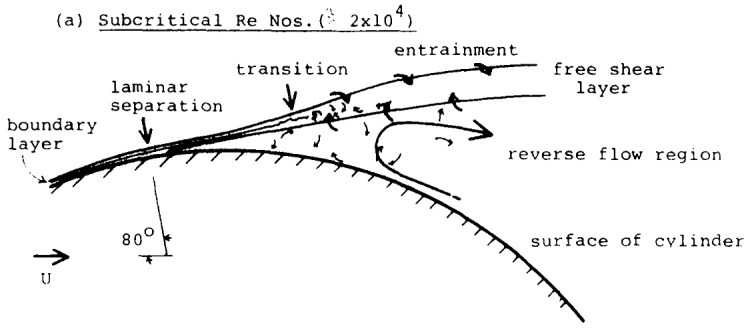

Figure 6: Flow field near separation point [6].

.

In laminar boundary layers the angles of separation is approximately $\pm 80°$, measured from forward stagnation point. For turbulent boundary layers the separation point moves downstream and for supercritical and transcritical flow the angles of separation is approximately $\pm 120°$. For subcritical and critical flows the boundary layer might not be fully turbulent and a point of instability defines where the boundary layer change from laminar to turbulent. The point of instability is located ahead of the separation point. Figure 7 shows the angle of separation in terms of Re for various roughness numbers.

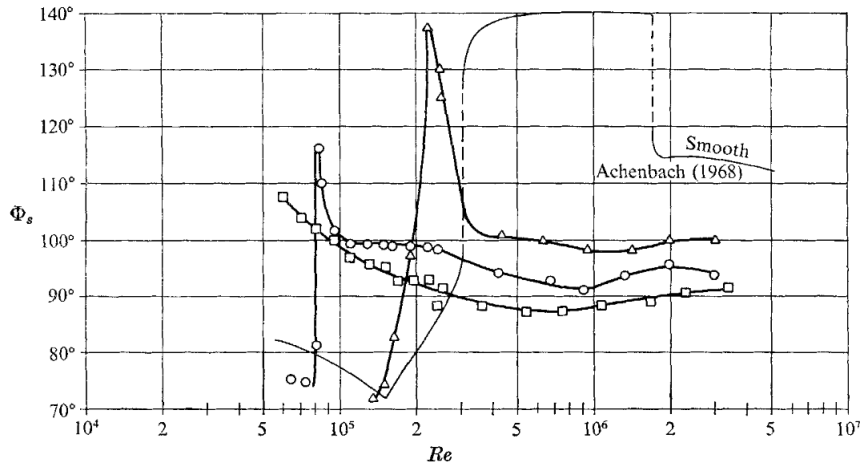

Figure 7: Separation angle in terms of Re. △, $k/D = 110 \times 10^{-5}$; ◯, $k/D = 450 \times 10^{-5}$; □, $k/D = 900 \times 10^{-5}$ [2].

2.4 VIV

VIV is associated with cross-flow past circular cylinders and an important parameter for a given natural frequency, f_n, is the reduced velocity, U_r, given by:

$$U_r = \frac{U}{f_n D} \tag{6}$$

where U is the current speed and D is the cylinder diameter. A rough condition for VIV occurrence is given by $U_r = 1/St = 5$ for $St = 0.2$. Empirical guidelines are established for VIV on circular cylinders in cross-flow. Figure 8, from DNV guidelines [11], shows the cross-flow VIV amplitude as a function of reduces velocity for a straight circular cylinder.

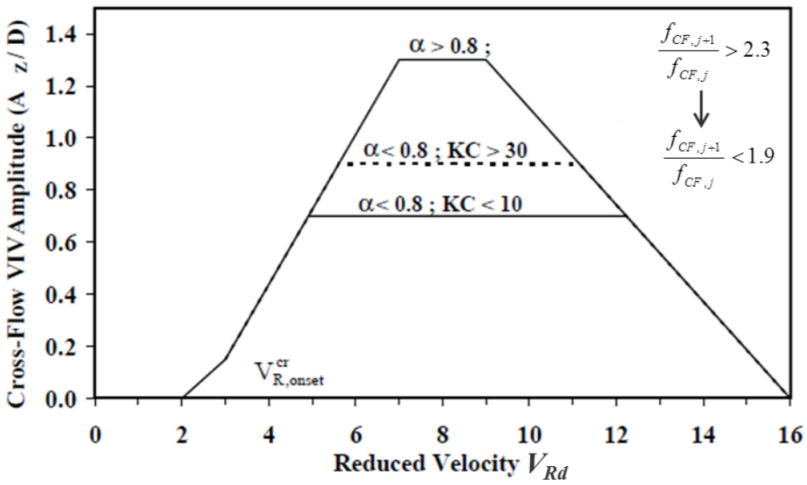

Figure 8: DNV guidelines for cross-flow VIV [11]. $\alpha = \frac{U}{U+U_w}$ is the current flow velocity ratio, U is the current speed, U_w is the incident wave-velocity along the current direction. $V_R = \frac{U}{f_n D}$ is the reduced velocity, f_n is the natural frequency and D is the diameter. A_z is the cross-flow VIV amplitude.

2.5 Free Stream Turbulence

The free stream is usually turbulent in most practical applications. Turbulence is a way of quantifying the level of randomness in a flow. Turbulence can be statistically quantified by the intensity and scale of turbulence.

Turbulence can be described as instability of laminar flows that occurs when Re increases. Turbulence is nearly an intractable problem due to the randomness and non-linearity features. Turbulent flows consists of 3D eddies of various size and the 3D vorticity fluctuations sets limitations for the use of 2D simulations.

The turbulence intensity can have a significant effect on the lift and drag coefficient. Cheng and Melbourne [10] studied this for supercritical flow.

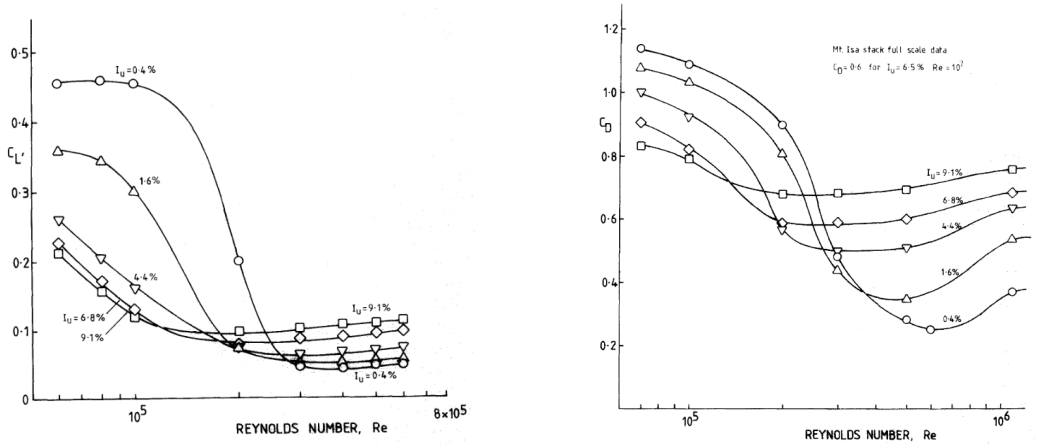

Figure 9: Variation in fluctuating lift and mean drag with T_i and Re [10].

2.6 Rigid Body Dynamics

The dynamics of rigid bodies and fluid motions are governed by the combined actions of different external forces, moments and the bodies inertia. In the following sections background theory considering loads superposition and hydrodynamic loads will be discussed in the view of a single linear mass-spring system.

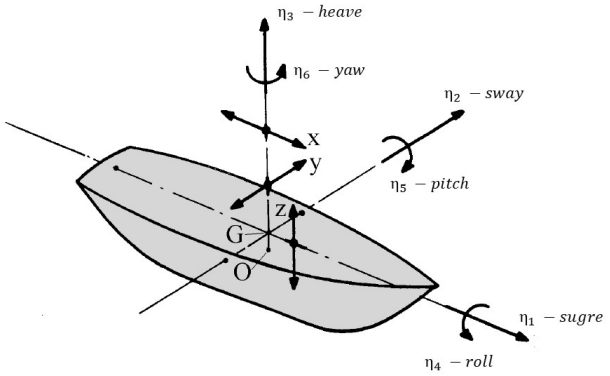

Figure 10: Definition of body motion in six degree of freedom [20].

2.6.1 Loads Superposition

A real structure that operates in the ocean is exposed to irregular waves. The results in irregular sea can be obtained by linearly superposing results from regular wave components. The hydrodynamic problem in regular waves is usually divided into two sub-problems:

A: The diffraction problem.
In this problem the body is restrained, while exposed to regular waves. The hydrodynamic loads that acts on the body in this condition are called wave excitation loads and are composed of Froude-Kriloff and diffraction forces and moments.

B: The radiation problem.
In this problem the body is forced to oscillate with the wave excitation frequency in any rigid body mode. There are no incident waves and the hydrodynamic loads that acts on the body are identified as added mass, damping and restoring forces.

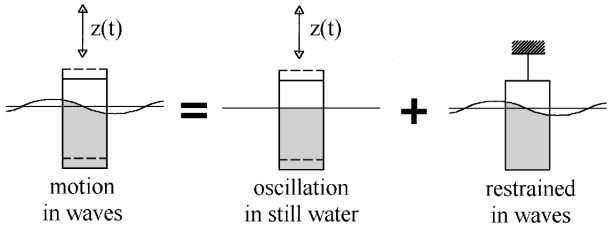

Figure 11: Superposition of hydromechanical and wave loads [20].

Figure 11 shows the two problems and the total hydrodynamic forces is found by adding the forces obtained in A and B. The motion of any point on the body can be written as:

$$\mathbf{s} = \eta_1 \mathbf{i} + \eta_2 \mathbf{j} + \eta_3 \mathbf{k} + \boldsymbol{\omega} \times \mathbf{r} \tag{7}$$

where η_i represent translatory displacements in x-, y- og z-direction so that η_1 is the surge, η_2 is the sway and η_3 is the heave displacement. This can also be seen in Fig. 10. $\times$ denotes the vector product between $\boldsymbol{\omega}$ and $\mathbf{r}$ where:

$$\boldsymbol{\omega} = \eta_4\mathbf{i} + \eta_5\mathbf{j} + \eta_6\mathbf{k} \quad \mathbf{r} = x\mathbf{i} + y\mathbf{j} + z\mathbf{k} \tag{8}$$

η_4, η_5 and η_6 is the angular displacement of the rotational motion about the x-, y- and z-axis. η_4 is defined as the angle in roll, η_5 the angle in pitch and η_6 the angle in yaw as shown in Fig. 10. $\mathbf{i}$, $\mathbf{j}$ and $\mathbf{k}$ are unit vectors along x-, y- and z-axis and the motion can be rewritten as:

$$\mathbf{s} = (\eta_1 + z\eta_5 - y\eta_6)\mathbf{i} + (\eta_2 - z\eta_4 + x\eta_6)\mathbf{j} + (\eta_3 + y\eta_4 - x\eta_5)\mathbf{k} \tag{9}$$

η_i where $i = 1, ..., 6$ do not need to be translatory or rotational motions of the center of gravity of the body, e.g for floating wind turbines there is a common practise to calculate motions according to a global coordinate system located at still water level.

Added mass and damping can be found by studying the radiation problem. The forced motion of the structure generates outgoing waves that results in oscillating fluid pressure on the body surface. The resulting forces and moments on the body can be found through integration of the fluid pressure forces over the body surface. The hydrodynamic added mass and damping loads due to harmonic motion mode η_j can formally be written as:

$$F_k = -A_{kj}\frac{d^2\eta_j}{dt^2} - B_{kj}\frac{d\eta_j}{dt} \tag{10}$$

A_{kj} and B_{kj} are added mass and damping coefficients. By Green's second identity, it can be shown that $A_{kj} = A_{jk}$ and $B_{jk} = B_{kj}$ if no current is present and the structure has no forward speed.

For the case where the body motion are studied for very high frequencies ($\omega \to \infty$) or for very small frequencies ($\omega \to 0$), the body cannot generate any free-surface waves and the damping will be zero. For these two cases only the added mass coefficients needs to be calculated.

2.6.2 Strip Theory

Strip theory states that the total 3D force acting on a body is equal to the sum of 2D forces action on strips of the body. For an uniform body the total force is found by integrating the 2D force over the length of the body. This makes 2D simulations of 3D bodies possible.

The 2D added mass coefficient for a circular cylinder is well know to be:

$$A^{2D} = \rho A \quad \text{where} \quad A = r^2\pi \tag{11}$$

The force in sway on a strip can be written as:

$$dF_2(z) = -A_{22}^{2D} \cdot \ddot{s}_2(z) \quad \text{where} \quad \ddot{s}_2(z) = \ddot{\eta}_2 - z\ddot{\eta}_4 \tag{12}$$

By using the expression for $\ddot{s}_2(z)$, $dF_2(z)$ can be divided into two parts due to the two motions:

$$dF_2(z) = dF_{22}(z) + dF_{24}(z) \tag{13}$$

where

$$dF_{22}(z) = -A_{22}^{2D}\ddot{\eta}_2 \quad \text{and} \quad A_{22}^{2D}z\ddot{\eta}_4 \tag{14}$$

according to Eq. 12. The total force can be found by integrating the 2D force over the draft.

$$F_{22}(z) = \int_a^b dF_{22}(z)dz = -\int_a^b A_{22}^{2D} dz\ddot{\eta}_2 \tag{15}$$

By comparing Eq. 15 and Eq. 10 the 3D added mass coefficient can be written as:

$$A_{22} = F_{22}(z) = \int_a^b A_{22}^{2D} dz \tag{16}$$

The restoring forces and moments for a freely floating body are found by hydrostatic and mass consideration. The force and moment components can be written as:

$$F_k = -C_{kj}\eta_j \tag{17}$$

where C_{kj} is the restoring coefficient. Only a few stiffness coefficients are non-zero for a submerged cylinder which has the x-z plane as a symmetry plane. Those are:

$$C_{33} = \rho g A_{WP} \tag{18}$$

$$C_{44} = \rho g V(z_B - Z_G) + \rho g \iint y^2 ds = \rho g V \overline{GM}_T \tag{19}$$

$$C_{55} = \rho g V(z_B - Z_G) + \rho g \iint x^2 ds = \rho g V \overline{GM}_L \tag{20}$$

where A_{WP} is the water plane area, V is displaced water volume, z_B and z_G is the z-coordinate for center of gravity and center of buoyancy.

The equations of rigid body motions can be written as:

$$\sum_{k=1}^{6} = [(M_{jk} + A_{jk})\ddot{\eta}_k + B_{jk}\dot{\eta}_k + C_{jk}\eta] = F_j e^{-i\omega_e t} \qquad (j = 1, ..., 6) \tag{21}$$

where M_{jk} are the components of the generalized mass matrix, A_{jk} are the components of the added mass matrix, B_{jk} are the components of the damping matrix and C_{jk} are the components of the stiffness matrix. F_j are the complex amplitudes of the exiting force and moment-component, where the force and moment-component is given by the real part of $F_j e^{-i\omega_e t}$. Equation 21 is written for steady-state sinusoidal motion by using the equations of linear and angular momentum.

For a structure that has symmetry about the x-z plane and center of gravity at $(0, 0, z_g)$ the generalized mass matrix is written as:

$$M = \begin{bmatrix} M_{11} & 0 & 0 & 0 & M_{15}z_g & 0 \\ 0 & M_{22} & 0 & -M_{24}z_g & 0 & 0 \\ 0 & 0 & M_{33} & 0 & 0 & 0 \\ 0 & -M_{42}z_g & 0 & I_{44} & 0 & -I_{46} \\ M_{51}z_g & 0 & 0 & 0 & I_{55} & 0 \\ 0 & 0 & 0 & -I_{46} & 0 & I_{66} \end{bmatrix}$$

where I_{jk} is the moment of inertia and $M_{jk} = M$.

2.7 One Degree of Freedom System

2.7.1 Free Decay

In a free decay test a mass connected to a spring is displaced and released and the motions are let to die out freely. The vertical motions are determined by the solid mass and the hydrodynamic loads. A single degree of freedom (DoF) system can be modelled as a mass-spring system, as shown in Fig. 12.

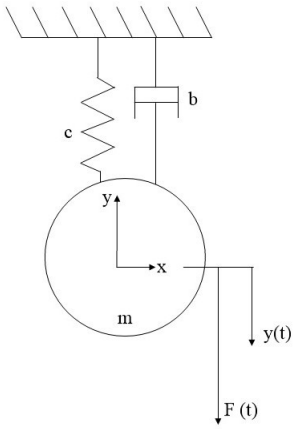

Figure 12: One degree of freedom system.

The equation of motion for this system can be written as:

$$(m+a)\ddot{y}(t) + b\dot{y}(t) + cy = F(t) \tag{22}$$

where m is the mass of the system, a is the added mass, b is the damping coefficient and c is the spring stiffness coefficient. y(t) is the systems horizontal displacement from equilibrium and F(t) is an external load action on the system. $F(t) = 0$ for a system that is free to vibrate and the solution to this second order differential equation can be written as:

$$y(t) = Y_1 e^{\lambda_1 t} + Y_2 e^{\lambda_2 t} \tag{23}$$

where Y_1 and Y_2 are constants and $\lambda_1 = \sigma + i\omega$ and $\lambda_2 = \sigma - i\omega$. By using Eq. 23 to describe the free response and substitute $y(t) = Ye^{\lambda t}$. Eq. 22 can be written as:

$$(m+a)\lambda^2 Y e^{\lambda t} + b\lambda Y e^{\lambda t} + bY e^{\lambda t} = 0 \tag{24}$$

$$((m+a)\lambda^2 + b\lambda + c)Y e^{\lambda t} = 0 \tag{25}$$

$$((m+a)\lambda^2 + b\lambda + c)y = 0 \tag{26}$$

m, a, b, c, λ and Y do not depend on time and Eq. 26 is true for all times. The non-trivial solution to this equation is:

$$\lambda_{1,2} = -\frac{B}{2(m+a)} \pm \frac{1}{2}\sqrt{\left(\frac{b}{2(m+a)}\right)^2 - \frac{c}{(m+a)}} \tag{27}$$

for an undamped system, $b = 0$:

$$\lambda_{1,2} = - \pm i\sqrt{\frac{c}{(m+a)}} = -i\omega_n \tag{28}$$

where ω is the angular natural frequency, given in radians per second, of the system. This shows that the angular natural frequency of an undamped, free vibrating one DoF system is written as:

$$\omega_n = \sqrt{\frac{c}{(m+a)}} \tag{29}$$

The natural period is found as:

$$T_n = \frac{2\pi}{\omega_n} = 2\pi\sqrt{\frac{(m+a)}{c}} \tag{30}$$

2.7.2 Forced Oscillation

Forced oscillation tests can be used to find the hydrodynamic damping and added mass of a system. For a free decay test in sway in x-y plain the vertical motion of the model is defined by:

$$y(t) = y_a sin(\omega t) \tag{31}$$

and the sway forces acting on the body are:

$$F_y(t) = F_a sin(\omega t + \phi) \tag{32}$$

and the linear equation of motion is given by:

$$(m+a)\ddot{y} + b\dot{y} + cy = F_a sin(\omega t + \phi) \tag{33}$$

By substituting Eq. 31 in to Eq. 33 one can obtain the added mass, damping and stiffness as:

$$a = \frac{c - F_a cos(\phi)}{y_a \omega^2} - m \tag{34}$$

$$b = \frac{F_a sin(\phi)}{y_a \omega} \tag{35}$$

$$c = \rho g A_w \tag{36}$$

2.8 Multiple Degree of Freedom System

For a multiple degree of freedom system, the equation of motion becomes a matrix equation:

$$(\mathbf{M} + \mathbf{A})\ddot{\eta} + \mathbf{B}\dot{\eta} + \mathbf{C}\eta = 0 \tag{37}$$

where $\mathbf{M}$, $\mathbf{A}$, $\mathbf{B}$ and $\mathbf{C}$ are matrices and η is a vector. The solution to this equation is assumed to be:

$$\eta = \eta_a cos(\omega t + \phi) \tag{38}$$

This assumption is valid for a system that oscillate with harmonic motion at the frequency ω and with phase angle ϕ. By assuming no damping and substituting Eq. 38 into Eq. 37 the characteristic equation is found as:

$$(-\omega^2(\mathbf{M}+\mathbf{A})+\mathbf{C})\eta_a = 0 \tag{39}$$

where η_a is a vector of unknown complex constant. For an uncoupled system the mass and stiffness matrix are diagonal and each DoF can be treated separately as one DoF systems. The angular natural frequency for any of the DoF is given by Eq. 29.

For a coupled system, the mass and stiffness matrix will not be diagonal as the matrices will include coupled terms. Eq. 39 can then be solved as:

$$det(-\omega^2(\mathbf{M}+\mathbf{A})+\mathbf{C}) = 0 \tag{40}$$

This equation is a bit tedious to solve by hand, but it can quickly be solved in e.g. MATLAB by using the eigenvalue function. ω^2 is solved as $\omega^2 = (\mathbf{M}+\mathbf{A})^{-1} \cdot \mathbf{C}$

2.9 Center of Gravity and Moment of Inertia for Complex Structures

Moments of inertia for parts of a body can only be added together if they have the same axis of rotation. The moment of inertia are generally given relative the center of gravity of a shape. The shapes usually have different centre of gravity (CoG) and the moment of inertias cannot be added together since they have not been calculated for the same axis of rotation. The parallel axis theorem can be used to adjust the different parts moment of inertia so they are taken about the same point.

The parallel axis theorem states that the moment of inertia about a point O for a body equals the moment of inertia about CoG plus an added moment of inertia due to distance between O and CoG:

$$I_O = I_{CoG} + md^2 \tag{41}$$

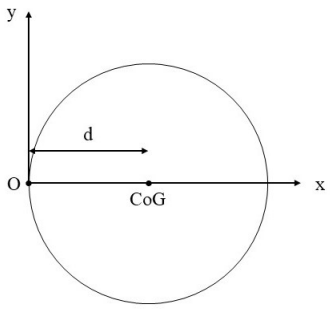

Figure 13: Parallel axis theorem.

The global moment of inertia for a system is usually taken about the global CoG or at still water level. The global CoG according to SWL can be found by:

$$z = \frac{m_1 \cdot z_1 + m_2 \cdot z_2 + ... + m_n \cdot z_n}{m_1 + m_2 + ... + m_n} \tag{42}$$

where m_i is the mass of part i, $i = 1, 2, ..., n$, and z_i is the distance from CoG for part i and to a reference point.

Chapter 3

3 Software and Method

3.1 OpenFOAM

OpenFOAM is a software to solve computations fluid dynamic (CFD) problems. The software is an open source library developed by OpenCFD Ltd., to solve fluid flows and heat transfer problems. OpenFOAM is an acronym and stands for Open Source Field Operation and Manipulation. The software consist of a large number of numerical solvers in addition to both pre- and post-processing utilities.

For new users, OpenFOAM provides many tutorials that can be used as starting points when setting up new cases. OpenFOAM does not come with a graphical user interface, but Paraview is commonly used for graphical visualisation. A case in OpenFOAM consists of a number of text files, located in a project directory and the case is executed from the terminal. Appendix X shows examples on a controlDict, run script, snappyHexMeshDict and dynamicMeshDict that are used in this project. Adjustments are manually done in a text editor and the learning curve of OpenFOAM is therefore steeper than most other CFD-software.

OpenFoam uses implicit schemes. Implicit schemes are more robust and the Courant number, Co, is not a critical measure of stability. However, Co serves as a measure of accuracy since stability does not imply accuracy. The Courant number will be discussed more in Section 3.4.

3.1.1 Solvers

Various solvers are applicable in OpenFOAM, but only the ones used in this work will be discussed in this section.

pisoFoam is a transient solver for incompressible, Newtonian, laminar/turbulent flow that uses the PISO (Pressure-Implicit with Splitting of Operators) algorithm to solve the continuity equation:

$$\nabla \cdot \mathbf{U} = \mathbf{0} \tag{43}$$

and the momentum equation:

$$\frac{\partial \mathbf{U}}{\partial t} + \nabla \cdot (\mathbf{U}\mathbf{U}) - \nabla \cdot \mathbf{R} = -\nabla \mathbf{p} \tag{44}$$

where $\mathbf{U}$ is velocity, $\mathbf{p}$ is kinematic pressure, $\mathbf{p} = \mathbf{p}/\rho$, and $\mathbf{R}$ is a stress tensor.

pimpleFoam is a transient solver for incompressible, Newtonian, laminar/turbulent flow that uses the PIMPLE algorithm. The PIMPLE algorithm is a combination of the PISO and SIMPLE (Semi-Implicit Method for Pressure-Linked Equations) algorithms. The PIMPLE algorithm gives better stability than PISO, when considering large timesteps where the maximum Courant number is above 1. PIMPLE also solves Eq. 43 and Eq. 44, but with an extra momentum source, S_U, term on the right hand side of Eq. 44. pimpleFoam is also applicable on moving meshes where morphing of the mesh is used to account for the motion. For overset grids the overPimpleDyMFoam solver is used.

sixDoFRigidBodyMotion is a motion solver that can be used together with pimpleFoam or overPimpleDymFoam. This solver is used for problems were free rigid body motions are solved. The motion solver is defined in the DynamicMeshDict together with system properties, constrains and restrains. Mass, center of mass and moment of inertia are examples of system properties that must be defined. Constrains controls directly the permitted motion of the body. E.g. the constrain axis controls

which axis the body can rotate about and the constrain line controls the direction of the linear motion.

multiSolidBodyMotionSolver is a motion solver that can be used to solve forced body motion. For harmonic motion only the amplitude and the angular frequency needs to be specified. This might make the multiSolidBodyMotionSolver easier to implement than the sixDoFRigidBodyMotion solver.

3.2 Turbulence Models

Both pisoFoam and pimpleFoam are applicable with laminar, Reynolds Averaged Navier-Stokes (RANS), Large-Eddy Simulation (LES) or Detached-Eddy Simulation (DES) models in OpenFOAM. Laminar uses no turbulence model while RANS, LES and DES are different turbulent models for solving the Navier-Stoke equation.

Large-Eddy Simulation is less sensitive to turbulent modelling errors since only small sub-grid scales of motion are modelled, however the computational cost of resolving the turbulent boundary layers is high and limits LES to moderate Reynolds numbers. Wall functions are applicable with LES since sufficient resolution is usually not possible.

RANS gives time average values and cannot resolve the vortex structures as accurate as LES. RANS also assumes full turbulence and cannot be used for flows in laminar-turbulent transition regime. RANS has low computational demand compared to LES and can be used for complex geometries. RANS can be highly useful for engineering applications when combined with empirical information.

Another sub-model has to be used when modelling turbulence with RANS or LES and two equation eddy-viscosity turbulence models are the most used models today. $k-\epsilon$ model is a widely used, robust and cheap model. One of the models drawbacks is the lack of sensitivity to adverse pressure gradients and therefore predicts too high shear-stress levels, thus delays or prevents separation. Another problem is numerical stiffness of the equations when integrated through the viscous sublayer.

$k-\omega$ is an alternative model to $k-\epsilon$ that preforms significantly better under adverse pressure gradient conditions. However, this model depends strongly on the freestream values that are specified outside the shear-layer. To overcome this major shortcoming F. R. Menter [24] proposed the $k-\omega$ SST model which is independent of the free steam values, and has shown good agreements with experimental data for adverse pressure gradient boundary layer flows. The shortcomings of this model is the wall distance dependence which makes the model less suitable for free shear flows, compared with standard $k-\omega$. Compared to $k-\epsilon$, $k-\omega$ SST can be a little more challenging to implement and requires more computational time. However, the accuracy is significantly better as the model performs better regarding separation and vortex shedding. The $k-\omega$ SST model is therefore used in this project. In OpenFOAM the $k-\omega$ formulation in the inner parts of the boundary layer makes the model directly unstable all the way down to the wall, through the viscous sub-layer. This allows the $k-\omega$ SST model to be used as a low-Re turbulence model without extra damping functions. The model also switches to a $k-\epsilon$ behaviour in the free-stream and thus avoids the problem with being too sensitive to inlet free stream turbulence properties. The model can produce a bit too large turbulence levels in regions with large normal strain, like stagnation regions and regions with strong acceleration.

3.3 Dimensionless Wall Distance

A dimensionless wall distance, y^+, is commonly used in boundary layer theory and can be defined as:

$$y^+ = \frac{u_* y}{\nu} \tag{45}$$

where u_* is the friction velocity at the nearest wall, y is the distance to the nearest wall and ν is the local kinematic viscosity. In CFD calculations, y^+ is often used to describe how coarse or fine a mesh

is close to a body and for turbulent modelling the parameter is important to determine the proper cell size near a wall. Different turbulence models can have different requirements for y^+.

Near wall treatment or wall functions are two different methods that can be used when treating the mesh closest to the body. In near wall treatment a high mesh resolution is used in the near-wall area and the eddies are resolved in all scales by integration. The boundary layer is completely resolved and this method is generally used for laminar flows and direct numerical simulation (DNS). Near wall treatment requires a $y^+ < 1$.

Wall functions allows for a coarser mesh near the wall and a higher y^+ value. ANSYS FLUENT suggests y^+ in the range $30 \leq y^+ \leq 300$ when wall functions are used, but other suggests a $y+$ in the range $50 \leq y^+ \leq 500$. Various wall functions are available for the different initial values in OpenFOAM and the choice of wall function depends on the case.

3.4 CFL Condition

Courant-Friedrich-Lewy (CFL) condition is a condition for stability of unstable numerical methods. The CFL condition expresses that the distance information travels in a mesh during a timestep must be lower than the distance between mesh elements. In other words, if the timestep is too large or the information travels too fast compared to the cell size the solver will "jump over" these cells and information will be lost. This will affect the next calculation and can result in instability and provoke a solution blow up. The CFL condition is therefore nessesary to ensure that information from one cell only propagates to its immediate neighbours. Equation 46 shows mathematically the CFL condition for a 2D case.

$$Co = \frac{u_x \Delta t}{\Delta x} + \frac{u_y \Delta t}{\Delta y} \leq Co_{max} \tag{46}$$

Co is called the Courant number, u_x and u_y are the velocities in x- and y-direction and Δx and Δy are the distance in x- and y-direction.

The CFL condition applies differently to explicit and implicit schemes. For explicit solvers $Co_{max} = 1$ is a requirement to avoid instability. Implicit schemes uses the entire domain to calculate each timestep and are more robust and may tolerate $Co_{max} > 1$. Although the implicit schemes can be more stable, this does not imply accuracy. Larger Co_{max} means larger timestep and this can lead to loss of e.g. fluctuation or transient features. Consequently, calculating local Courant number can be useful in critical areas to ensure the solution accuracy. Large variation in the Courant number are possible in a domain due to changes in cell size and local velocities. When calculating local Courant numbers the smallest cell size and the largest velocities in this area should be used. Although OpenFOAM uses implicit schemes, the maximal Courant number in the domain is kept below 1 to ensure accuracy.

3.5 Boundary Conditions

Boundary conditions are defined for cells facing a body surface or domain edge to solve the governing equations at these locations. Boundary conditions are often divided into Dirichlet and Newmann conditions. Dirichlet conditions specifies the solution value, while Newmann conditions imposes values of the derivative. The term *faces* is important when considering boundaries. *Faces* are defined as cell sides that creates a border to the domain or geometry. Figure 14 shows a picture of a general computational domain and the names used on the boundary surfaces.

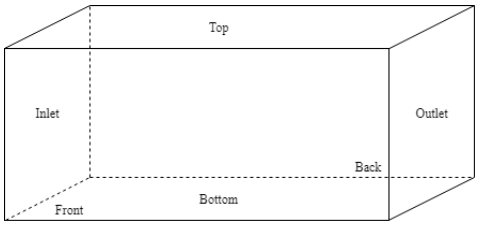

Figure 14: Computational domain and boundary surface.

A large number of boundary conditions are available in OpenFOAM, but only the ones used in this thesis will be described here.

3.5.1 Pressure and Velocity Boundary Conditions

Empty is a boundary condition used on a face for simulations in 1D and 2D, since OpenFOAM generates geometries in 3D as default. This is a method to force OpenFOAM into 1D or 2D simulation. *Symmetry* is a boundary condition that enforce a symmetry constrain. *FixedValue* is a boundary condition that supplies a fixed value constrain and is a boundary condition used at the inlet to simulate an uniform incoming flow. *ZeroGradient* is a boundary condition that prescribes the field gradient on a boundary to zero by applying a zero-gradient condition from a patch internal field onto the patch face. This boundary condition is often used on walls where the pressure gradient is set to zero and at outlets where the gradient for the velocity field and transported quantities like turbulent kinetic energy or dissipation rate is set to zero. The boundary condition *noSlip* fixes the velocity to zero and is often used at faces that border to non-moving walls or fixed geometries. Figure 15 shows a computational domain and boundary conditions for a fixed cylinder.

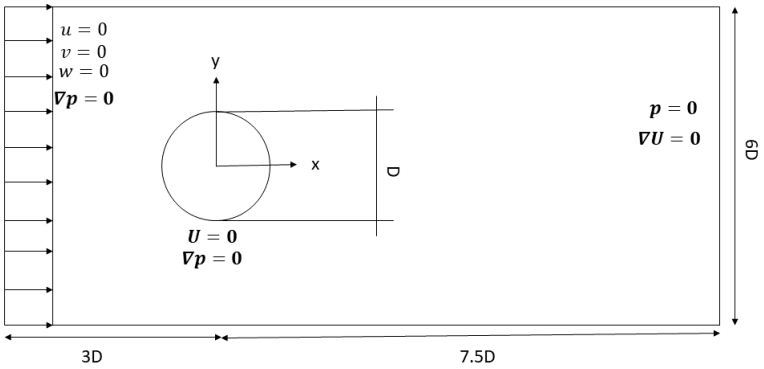

Figure 15: Computational domain and boundary conditions.

For moving meshes a *movingWallVelocity* is used at the cylinder surface. This boundary condition corrects the flux due to the mesh motion so that the total flux though the moving wall is zero. For overset grids the overset patch needs the boundary condition *overset*.

3.5.2 Turbulent Inlet Conditions

Turbulent inlet condition has to be specified when simulating free stream turbulence. In the $k-\omega$ SST turbulent model, k and ω has to be specified. This can be a challenge and a source to uncertainty since the incoming turbulence rarely is known. The incoming turbulence is often decided by qualitative estimations. Turbulent model variables, like turbulent energy, dissipation or Reynolds stresses are often

difficult to estimate directly. Common practise is to use variables like incoming turbulence intensity and turbulent length scale or eddy viscosity ratio. These properties can more easily be related to physical characteristics of the problem.

For isotropic turbulence, turbulent kinetic energy, k, can be computed as:

$$k = \frac{3}{2}(UI)^2 \tag{47}$$

where U is the mean flow velocity and I is the turbulence intensity.

Turbulent kinetic energy is the energy content in the eddies that are formed when instability emerges by extraction of energy associated with the mean flow. These eddies remains in the system until they break up into smaller eddies. The original energy content is divided and transferred into the smaller eddies. This is called energy cascade or forward cascade. The kinetic energy is transferred to smaller and smaller scales until the smallest scale (Kolmogorov scale) is reached and the energy is dissipated by friction.

U and I in Eq. 47 is defined as:

$$I = \frac{u'}{U} \qquad U = \sqrt{U_x^2 + U_y^2 + U_z^2} \tag{48}$$

where u' is root-mean-square of the turbulent velocity fluctuations.

The turbulent intensity level varies between low-, medium- and high turbulence. In low turbulence cases e.g. external flow around cars, submarines and air crafts have typically $I < 1\%$. Medium turbulence cases, e.g. flow in pipes and ventilation flows, can typically have $1\% < I < 5\%$. High turbulence cases, e.g. high-speed flow in complex geometries can have $5\% < I < 20\%$. A low turbulence intensity, 1%, is chosen for this study.

Turbulent specific dissipation rate, ω, is the rate at which the turbulence kinetic energy is converted into thermal internal energy per unit volume and time. ω is defined as:

$$\omega = \frac{k^{0.5}}{C_\mu T_{u_L}} \tag{49}$$

where C_μ is 0.09 and T_{u_L} is turbulence length scale.

Turbulent length scale, T_{u_L}, is a physical quantity that describes the size of the energy containing eddies in a turbulent flow. T_{u_L} is often used in CFD simulation to estimate the turbulent properties at the inlets and is commonly estimated as a certain percentage of a characteristic dimension of the problem. In project a turbulence length scale of 3% of the diameter is used and is based on the study of the effect of different T_{u_L} that was conduced during the previous work.

Chapter 4

4 Grid Generation Methods

Mesh quality is essential for accuracy and convergence of the results. Mesh generation are constantly evolving and, a large number of different methods are applicable. A mesh can usually be categorized as structured, unstructured or hybrid. Table 2 gives a quick overview of the three meshing methods that is used in this study. The next sections will give a more in depth explanation of the structured and unstructured grid.

Table 2: Grid generation methods.

blockMesh	snappyHexMesh	overset mesh
Time consuming when meshing complex geometries with many blocks	Unstructured mesh, less time consuming when meshing complex geometries	Overset mesh interpolation can be time consuming
Difficult to manage the cell transition between blocks	Many parameters in the snappyHexMeshDict that needs to be tuned	No distorted cells when considering moving meshes
No distorted cells, but cell aspect ration needs to be considered manually	Distorted cells close to a curved body	May suffer from interpolation errors
Distorted cells when considering body motion and mesh morphing	Distorted cells when considering body motion and mesh morphing	No use of mesh morphing and no reduction in grid quality

4.1 Structured Grid - blockMesh

The main difference between a structured and an unstructured mesh is how data is stored. In a 2D structure, every node has a corresponding integer, i and j index value, which is unique. The nodes physical locations are stored in a table or are functionally related to the mesh space i.e. (x,y) = f(i,j). The mesh generation utility, blockMesh, generates high quality meshes and is based on the principle to decompose the domain with the geometry into a set of one or more three dimensional hexahedral blocks. blockMesh is a useful tool for simple geometries, but the effort and time required to setup the dictionary increases with the complexity of the geometry.

A structured grid, generated with blockMesh, was used in the project thesis. For simplicity, only half of the mesh is generated before the mesh is mirrored to obtain the whole domain. Figure 16 shows the numbering of the vertices in one plane (in red) and the block numbers (in black). All geometries in OpenFOAM are generated in 3D and two plane are defined at z = 0.5 and at z = -0.5. The vertices in Fig. 16 are located at z = -0.5 while another set of 19 vertices are located at z = 0.5 and a total of 38 vertices are defining the 10 blocks. The numbering order are the same for the two plane e.g. vertex number 19 and 20 are located at the same x- and y-coordinates as vertex number 0 and 1, but at z = 0.5.

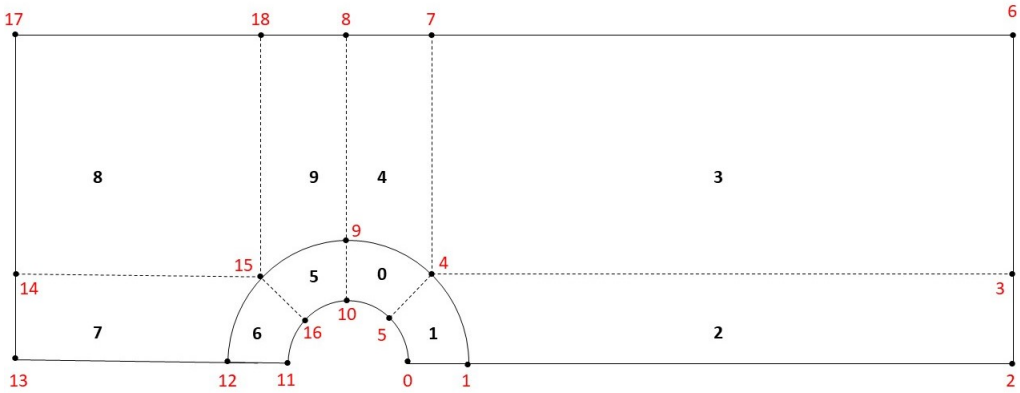

Figure 16: Mesh with blocks and vertices.

A global coordinate system is defined at the cylinder center and local coordinate systems are defined for each block.

blockMesh allows the user to define the number of cells in x- and y-direction individually for each block. The only constrain is that the number of cells at the border between blocks has to be equal. The user is also allowed to apply grading in x- and y-direction to vary the cell size within a block. The local coordinate systems has to be considered when choosing the number of cell and grading in the different directions. An overview of the local coordinate systems are given in Fig. 24.

The challenge with this mesh is that many of the parameters must be changed manually, and the number of parameters increases with the number of blocks. When writing the blockMesh as an .m4 file the number of parameters that needs to be changed are reduced, since .m4 allows the user to write parameters as functions of each other and many parameters of the parameters i blockMesh depends on each other.
The initial mesh for one cylinder was generated with blockMesh as shown in Fig. 17.

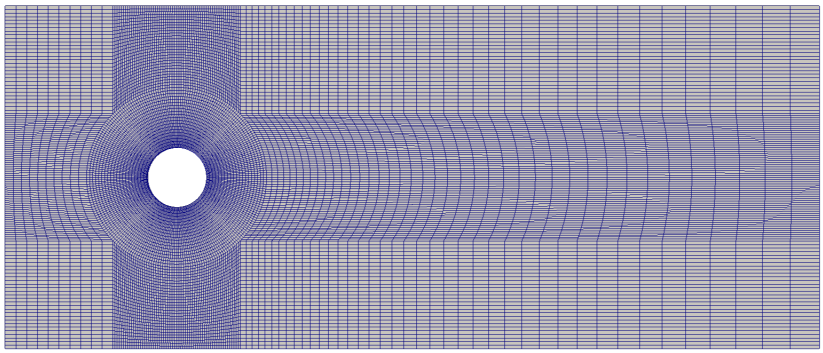

Figure 17: Mesh for one cylinder generated by blockMesh.

This mesh provided satisfying results in a convergence study for $Re = 100$, but has a critical area shown in Fig. 18.

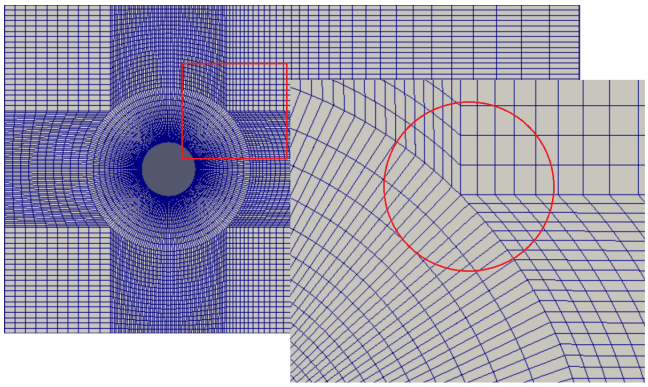

Figure 18: Critical area for blockMesh.

An other issue is the transition between the cells in the inner curved blocks and the outer blocks. Since the mesh is hardcoded and the number of cells in each block are defined by the user adjustments in the mesh has to be conducted manually. This can be troublesome for inexperience users and for complex meshes with many blocks. To save time and trouble when creating and refining a mesh for three cylinders an unstructured mesh is an attractive alternative.

4.2 Unstructured Grid - snappyHexMesh

An unstructured mesh can be generated with snappyHexMesh and is a good alternative to blockMesh for complex geometries. The snappyHexMesh utility generates a 3D mesh containing hexahedra and split-hexahedra from a triangulated surface geometry in STL format.

The mesh generation with snappy can be divided into six steps:

1. Generation of a background/base mesh
2. Geometry definition
3. Generation of a castellated mesh/cartesian mesh
4. Generation of a snapped mesh of body fitted mesh
5. Addition of layers close to the surfaces/boundary layer meshing
6. Check/enforce mesh quality

In this work, the background mesh consist of a singe block of pure hexes and is generated in blockMesh. The cell aspect ratio should be approximately 1, at least close to the body surface. The STL geometry can be obtained from any Computer-aided design (CAD) program and in this work a CAD model of the cylinder with 500 vertices was modelled in Blender. Step 3, 4 and 5 are controlled by the dictionary snappyHexMeshDict. In the settings for the castellatedMesh generation the level of refinement at the surface and in the refinement regions are defined. Most of the default options in snapControls were kept, but for more complex geometries these might need adjustments. Seven surface layers were added to capture the boundary layer. In addLayersControls, the first layer thickness and the expansion ratio is chosen. The default settings for the meshQualityContols were also kept. Figure 19 shows an example of a mesh for a cylinder with snappyHexMesh. Two refinement regions are chosen for this mesh and no layers are added.

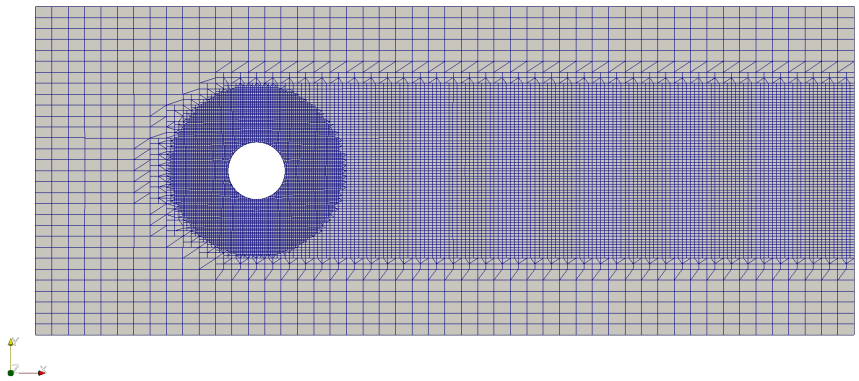

Figure 19: Unstructured mesh - snappy.

4.3 Overset Grid Method

The overset grids is a rather new function that came with OpenFOAM v1706 in 2017. Overset, also known as Chimera approach or overlapping grids, allows the user to create multiple mesh regions separately and merge them together into one mesh. The benefits with this type of grid is the superior performance as a dynamic mesh when large motions are considered.

When creating a moving mesh with overset the user first creates a background mesh that is suppose to be fixed. Then the moving part of the mesh is created and the two meshes are merged together. The benefits with overset is that the moving mesh will move on top of the background mesh, due to cell-to-cell mapping between the two layers and this will not result in any disordered cells. For cases with large motion this method is recommended.

The overset grid method can be divided into four execution steps:

1. Identify hole cells
2. Identify fringe cells
3. Identify donor cells
4. Interpolation between fringe and donor cells

Hole cells are defined as cells in the background that lies inside the moving body. These cells are marked and blanked out during the solution process and is the main cause for the extensive computational cost [21]. Fringe cells are defined as the cells adjacent to the hole cells and as the cells at the outer boundary of the body-fitted grid. The fringe cells are used a boundary cells and the boundary values are determined through solution interpolation. Donor cells are cells on both grids that acts as interpolation partners.

The four steps explained above affects the quality of the numerical results directly and relates the solution quality to the employed interpolation scheme and problem discretisation.

4.4 Dynamic Mesh Motion Methods

A dynamic mesh provides a challenge regarding increase in computational cost, numerical stability issues and modelling limitations when large structural displacement are considered. Large structural displacement is especially an issue when considering a resonant phenomena like VIM.

One approach to incorporate structural motion in CFD simulations are body fitted approaches. For a fixed grid connectivity, body motion can only be accounted for by mesh morphing. Mesh morphing is a method where the displacement is diffused within the domain. This method is well established and is stated as computationally efficient. The drawback with the method is the potentially occurrence of numerical errors due to low grid quality. Mesh morphing can result in high aspect ratio and highly skewed cells when the motions are large. Hence, this method is best suited for small, single degree of freedom motions.

An alternative to the body-fitted approaches is the overset grid method. With this method two grids are internally static with fixed grid connectivity, but are able to move relative to each other. Interpolation between the grids is used to transfer solutions across grid interfaces. Compared to body fitted approaches, this method increases the numerical stability when considering large motions. The drawbacks with the overset grid method is the potentially increase in computational time and that the results can suffer from numerical interpolation errors which consists of conservation and convergence issues. This method has better stability as the mesh quality is constant.

Chapter 5

5 Concept

In this section the physical structures and concepts are described. The two platforms are designed to operate at the same site, West of Barra. Only the current will be considered in this chapter. For further environmental data the reader is advised to read the LIFE50+ report [15]. This report gives a detailed description of the environmental conditions on the site. The semi-submersible concept was suggested by Wood and is a part of a master thesis by Markus Johannessen [18]. A spar platform was designed with the same main diameter as the columns on the semi-submersible to make them comparable. The design of the spar platform was conducted by John Marius. An estimation of the VIM occurrence at the site is also presented in this chapter.

5.1 Environment Condition - Current

No site-specific current data is available at West of Barra and the current characteristics given in the LIFE50+ report have been based on available met-ocean numerical model data provided in [31] and in [17]. The assumptions have been taken as recommended by DNV GL [13]. The average water depth at this site is 95 m, which is too shallow for a spar. The water depth is therefore assumed to be 320 m as this the water depth the mooring lines for the spar platform are designed for.

The current is divided into a wind component and a tidal and surge component. The wind induced current have maximum velocity at the sea surface and can be assumed to have no effect at 50 m water depth. The variation of wind generated current can be modelled as:

$$v_{c,wind}(z) = v_{c,wind}(0)\left(\frac{d_0 + z}{d_0}\right) \quad \text{for} \quad -d_0 < z < 0 \tag{50}$$

The tidal and surge induced current profiles are modelled according to:

$$v_{c,tide}(z) = v_{c,tide}(0)\left(\frac{d + z}{d}\right)^{\alpha} \quad \text{for} \quad z < 0 \tag{51}$$

where:

z is distance from still water level, positive upwards
$v_{c,tide}(0)$ is tidal current velocity at still water level
$v_{c,wind}(0)$ is wind-generated current velocity at still water level
d is water depth to still water level (taken positive)
d_0 is reference depth for wind generated current, $d_0 = 50$ m
α is an exponent - typically 1/7

Table 3: Current speeds for 1 and 50 years return period [17].

Return period [year]	Wind induced current speed [m/s]	Tidal current [m/s]	Storm surge current [m/s]	Combined current [m/s]
1	0.88	0.39	0.53	0.84
50	1.15	0.44	0.6	0.94

A wind farm is typically planned for a 20-year design life and a 50 year return period of the characteristic loads is recommended in DNV offshore standard [12]. By using the values in Table 3 for a 50 years return period, current speed profiles are plotted according to Eq. 50 and 51 as shown in Fig. 20. The graphs shows that the current speeds have a shear profile and there are various methods for deciding

what current speed to use when calculating the vortex induced loads. One method is to discretise the current profile as done by Tang et al. [40]. In this project, the mean current velocity of the combined wind, tidal and surge profile will be used as an upper limit as these calculations are done for a 50 year return period and indicate extreme condition. The spar and semi-submersible will have different mean extreme current speed due to different draught. The spar has a mean combined current speed on 1.40 m/s and the semi-submersible will have a mean combined current speed on 2.07 m/s.

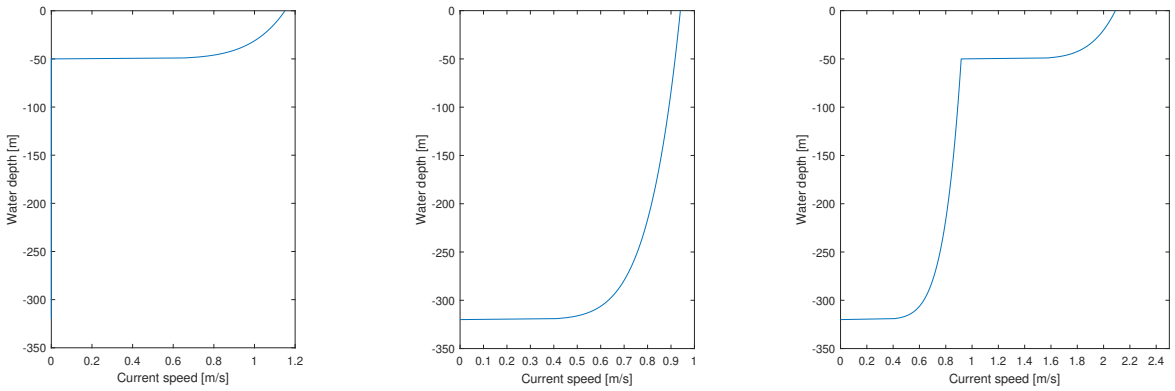

Figure 20: Current speed profile. The left graph shows the wind induced current speed profile, the middle graph shows the combined tidal and surge induced current speed profile and the right graph shows the total current speed profile.

5.2 Reference Turbine

The DTU 10 MW Reference wind turbine (DTU 10-MW RWT) is used as a reference turbine [5]. This is a large turbine compared to existing turbines and shows the next step of wind turbine size. The DTU 10-MW RWT is a three-bladed upwind turbine, with 10 MW rated power and a 178.3 m rotor diameter. The total mass of the nacelle, blades, hub and tower is 1 305 146 kg. The semi-submersible where conservatively dimensionalised to support the original DTU 10-MW RWT. This might not be optimal since the DTU 10-MW RWT is design to operate at a bottom fixed structure and not on a floater. This was taken into consideration when setting up the spar model. The total turbine mass is 1.25×10^6 kg for the spar structure. The mass is the most interesting parameter for this study and further turbine characteristics are described by Bak et al. [5].

5.3 System Characteristics - Spar

The spar model was made by John Marius. The main dimensions are given in Fig. 21 and the platform properties are given in Table 4.

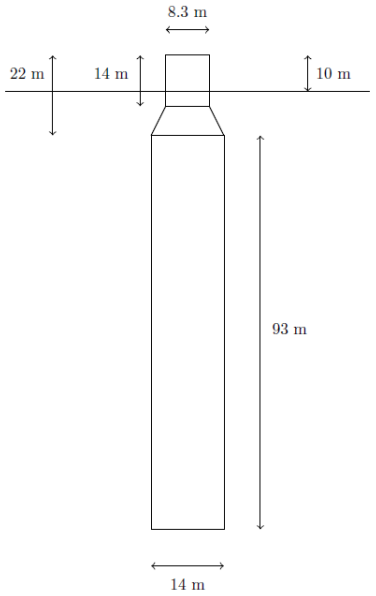

Figure 21: Main dimensions-Spar foundation.

Table 4: Platform Properties - Spar foundation.

Parameter	Value	Unit
Draft	105.00	[m]
Elevation to tower base above SWL	10.00	[m]
Depth to top of taper below SWL	4.00	[m]
Depth to bottom of taper below SWL	12.00	[m]
Diameter above taper	8.30	[m]
Diameter below taper	14.00	[m]
Mass including ballast	1.41E7	[kg]
Displacement	1.53E4	[m^3]
Moment of inertia about CoG	6.14E9	[kgm^2]
Vertical CoG below SWL	83.7	[m]
Vertical CoB below SWL	55.1	[m]

The mass given in Table 4 does not include the turbine, only the spar platform and the ballast. The displacement is given for the platform with operational draft. The moment of inertia is given for the support structure about local CoG. The moments of inertia for the turbine was calculated about still water level. The moments of inertia for the total system and the global CoG were calculated.

The center of gravity for a complex system can be found by breaking the system into simple parts and calculate the center of gravity for each part. The center of gravity for the total turbine-spar system is found by using Eq. 52.

$$z = \frac{m_T \cdot z_T + m_S \cdot z_S}{m_T + m_S} \tag{52}$$

m_T and m_S are turbine mass and mass of the spar. z_T is distance from SWL to CoG_T and z_S is distance from SWL to CoG_S. To find the moment of inertia for the total system about SWL the parallel axis theorem is used to find the moment of inertia for the spar about SWL. The results are given in Table 5

Table 5: Turbine, Spar foundation and total system properties.

Turbine			
m_T	1.25e6	[kg]	
CoG_T	88.6	$[m]$	Over SWL
I_{xx}, I_{yy}	1.17e10	$[kgm^2]$	About SWL
Spar			
m_S	1.41e7	[kg]	
CoG_S	83.7	$[m]$	Below SWL
I_{xx}, I_{yy}	5.14e9	$[kgm^2]$	About CoG_S
I_{xx}, I_{yy}	1.04e11	$[kgm^2]$	About SWL
System			
m	1.535e7	[kg]	
CoG	69.67	$[m]$	Below SWL
CoB	55.1	$[m]$	Below SWL
I_{xx}, I_{yy}	1.156e11	$[kgm^2]$	About SWL
I_{zz}	4e8	$[kgm^2]$	About SWL

5.3.1 Natural Periods

The natural periods were calculated for the spar. The natural period is calculated for $\omega \to 0$ or $\omega \to \infty$ and there will be no damping. The mass, added mass and stiffness matrices are given in Appendix I.

The mass matrix is found by using the system properties given in Table 5. The natural period in heave and yaw are not of interest and I_{46} is set to 0. I_{66} is needed for the mass matrix to be invertible, but this value is equal I_{zz}.

A stiffness matrix due to the mooring lines was given. The mooring line stiffness was given by John Marius. In addition to the mooring line stiffness the system will experience hydrodynamic restoring moments in roll and pitch. These restoring moments are calculated according to equation 19 and 20. The additional stiffness in heave direction was not considered as the natural period in heave is not of interest.

Strip theory is used to calculate the added mass for a coupled system in sway and roll. The submerged part of the system, which is shown in Fig. 21, where divided into three parts and the added mass was calculated separately before added together. The second part with varying diameter was divided into eight parts were the average diameter where calculated for each part. The average diameter was found by first finding the linear equation for the increase in diameter. The average 2D added mass was then found for each slice and this is integrated over the part. The total added mass is found by summing up the the added mass for the three parts.

Due to the symmetry of the problem only added mass in sway (A_{22}), roll (A_{44}) and coupled added mass in sway due to roll motion (A_{24}) are calculated. The other added mass coefficients are found through the relations: A_{11}=A_{22}, A_{42}=A_{24}, A_{15}=-A_{24}, A_{51}=A_{51} and A_{55}=A_{44}.

The eigenvalues are found by solving the eigenvalue problem, as described in section 2.8, in MATLAB and the natural frequencies are found as $\omega = \sqrt{\lambda}$ where ω is given in $[rad/s]$.

The coupled natural frequencies and periods in surge, sway, roll and pitch are given in Table 6.

Table 6: Coupled Natural frequency and period for spar.

	Natural fequency	Natural Period
Surge	0.0488 [rad/s]	128.87 [s]
Sway	0.0488 [rad/s]	128.87 [s]
Roll	0.1998 [rad/s]	31.45 [s]
Pitch	0.1998 [rad/s]	31.45 [s]

To evaluate the effect of coupling the uncoupled frequencies and periods where found by setting the coupled coefficients in the mass, stiffness and added mass matrix to zero. The uncoupled natural frequencies and periods are given in Table 7.

Table 7: Uncoupled Natural frequency and period for spar.

	Natural fequency	Natural Period
Surge	0.0488 [rad/s]	128.74 [s]
Sway	0.0488 [rad/s]	128.74 [s]
Roll	0.1212 [rad/s]	51.82 [s]
Pitch	0.1212 [rad/s]	51.82 [s]

Table 6 and 7 shows that the coupled and uncoupled natural periods in surge and sway are almost the same. A large difference is observed between the coupled and uncoupled natural periods in roll and pitch.

To verify that the natural periods are calculated correctly, simple calculations were done considering a one DoF system in surge, sway, roll and pitch. By using Eq. 30 the natural periods were calculated and compare to the results found by solving the eigenvalue problem without coupled coefficients. These results where equal and implies that the method for solving the eigenvalue problem was correctly implemented in MATLAB. Another checks that was done to verify the system was to compare the mass and added mass matrix. The coefficients in the mass and added mass matrix should have the same sign and the matrices should be symmetrical.

When comparing the coupled and uncoupled natural periods given by MATLAB the eigenvalues should be evaluated against the eigenvectors. For an uncoupled system the eigenvector will be one in the considered direction. For a coupled system this can be more than one eigenvector associated with one eigenvalue depending on the coupling. In surge and sway the value of the eigenvector in surge and sway were much larger than the eigenvector in pitch and roll. This shows that for these DoF the coupling has little effect. The eigenvalue in roll has an coupled eigenvector, with significant size, in addition to the eigenvector in roll. This implies that the eigenvalue in roll is quite affected by motion in sway. The same goes for the eigenvalue in pitch.

When looking at the eigenvalues in terms of the eigenvector it makes sense that the natural periods in surge and sway are more equal for the coupled and uncoupled system than the natural periods in roll and pitch. When looking at this system in a physical way the results are also consistent. The global coordinate system was chosen with origin at SWL. This was done because the mooring line stiffness was calculated about SWL and it makes the calculations for added mass easier especially in roll. An local coordinate system is not needed if the moment of inertia in y-direction is taken about SWL and you do not need to convert between a local and global coordinate system. In addition, this is common practice for floating structures, but it introduces coupling for a spar because in reality the spar moves in roll and pitch about CoG. When a spar rotates in pitch about CoG the platform will

have a transition in surge at SWL. This is shown to the right in Fig. 22. In this figure, it is clear that a rotation about CoG for a spar will cause a transition in x-direction at SWL. This will not be captured if the system is treated as uncoupled. In an uncoupled system, where the motions are defined about SWL, the system will behave as shown to the left in the figure. This gives an physical explanation for the observed difference between coupled and uncoupled roll and pitch.

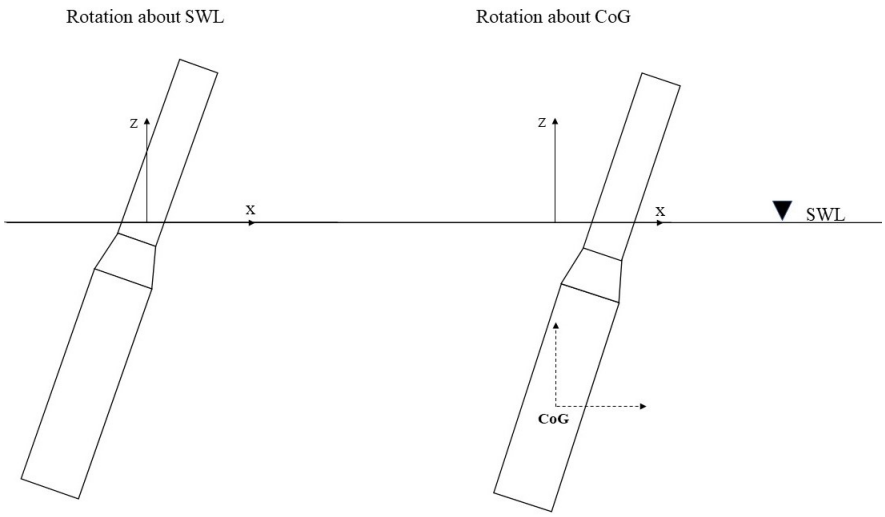

Figure 22: The effect of coordinate system definition on the rotational coupling.

5.4 System Characteristics - Semi-submersible

The system characteristics for the semi-submersible where given by Wood together with the natural period at zero frequency.

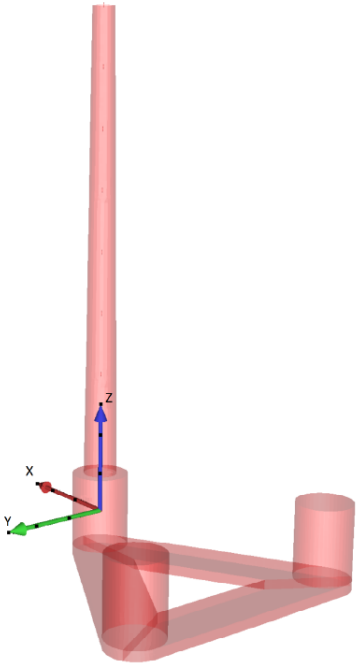

Figure 23: Main dimensions Semi-submersible-foundation.

Table 8: Platform Properties - Semi-submersible foundation.

Parameter	Value	Unit
Distance between columns	59.50	[m]
Height of column	18.78	[m]
Diameter of column	14.00	[m]
Height of pontoon	2.50	[m]
Width of pontoon	14.00	[m]
Draft	11.28	[m]
Displacement	10 080.05E3	[kg]
COG	(-34.31 0.00 6.93)	[m]
COB	(-34.31 0.00 -8.54)	[m]
GM_{0L}	12.81	[m]
GM_{0T}	12.81	[m]
$\eta_{5,\text{static}}$	9.71	[deg]

Table 9 shows the parameters used in the calculation. m is the mass of the support structure including the ballast, m_T is the turbine mass, m_a is added mass and c is the mooring line stiffness. The mooring line configuration is similar to the NREL Semi-submersible OC4 platform and the stiffness is then the same [30].

Table 9: System characteristics and Natural period - Semi-submersible.

m [kg]	m_T [kg]	m_a [kg]	c [N/m]	f_0 [1/s]	T_0 [s]
1.82E7	1.31E6	4.58E3	7.08E4	0.0096	104.17

5.5 VIM Occurrence

VIM can occur when the natural period of the structure is equal to the vortex shedding period. The vortex shedding period can be found from the Strouhal number as:

$$T_v = \frac{D}{StU_c} \tag{53}$$

The Reynolds number for current speed between 1.4 m/s - 2.07 m/s, D = 14 and $\nu = 1.83 \times 10^{-6}$ are of order 10^6-10^7. This corresponds to a $St \approx 0.25$ according to Fig. 2 and Faltinsen [14].

By assuming that the vortex shedding period is equal to the natural period of the cylinder, the current velocity for when this happens can be found.

For the spar, this gives a current velocity $U_{c,1\_s} = 0.47$ m/s and $U_{c,1\_s}$ gives a reduced velocity, $U_{R,1\_s} = 4.045$. The extreme condition $U_{c,2\_s} = 1.38$ m/s gives a vortex shedding period on 40.58 s for St = 0.25 and a reduced velocity, $U_{R,2\_s} = 1.88$.

The same approach is used for the semi-submersible and gives a current velocity $U_{c_1\_ss} = 0.54$ m/s and $U_{c_1\_ss}$ gives a reduced velocity, $U_{R_1\_ss} = 4.02$ which is similar to the reduced velocity $U_{R_1\_s}$ for the spar. The extreme condition $U_{c,2\_ss} = 2.07$ m/s gives a vortex shedding period on 27.05 s for St = 0.25 and a reduced velocity, $U_{R,2\_ss} = 15.40$.

Cross-flow vortex shedding excitation can occur for $3 \leq U_R \leq 16$ for all Reynolds numbers and maximum response is often found in the range $5 \leq U_R \leq 9$ [13].

None of the calculated reduced velocities are in the range of maximum response, but since current velocity is not a fixed value at a site the platforms can still experience large response for current velocities between $U_{c,1}$ - $U_{c,2}$ that results in more critical U_R.

Chapter 6

6 Analysis of Two Grid Approaches for a Fixed Cylinder

6.1 blockMesh

A mesh refinement study for a turbulent case was a natural way to continue the work conducted in the project thesis. Two methods of refinement were tested. First the number of cells in all the block were multiplied with a factor of 1.5 in the same way as Squries et al. [37] did in their simulation of the flow around a circular cylinder in using detached-eddy simulation. This resulted in an unstable solution. Another approach was then tested where the inner blocks were refined while the number of cells in the outer block was kept constant before the number of cells in the inner blocks was kept constant and the number of cells in the out block was varied. Some of the combinations with inner cells and outer cells resulted in stable vortex shedding, but many did not.

The simulation parameters used in the turbulent simulations are given in Table 10. In this mesh refinement study an adjustable timestep is used to have the same CFL number for all simulations. The maximum CFL number is kept constant at 0.6.

Table 10: Turbulent simulation parameters.

U [m/S]	ν $[m^2/s]$	Re [-]	ρ $[kg/m^3]$	Co_{max} [-]	I [%]	T_{u_L} [m]	k $[m^2/s^2]$	ω [1/s]
1	1.83E-6	$7.65 \cdot 10^6$	1000	0.6	1	0.42(3%)	1.5E-4	0.02916

Figure 24 shows the mesh refinement parameters that are varied in Table 11. nx0 is the number of cells from the cylinder surface and out into the flow for the inner block. nx0 is also the number of cells in x-direction for block 4 and 9 since the blocks are connected and the number of cells has to be equal at the borders between the blocks. ny0 is the number of cells along the body for the inner block and the number of cells in y-direction for block 2 and 7. nx2 are the number of cells in x-direction for block two and three, while ny3 is the number of cells in y-direction for block 3, 4, 9 and 8. nx7 is the number of cells in x-direction for cell 7 and 8. y6 is the distance from y=0 to the domain top, which is equal to half of the total domain width. x13 and x2 are the distances from origin to the inlet and outlet. These values are given as a function of the cylinder radius ($r = 7\ m$).

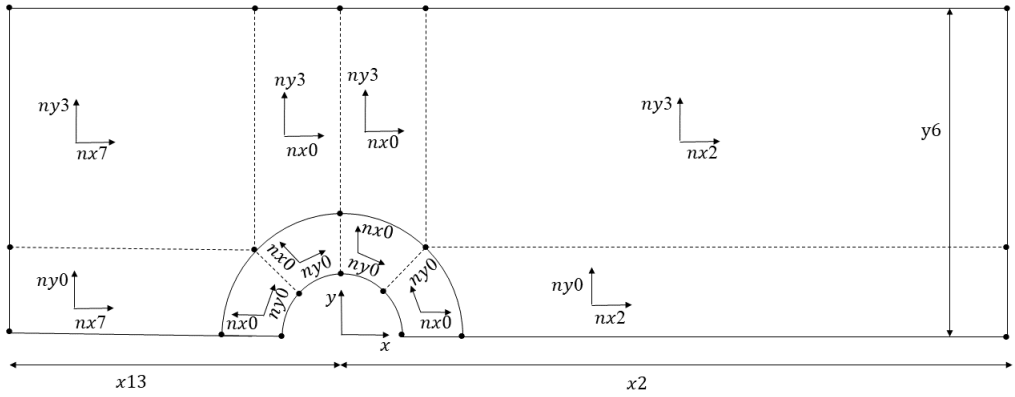

Figure 24: Local coordinate systems for individual blocks in structural mesh.

Table 11 shows the different cases and the cell numbers associated with the case. The domain size is constant for all cases.

Table 11: Mesh refinement study for structural grid.

No.	nx0	ny0	nx2	ny3	nx7	x2	y6	x13
Initial	50	70	50	40	10	15r	6r	-6r
1	$100 \cdot 1.5$	$70 \cdot 1.5$	$50 \cdot 1.5$	$40 \cdot 1.5$	$10 \cdot 1.5$	15r	6r	-6r
2	100	70	50	40	10	15r	6r	-6r
3	110	80	50	40	10	15r	6r	-6r
4	150	100	50	40	10	15r	6r	-6r
5	100	70	80	50	10	15r	6r	-6r
6	100	70	90	60	20	15r	6r	-6r

Figure 25 - 31 shows the drag coefficient for the different cases. The drag coefficient is an integrated quantity and can not be used directly to find an error in a simulation, but can be used to check if you should look for one. In this case the drag coefficient clearly shows that something is wrong and that the simulation has stability issues.

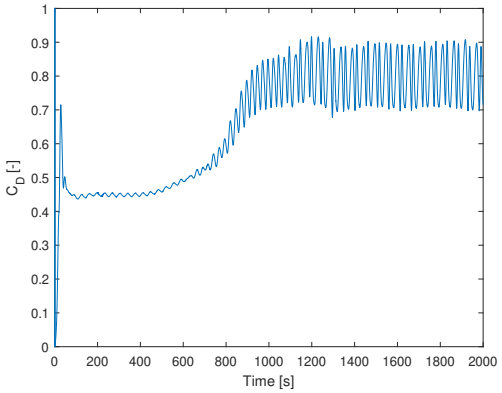

Figure 25: C_D for initial case with blockMesh.

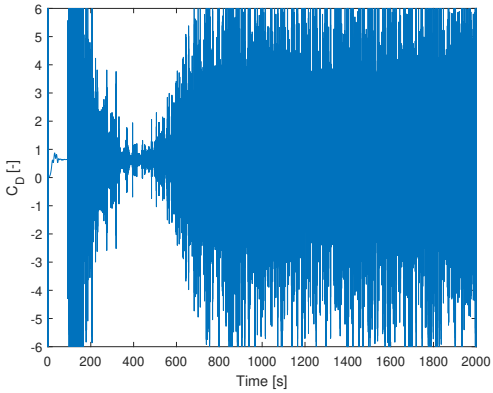

Figure 26: C_D for case No. 1 with blockMesh.

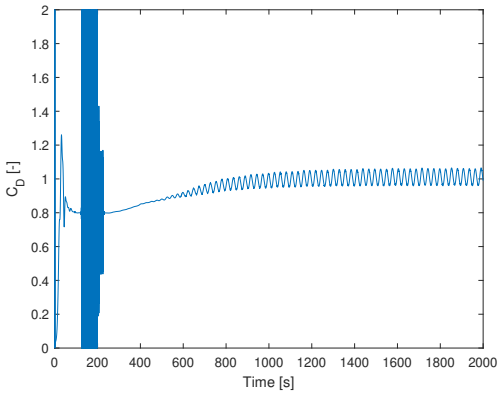

Figure 27: C_D for case No. 2 with blockMesh.

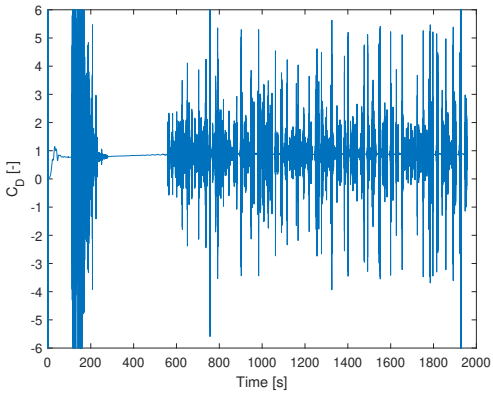

Figure 28: C_D for case No. 3 with blockMesh.

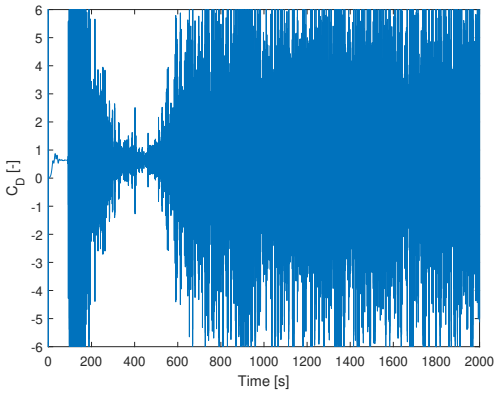

Figure 29: C_D for case No. 4 with blockMesh.

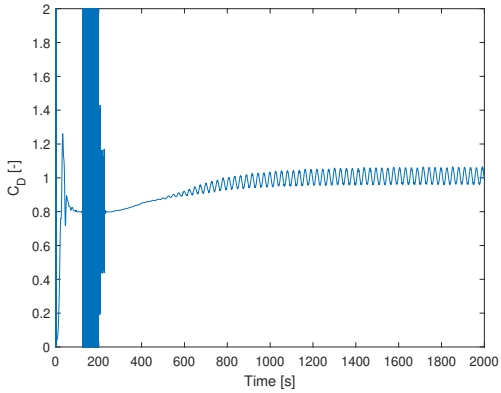

Figure 30: C_D for case No. 5 with blockMesh.

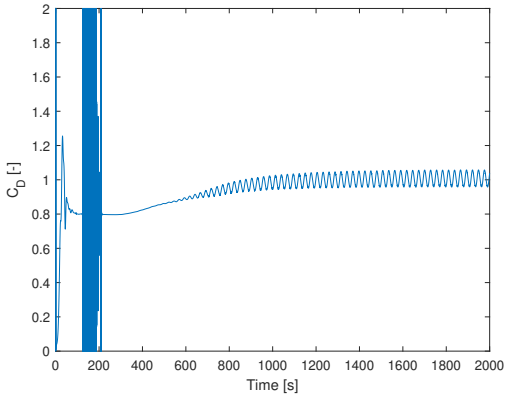

Figure 31: C_D for case No. 6 with blockMesh.

Case 2, 5 and 6 resulted in similar results shown in Fig. 31. An initial instability is observed in the time between 100-250 s before the solution becomes stable. Periodic vortex shedding occurs around 800 s. Case No. 4 gives same result as No. 1 and No. 3 gives an unstable solution , but not as unstable as No. 1.

6.1.1 Discussion

The flow features in the time period 100 s - 250 s for case No. 6 is studied to understand the highly unstable behaviour of the drag coefficient.

Figure 32 shows the pressure and velocity field at t=183 s which corresponds to a time instant in the time period where the strange behaviour of the drag coefficient was observed. At the right-hand side of the cylinder, which is the down stream side, both a high and a low pressure field are located close to the cylinder. This is not the expected pressure field when considering the corresponding velocity field. This pressure behaviour indicates that the numerical method experiences some instability in this time period.

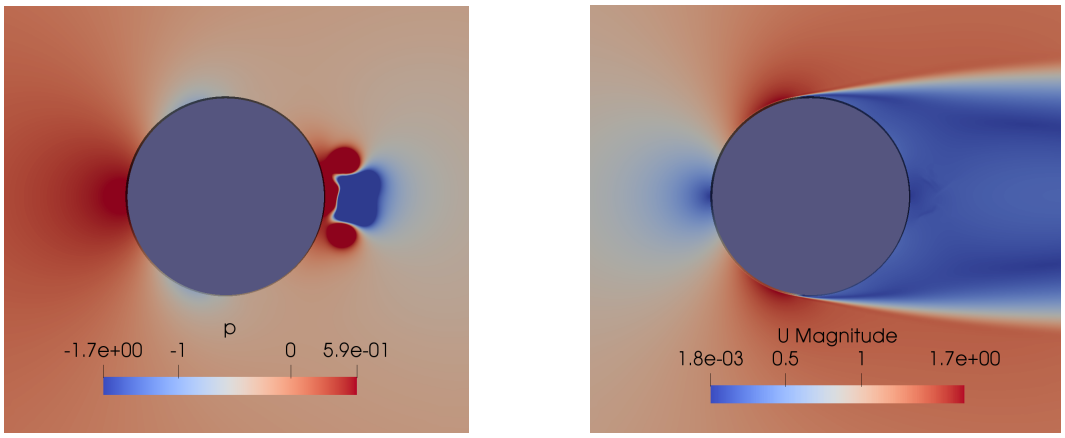

Figure 32: Pressure and velocity fields for at t=183 [s].

As show in Fig. 33, the pressure filed looks normal again at t = 229 s, which implies that at this time the solution has become stable again. This agrees with the behaviour of the drag coefficient.

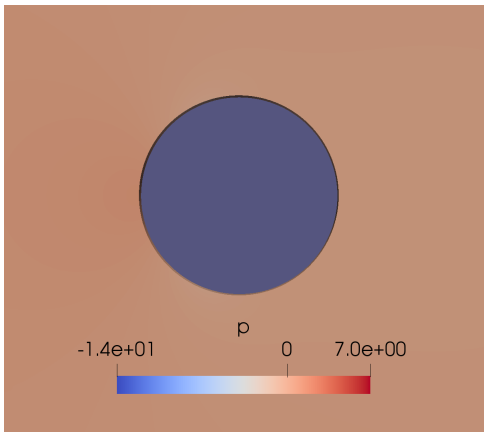

Figure 33: Pressure field for structured grid at t=229 [s].

The grid was first checked, but there are no skewered cells or bad aspect ratio in this region. The next to be considered was the CFL condition. If the CFL condition is not fulfilled the simulation can experience numerical instability. The output log for the simulation was first studied to check if this instability can be related to the CFL number. A timestep slightly over 0.02 was used throughout the simulation and the CFL number was kept at a maximum of 0.6. The small variation in the timestep is suspicious when the local velocities varies from 0 to 1.7 according to Fig. 32. By comparing the timestep with the evolution of the flow it was observed that the timestep even increased slightly even though high velocities were locally present in the flow. The same case was tested with a fixed timestep of 0.01, 0.02 and 0.03 to confirm that the problem lies with the CFL condition and the use of too large timestep. Figure 34 to 36 shows the pressure and velocity field for the new simulation at almost the same time instant. The results shows that a smaller fixed timestep does not experience unnatural behaviour of the pressure field close to the cylinder, but that a higher timestep experience the same unnatural behaviour and at an even larger scale.

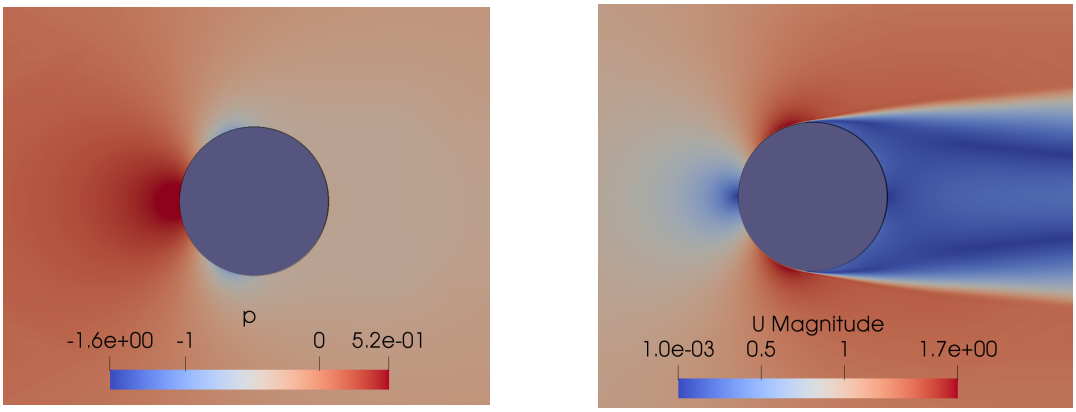

Figure 34: Pressure and velocity field at t=180 [s] and dt = 0.01 [s].

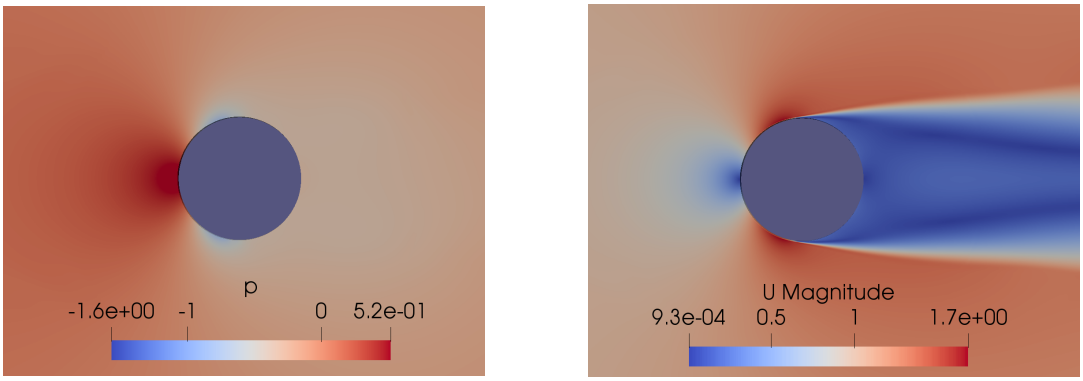

Figure 35: Pressure and velocity field at t=180 [s] and dt = 0.02 [s].

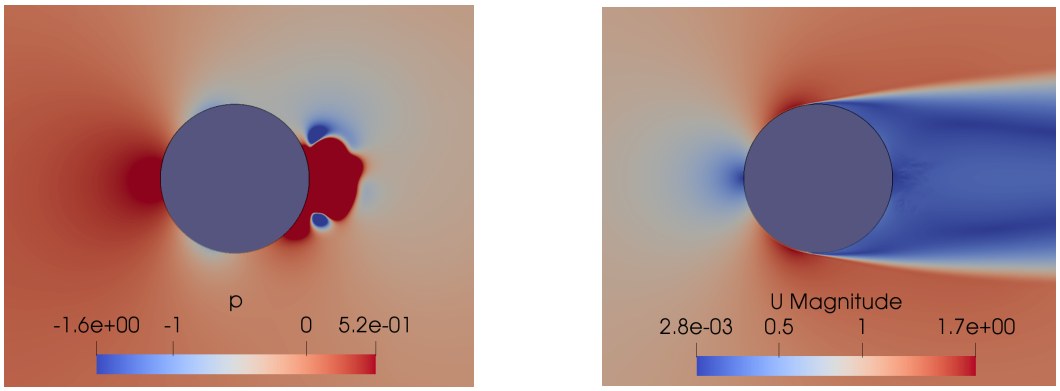

Figure 36: Pressure and velocity field at t=180 [s] and dt = 0.03 [s].

This indicates that the CFL condition is not fulfilled even though the simulation reports a maximum Courant number equal to 0.6 which is smaller than 1. The little variation in the timestep suggests that the local variation in the velocity is not considered when the solver calculates the CFL number. When calculating the CFL number the smallest cell size and the highest velocity in the domain should be used since these requires the smallest timestep. The smallest cell size in this grid is the first cells at the

cylinder surface with $\Delta x = 0.036$ and $\Delta y = 0.078$. By using $\Delta x = 0.036$, $u_x = 1.7$ and $Co_{max} = 0.6$ a dt equal 0.013 is calculated. This is smaller than 0.023 which was the dt used in the simulation at this time instant. $dt = 0.021$ if $u_x = 1$, which is the free stream velocity. These results confirms the suggestion that the local variation in the velocity is not considered when the solver calculates the CFL number. To avoid this issue the use of dynamic timestep should have been studied more carefully and a smaller maximal timestep should have been chosen. The challenge with this mesh refinement is that for every refinement in the inner blocks the smallest cell becomes smaller and this change the required dt. Then ideally the maximal required dt should have been calculated for every mesh and this dt should have been used either as the maximal timestep or as a fixed timestep. This mesh created with blockMesh proved to be too challenging due to the many parameters that has to be change manually and the structured mesh was decided to be unfit for future work where a mesh for three cylinders has to be created. An unstructured mesh is too time consuming due to the many manually changes in the mesh.

6.2 snappyHexMesh

6.2.1 Laminar

An unstructured mesh was tested due to the difficulties with achieving a stable solution with blockMesh for a turbulent case. An unstructured mesh is also more convenient for the study with three cylinders, which is presented in Section 7. The unstructured mesh is generated with snappyHexMesh and was tested for one cylinder in laminar flow and Re = 100. This grid will be referred to as laminar snappy. The computational domain is 15D in x-direction and 10D in y-direction. The cylinder is located 5D from the inlet, 10D from the outlet and 5D from the upper and lower boundaries. This domain is smaller than many of the domains used in the literature, but the domain size is chosen based on the convergence study conducted in the project thesis. In the project a larger domain was tested and the results were not affected significantly and proved that the results were not affected by far field effects. The boundary conditions are also the same. This is also done to have comparable results.

The mesh has a circular refinement region stretching 1D out from the cylinder surface. This region has a refinement level 3. The mesh as also a squared refinement region behind the cylinder with a refinement level 2, to capture the vortex shedding.

The background mesh has the cell size $\Delta x = 1.4$ and $\Delta y = 1.56$, refinement level 2 has cell size $\Delta x = 0.35$ and $\Delta y = 0.39$ and refinement level 3 has cell size $\Delta x = 0.175$ and $\Delta y = 0.195$.

The results are given in Table 12 and the lift and drag coefficient are given in Fig. 37 and 38.

Table 12: Laminar study with snappyHexMesh.

Re [-]	dt [s]	$C_{D_{rms}}$ [-]	$C_{L_{rms}}$ [-]	St [-]
100	0.01	1.4903	0.2506	0.1750

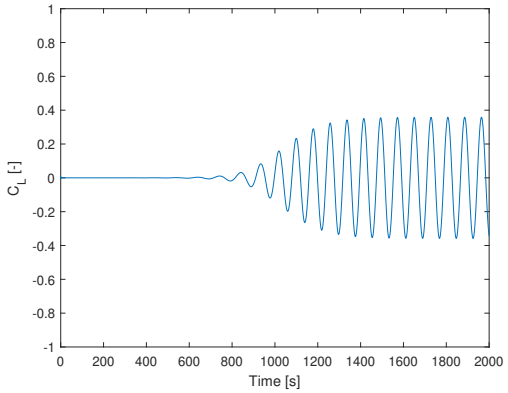

Figure 37: Lift - laminar snappy.

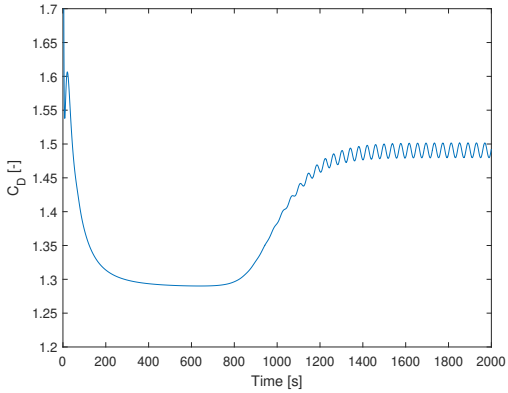

Figure 38: Drag - laminar snappy.

Table 13 shows an overview of the previous studies result for Re = 100. The results from the laminar study conducted in the project is also given in the Table 13 as project (blockMesh). The present results are also given for comparison.

Table 13: Laminar comparison.

	$C_{D_{rms}}$ [-]	$C_{L_{rms}}$ [-]	St [-]
Present results (snappy)	1.4903	0.2506	1750
Project (blockMesh)	1.4924	0.2565	0.1750
Rajani et al. [29] (2D RANS)	1.3353	0.1792	0.1569
Rosetti et al. [32] (2D URANS)	1.38	-	0.17
Park et al. [27] (Numeric)	1.33	0.3321	-
Singh et al. [36] (2D LES)	-	0.319	0.1643

The results obtained with the unstructured grid are almost identical to the results obtained with the structured mesh. The St is the same and the drag and lift coefficients are only slightly smaller than the results with the structured mesh. The drag coefficient for both the structural and the unstructured mesh are higher than the reference solutions. The study conducted by Singh et al. showed that St becomes closer to 0.2 for Re = 200 than for Re = 100.

The drawbacks with the unstructured mesh is the distorted cells that are created close to the body as shown in Fig. 39. This types of cells are not an issue with a structural mesh, but for a laminar case they do not affect the solution significantly. They can, however, give problems when considering higher Re and the boundary layer is more important.

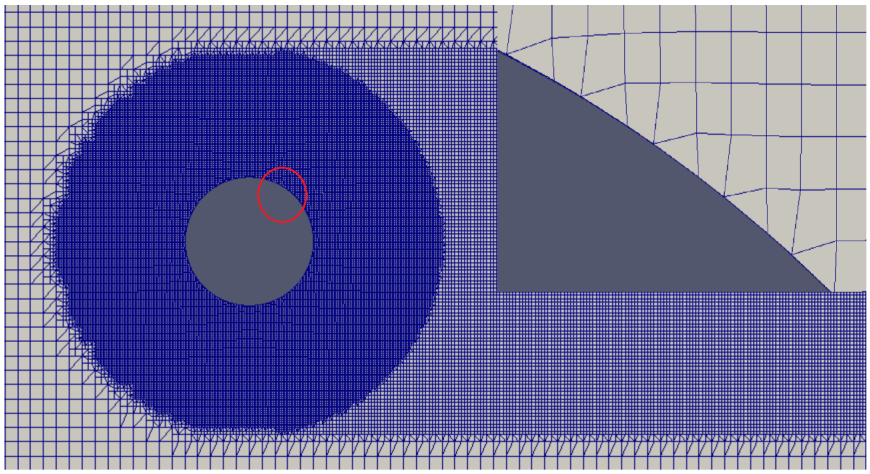

Figure 39: Critical area of the unstructured mesh for fixed cylinders.

6.2.2 Turbulent

The simulation parameters are the same as the ones given in Table 10. For the turbulent simulation a fine boundary layer is needed close to the cylinder. Two different meshes were tested. The first has four levers of refinement close to the body and the other has three. The mesh with four levels of refinement is referred to as grid number 1 and the grid with three levels of refinement is referred to as grid number 2. The background area with no refinement has a cell size with $\Delta x = 0.98$ and $\Delta y = 0.93$ for both grids.

Grid number 1 and 2 are shown in Fig. 40 and 41. The grid is similar to the one used in the laminar case, with a refinement region around the cylinder stretching 1D from the cylinder surface and another refinement region to capture the vortex shedding. The darker area close to the cylinder are the extra refinement added to capture the turbulent boundary layer. Figure 42 and 43 shows the mesh in this region. The Figure shows that grid No. 1 has smaller cells close to the body compared to grid No. 2. However, grid No. 2 has a larger area of refinement.

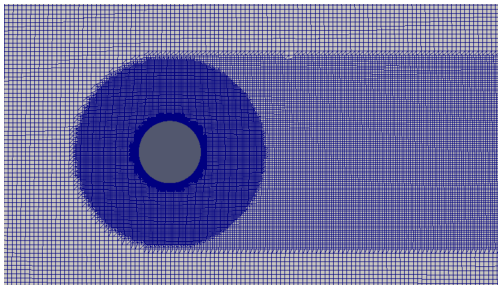

Figure 40: Unstructured mesh - Turbulent grid No. 1.

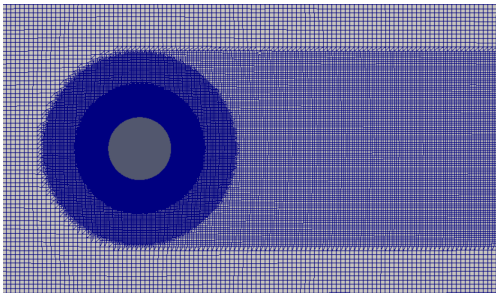

Figure 41: Unstructured mesh - Turbulent grid No. 2.

One of the drawbacks with grid generation with snappyHexMesh is the distorted cells that are created close to the body as discussed in the previous section. These cells did not affect the results for the laminar case, but for a turbulent simulation in high Re these cells makes the simulation highly unstable. Layers close to the cylinder is therefore needed. Six surface layers are used for mesh No. 1 and the first cell has a cell thickness of 0.015. Seven surface levels are used for mesh No. 2 and the first cell has a cell thickness of 0.017. The number of surface layers and the expansion ratio

are adjusted so that the last cell in the layer has approximately the same cell size as the cells outside the layer to ensure a smooth transition. If a finer or coarser mesh is used this needs to be adjusted.

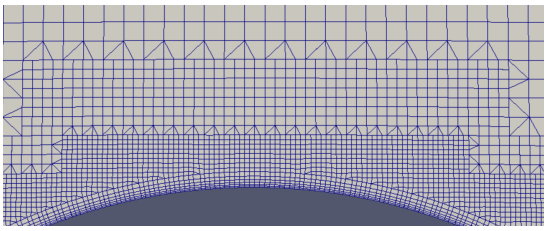

Figure 42: Boundary layer of unstructured grid - Turbulent grid No. 1.

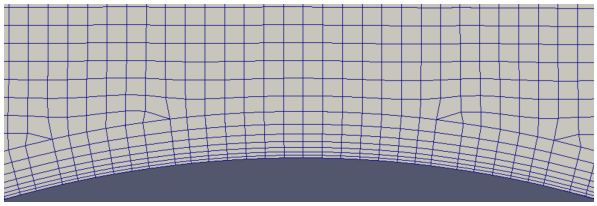

Figure 43: Boundary layer of unstructured grid - Turbulent grid No. 2.

Grid generation with snappyHexMesh is more time consuming than grid generation with blockMesh. To save time when testing grids a smaller domain is used. These results shown in Table 14 are given for a smaller domain, 10.5D x 6D. The upper and lower boundaries are located 3D from cylinder center. The inlet is located 3D from cylinder centre and the outlet is located 7.5D from cylinder centre.

Table 14: Initial turbulent study with snappyHexMesh.

Case	Re [-]	dt [s]	$C_{D_{rms}}$ [-]	$C_{L_{rms}}$ [-]	St [-]
Grid No. 1	7.65E6	0.01	0.5750	0.3126	0.3220
Grid No. 2	7.65E6	0.01	0.6212	0.3680	0.3080

The No. 2 was chosen for further study. This grid showed a smoother transition between the refinement regions. This is shown in Fig. 99 in Appendix II. The first mesh created smaller cells close to the body and the total number of cells is less than for grid No. 2. This might indicate that this grid is more cost effective, but the smaller cells requires smaller time step and the computational time might increase. The transition region between the refinement regions are too short for this grid and the flow resolution is suffering from this. This is shown in Fig. 98 in Appendix II.

6.2.3 Larger Domain

A simulation for a larger domain was conducted for the second mesh. This domain is 15D x 10D and similar to the domain used in the laminar case. The cell size is kept almost the same, $\Delta x = 0.98$ and $\Delta y = 0.97$. Table 15 shows the results for this simulation. Both the drag and lift coefficient in addition to the St decreased with a larger domain.

Table 15: Turbulent study with snappyHexMesh and larger domain.

Case	Re [-]	dt [s]	$C_{D_{rms}}$ [-]	$C_{L_{rms}}$ [-]	St [-]
Grid No. 2	7.65E6	0.01	0.5894	0.3631	0.2940

Figure 44 shows the lift and drag coefficients plotted against time. The transient phase is observed to continue until around $t = 800$ s. After 800 s the flow is stable and the boundary layer is fully turbulent. The lift coefficient is oscillating with mean value equal zero.

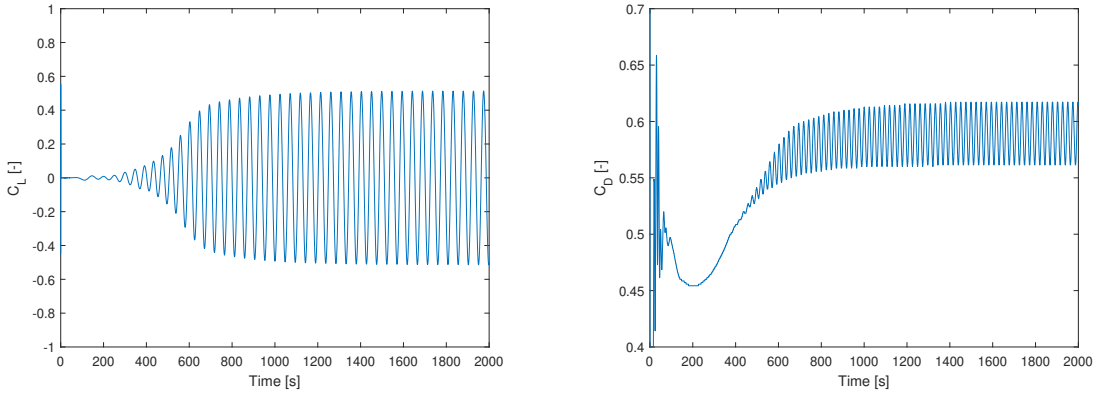

Figure 44: Lift and drag coefficients for fixed cylinder.

The lift force on a fixed cylinder in uniform flow oscillates with the same frequency at the vortex shedding frequency, $f_L = f_v$ and the drag force oscillates with twice the vortex shedding frequency, $f_D = 2f_v$. Figure 45 shows the power spectral density (PDS) plot of the lift and drag force. A singe peak is observed at 0.0207 1/s for lift and at 0.0414 1/s for drag. This shows that the observed $f_L = f_v = 0.0207$ and that $f_D = 2f_v = 0.0414$, exactly.

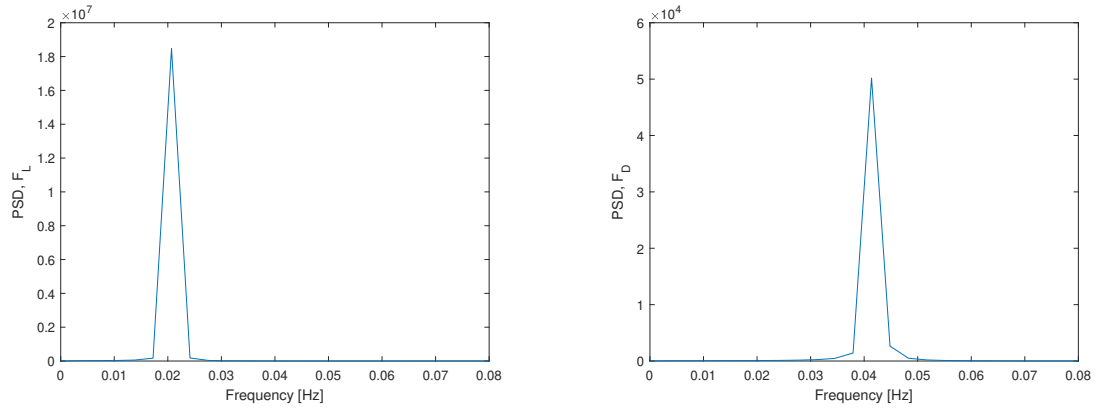

Figure 45: PSD for lift and drag force for fixed cylinder.

6.2.4 Discussion Turbulent Snappy

Squires et al. [37] studied the flow around a circular cylinder for $Re = 8 \times 10^6$ with two versions of 3D DES. The two method were tested for three grids with different refinement where the coarsest mesh has 1.47×10^6 cells and the fines has 9.83×10^6. The results shows that the C_D decreases for a finer mesh, while the St increases. For the finest grid the C_D were equal to 0.37 and 0.38 for the two methods, while the St equals 0.37 for both methods. Catalano et al. [9] conducted 3D LES, 3D RANS and 3D URANS simulations of the flow around circular cylinders for $Re = 1 \times 10^6$ and compared the results with experiments. Their results are included in Table 16. Ong et al. [26] investigated high Reynolds number flows around a 2D smooth circular cylinder using 2D URANS with $k - \epsilon$ model. Different Re were tested ($Re = 1 \times 10^6$, 2×10^6 and 3.6×10^6) and the results from the simulations with the highest Re is given in Table 16.

Table 16: Comparison between present results for fixed spar in turbulent condition and numerical results from the literature.

	Method	Re [-]	$C_{D_{rms}}$ [-]	$C_{L_{rms}}$ [-]	St [-]
Results	RANS	7.65×10^6	0.5894	0.3631	0.2940
K.D. Squires et al. [37]	(3D) DES	8×10^6	0.37-0.38	-	0.37
P. Catalano et al. [9]	(3D) LES	1×10^6	0.31	-	0.35
P. Catalano et al. [9]	(3D) RANS	1×10^6	0.39	-	-
P. Catalano et al. [9]	(3D) URANS	1×10^6	0.40	-	0.31
M.C. Ong et al. [26]	(2D) URANS	3.6×10^6	0.4573	0.0766	0.3052

Table 16 shows the present results together with numerical results found in the literature. The present $C_{D_{rms}}$ value is higher than the C_D obtained with 3D simulations which is in agreement with the theory stating that 2D simulations will over predict the drag force since spanwise variations is not considered. The $C_{D_{rms}}$ is also higher than Ong et al. [26] 2D result, but this can be explained by the higher Re used in the present study. The $C_{L_{rms}}$ is much higher than the one reported by Ong et al. [26] and St is lower than the results found in the literature. However, St is close to the 2D URANS results.
Numerous experimental results are published on the topic high Re flow around a circular cylinder and Fig. 46 shows some of the results in supercritical and transcritical regime for a smooth cylinder. Compared to Fig. 46 the present results are close to the line that presents the results by JONES et al.

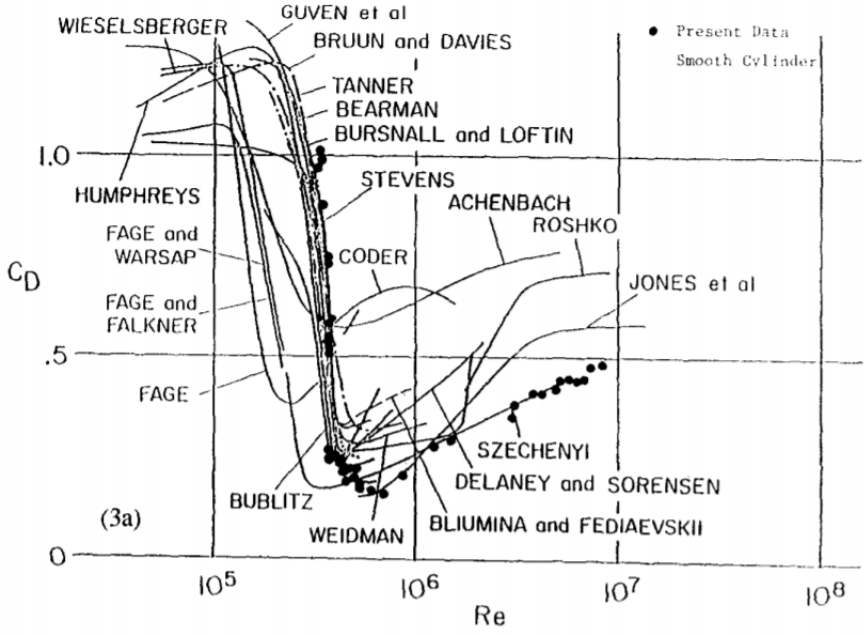

Figure 46: Experimental C_D values in supercritical and transcritical regime [35].

In the transcritical range, $Re \gtrsim 5 \times 10^6$, G. Schewe [34] reports a nearly constant $C_D = 0.52$. This is in agreement with the result given by Jones et al. [19] who observed $C_D = 0.5$, but smaller than the C_D measured by Roshko [33] and Achenback & Heinecke [3] who measured $C_D = 0.7$ and $C_D = 0.9 - 1$ respectively. The higher C_D measured by Roshko and Achenback & Heinecke are most likely due to the higher surface roughness used in these experiments. The present results are closer to the measured C_D given by Schewe as there is no surface roughness in the present numerical simulations.

The St value and the shape of the power spectra for C_L are in close agreement with the experimental results provided by Schewe [34]. He reported a $St = 0.29$ for $Re = 7.1 \times 10^6$. However, Schewe reports a maximum $C_{L_{rms}} = 0.38$ at $Re = 5 \times 10^4$ which is right before the drag crisis and a minimum $C_{L_{rms}} = 0.05$ for $Re > 2 \times 10^6$.

In general, the present results are within the range of experimental data and in reasonable agreement with the published numerical results.

Chapter 7

7 Analysis of an Unstructured Grid for Multiple Fixed Cylinders

7.1 Turbulent Semi-submersible

The change from structural too unstructured mesh was also done to save time when making the grid for the semi-submersible. After successfully making an unstructured mesh for one cylinder, the steps for making a mesh for three cylinders in a triangle cluster are few. Two more cylinders were made in the CAD program, blender, and the snappyHexMeshDict and the boundary condition files was modified to account for the two new cylinders.

An overview of the domain is given in Fig. 47. The red numbers inside the cylinders is the cylinder number and will be used when referring to the different cylinders. A larger domain is needed compared to the simulations for a single cylinder. The domain is 30.8D in x-direction and 17.1D in y-direction. The inlet boundary condition is located 9.2D from the center of cylinder 1 and 2. The outlet is located 17.9D from cylinder 3. The upper and lower boundaries are located 5.9D from cylinder 1 and 2.

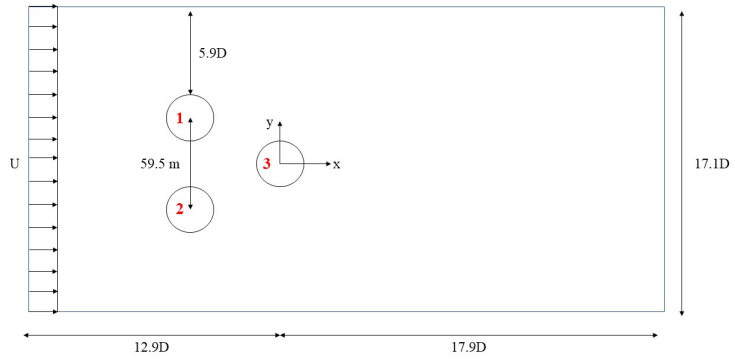

Figure 47: Computational domain for fixed semi-submersible.

Figure 48 shows the grid and a close up picture of the refinement regions around the cylinders. Refinement regions are similar to the one shown in Fig. 41 and the cells close to the cylinder is similar to Fig. 43. The boundary conditions are the same as for the turbulent case for the spar.

The grid is similar to the unstructured grid for one cylinder in turbulent flow. The difference is that there is no rectangular refinement region to capture the vortex shedding and the domain is larger. However, the mesh is refined compared to the unstructured mesh for the single cylinder. This was done after the small convergence study that was conducted for the single cylinder. A more in depth description of this convergence study is given in Section 8.1. A mesh size of $\Delta x = 0.80$ and $\Delta y = 0.80$ is used for the semi-submersible.

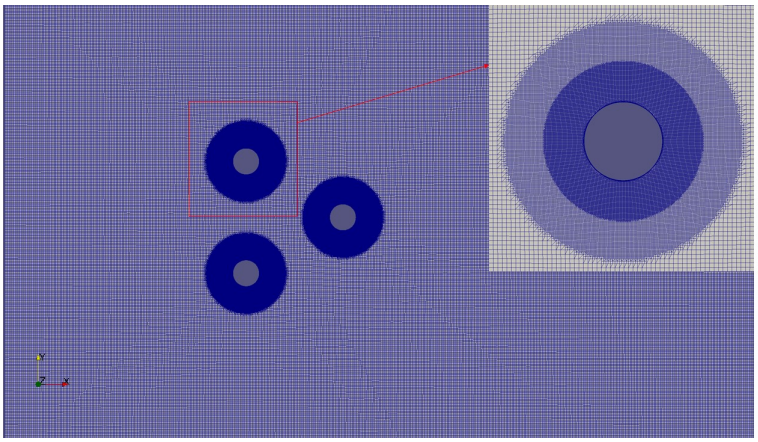

Figure 48: Grid and refinement regions for fixed semi-submersible.

To validate the changes in the mesh, the grid with only one of the cylinders was tested. The results are given in Table 17 and are close to the results presented in Table 15. Although, the lift coefficient is slightly larger and the St is slightly smaller, the results does not differ significantly and the grid is considered applicable.

The flow around cylinders in a cluster is rather complicated because the interference phenomena are highly non-linear. A side-by-side arrangement was therefore first studied before the flow around the semi-submersible was analysed. In the side-by-side arrangement cylinder 3 was removed from the simulation.

How the two cylinders interference depends on the distance between them. If the distance is sufficient large there will be no interference and the flow around each cylinders is the same as around a singe cylinder. As the distance becomes smaller the cylinders will start to interference. Zdravkovich [45] have defined two categories of interference for two cylinder arrangement; proximity-interference and wake-interference. Proximity-interference is direct interference of the vortex street formation for the two cylinders involved. This can occur for all arrangements where cylinders are in close proximity. Wake-interference affect only the vortex street formation behind the rear cylinder and does not occur for side-by-side arrangements. The proximity effects for two cylinders in side-by-side arrangement can be divided into three flow regimes based on the spacing between the cylinders. T/D is the non-dimensionalized distance called centre-to-centre transverse pitch ratio which is used to categorise side-by-side arrangements. Figure 100 in Appendix III shows an overview of the three flow regimes induced by the proximity effect. Single vortex street occurs for $1 < T/D < 1.1 - 1.2$, biased gap flow occurs for $1.2 < T/D < 2 - 2.2$ and coupled vortex street occurs for $2.7 < T/D < 4 - 5$. Five tandem flow regimes are also shown in the figure.

The pitch ratio T/D is equal 4.25 for cylinder 1 and 2 in Fig. 47 and a coupled vortex street is expected to occur for this case. The side-by-side case was tested with the same computational domain and inflow velocity as the case with one and three cylinders. The flow features agrees well with the reported features by Zdravkovich [44], Sumner et al. [38] and Williamson [42]. Figure 49 shows a coupled vortex street where both nearwakes are equal in size and mirror each other along the gap axis. The vortex shedding is in anti-phase synchronisation, meaning that the vortices are formed and shed in a symmetric manner on opposite sides of the deflected gap flow. The difference between anti-phase and in-phase synchronization is shown in Fig. 101 in Appendix III.

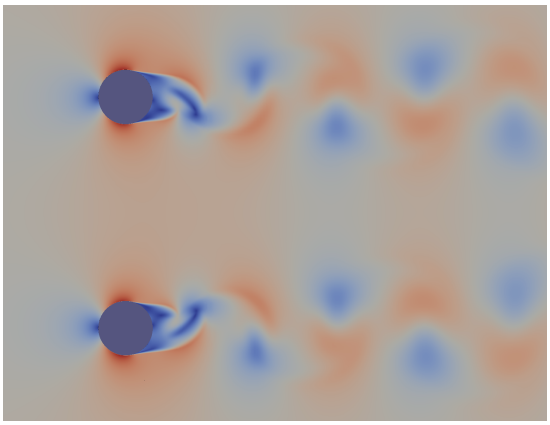

Figure 49: Side-by-side cylinders, coupled vortex street

Some of the same features that was observed for two side-by-side cylinders are also observed for the semi-submersible. At the beginning of the simulation, the same mirrored, anti-phased vortex shedding is observed for the two cylinders in front. This is shown in Fig. 50.

After some time the flow regime for the side-by-side cylinders change from anit-phase to in-phase vortex shedding. The in-phase vortex shedding is shown in Fig. 51. After a visual study of the flow, it was observed that the vortex shedding for cylinder 2 changed to be in-phase with cylinder 1. The spacing between the three cylinders is large enough to not experience bistable features. The observations are consistent with the observations done by Lam and Cheung for $l/d = 3.6$ [23].

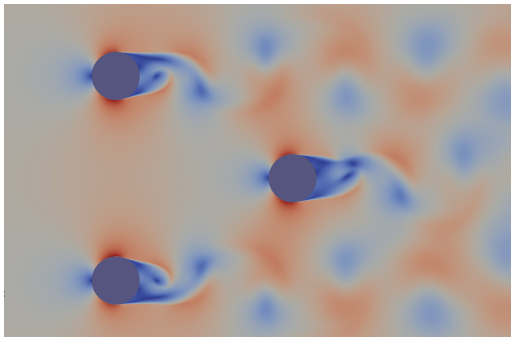

Figure 50: Semi-submersible - velocity field at t=700 s.

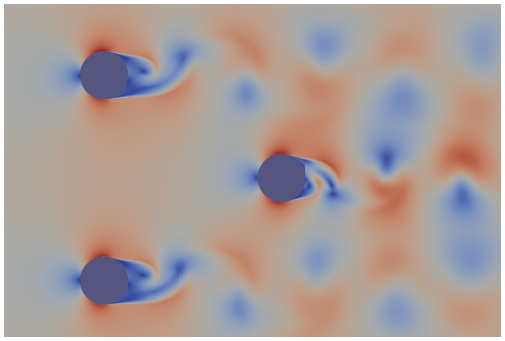

Figure 51: Semi-submersible - velocity field at t=2600 s.

The vortex street takes longer time to develop for cylinder 3. This is because of the shielding effect cylinder 1 and 2 provides. Cylinder 3 will experience smaller velocities than cylinder 1 and 2. The vortices shed from cylinder 3 is observed to blend with the vortices shed from cylinder 1 and 2.

Figure 51 also shows that cylinder 3 is in anti-phase with the two cylinders in front. This flow configuration results in that when cylinder 3 sheds vortices from the top these blends with vortices shed from cylinder 2 and when cylinder 3 shed vortices from the bottom these blend with vortices from cylinder 1. This is shown in Fig. 52 and 53. This anti-phase shedding between the two cylinders in front and cylinder 3 creates a stable wake for the total semi-submersible.

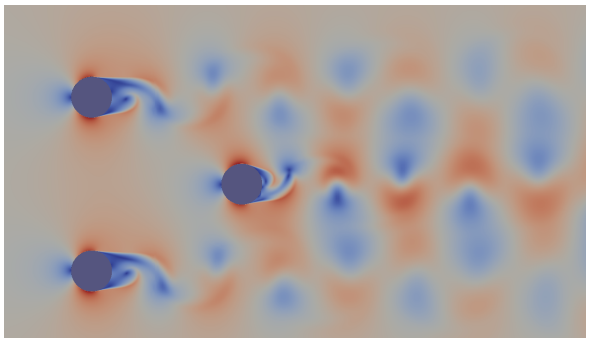

Figure 52: Semi-submersible - velocity field at t=2700 s.

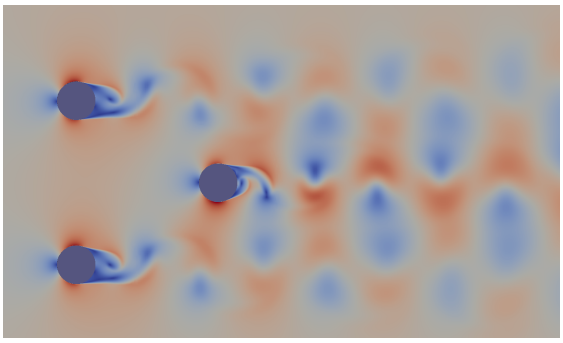

Figure 53: Semi-submersible - velocity field at t=3300 s.

Table 17: Results for individual cylinders in different arrangements.

Case	$C_{D_{rms}}$ [-]	$C_{L_{rms}}$ [-]	St [-]
Cylinder 1	0.5923	0.3671	0.2905
Cylinder 2	0.5948	0.3750	0.2940
Cylinder 3	0.7588	0.8971	0.2940
Side-by-side 1	0.6390	0.5109	0.2940
Side-by-side 2	0.6386	0.5097	0.2940
Singe cylinder	0.5779	0.4146	0.2870

Table 17 shows the $C_{D_{rms}}$, $C_{L_{rms}}$ and St for a single cylinder, two cylinders in side-by-side arrangement and three cylinders in the semi-submersible.

The results for the two cylinders in side-by-side arrangements are consistent with the observed flow features. The similar values for lift, drag and St are expected since the vortex shedding are identical in size and shedding frequency. The values are however slightly different from the values for a single cylinder. This is because the cylinders are affecting each other in the anti-phase regime. An in-phase regime is expected if there was no interaction. The slightly higher drag for cylinders in side-by-side arrangement compared to a single cylinder was also observed by Alam et al. [4].

Table 17 shows that for three cylinders, cylinder 2 and 3 have the same St while the St is reduced for cylinder 1. This is not consistent with the the results presented by Lam and Cheung for $l/d = 3.6$ [23]. They observed that the St for two side-by-side cylinders should have the same St and the St for cylinder 3 should be smaller. However, the difference is not significant and some variations are expected.

A reduction in both lift and drag is observed for the two side-by-side cylinders when the semi-submersible is considered. This reduction can be due to the wake disturbance caused by the third downstream cylinder. For two tandem cylinders the drag is know to be reduced for both cylinders involved as the distance between them decreases. The three cylinders can be viewed as a tandem arrangement with two cylinders in front and one in the back. A reduction in the drag for all three cylinders may be expected and can explain the reduction in lift and drag on cylinder 1 and 2.

However, both $C_{D_{rms}}$ and $C_{L_{rms}}$ are higher for cylinder 3, although lower values than for cylinder 1 and 2 was expected. To understand this, the flow features were examined. Figure 54 - 57 shows pressure fields for different time instant. A lower pressure field is observed at the top and bottom of cylinder 3 in Fig. 55, 56 and 56, compared to the pressure fields observed on cylinder 1 and 2. This indicate that cylinder 3 experience a larger pressure variation and can explain the larger lift coefficient

on this cylinder.

The Figures also shows that the low pressure regions in the wake behind cylinder 3 is lower than the low pressure regions behind cylinder 1 and 2. This indicates that cylinder 3 is experiencing larger alternating pressure variations than the two other cylinders. This can explain the larger drag forces acting on cylinder 3.

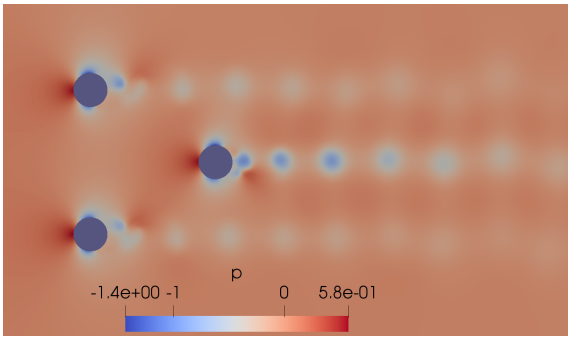

Figure 54: Semi-submersible - pressure field at t=2000 s.

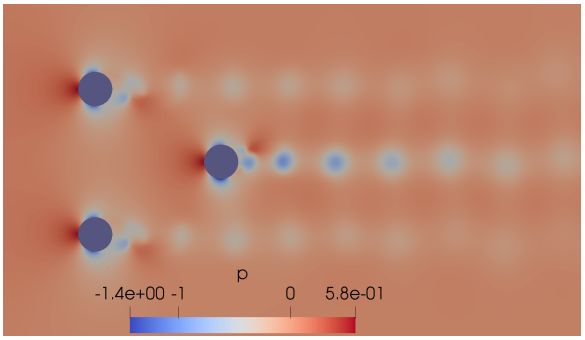

Figure 55: Semi-submersible - pressure field at t=3000 s.

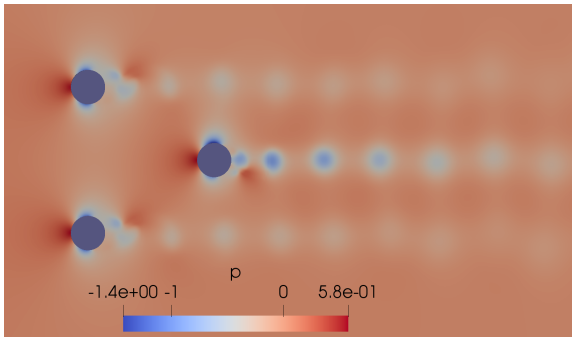

Figure 56: Semi-submersible - pressure field at t=3500 s.

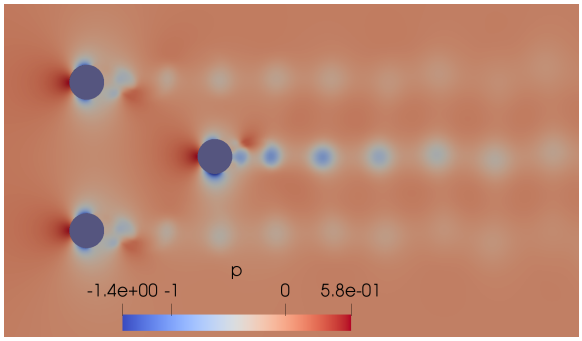

Figure 57: Semi-submersible - pressure field at t=4000 s.

Chapter 8

8 Physical Analysis of the Fixed Spar and Semi-submersible

The unstructured mesh for the fixed spar and semi-submersible were tested with various inlet velocities. The tested inlet velocities for the two platforms differs due to the different operational conditions. The results for the individual platforms are first presented before a comparison between the two.

8.1 Spar

The results for simulations with a fixed cylinder in uniform flow will be presented in this section. The final turbulent mesh with snappy is used for these simulations. The turbulent properties are the same as the ones given i Table 10. The inlet velocity is varied in the range 0.4 m/s to 1.4 m/s which corresponds to Re in the range $3.06 \times 10^6 - 1.07 \times 10^7$ and reduced velocity in the range $6.68 \leq U_r \leq 12.88$. The inlet velocity is increased with 0.1 m/s for each simulation, starting at the lowest velocity 0.4 m/s to the highest velocity at 1.4 m/s.
Two simulations with a coarser mesh and four simulations with a finer mesh were tested to verify that the results from these simulations had converged. The initial mesh is the second mesh that was tested with a larger domain in section 6.2.3. The cell size and total number of cells in the domain is given in Table 18. The mesh size is given for an unrefined cell as snappy uses this cell size as staring size for refinement.

Table 18: Mesh size for unrefined cell in Snappy.

	Δx [m]	Δy [m]	Number of cells
Initial Mesh ($*$)	0.98	0.97	92899
Coarser Mesh ($\triangle$)	1.4	1.4	45328
Finer Mesh ($\bigcirc$)	0.65	0.65	207023

The root-mean-square of the lift and drag coefficients are given in Fig. 58. The lift is increasing for $Re < 7.65 \times 10^6$ with about 17%, from 0.3003 to 0.3517. For $Re > 7.65 \times 10^6$ the lift is decreasing. The results for the initial mesh are close to the results for the finer mesh and indicates that the solution has converged. The drag are continuously decreasing with a small negative slope when Re increase. The results are close to the results for the finer mesh. Both lift and drag are decreasing when the grid is refined which is expected.

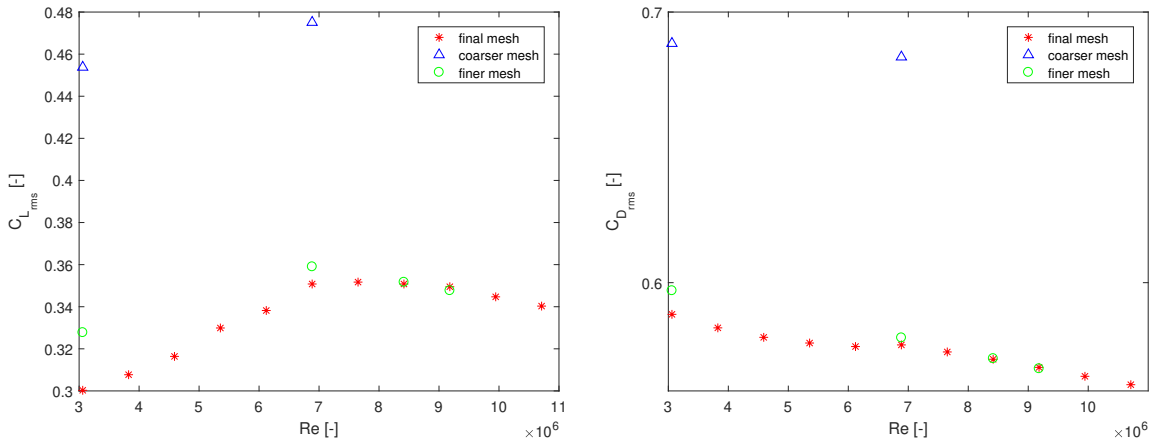

Figure 58: Lift and drag coefficient for a fixed spar.

Figure 59 shows that most of the St is found in the range 0.29-0.3 for the studied range of Re. The St is decreasing for $4.59 \times 10^6 < Re < 8.42 \times 10^6$ before the value increases for $Re = 9.18 \times 10^6$. For $Re > 9.18 \times 10^6$ the St decreases again.

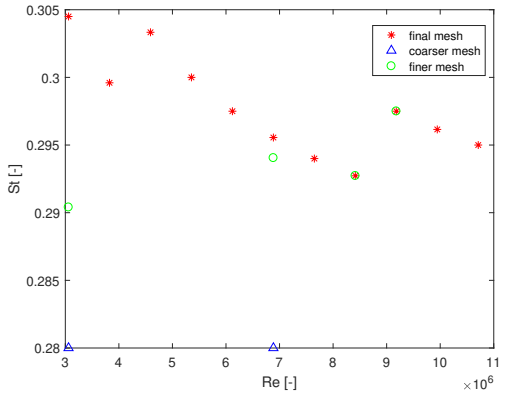

Figure 59: St for a fixed spar.

8.2 Semi-submersible

The simulations for the semi-submersible was conducted for 0.4 m/s $\leq U \leq$ 2.07 m/s. This corresponds to a reduced velocity range $3 \leq U_r \leq 15.4$ and a Reynolds number range of $3.06 \times 10^6 \leq Re \leq 1.58 \times 10^7$. The lift and drag coefficients are computed for the total platform by adding together the lift and drag forces on the three individual cylinders. The increase in the reference area is accounted for. The natural frequency is found by a fourier transformation of the total lift force.

Figure 60 shows the root-mean-square of the lift and drag coefficients for the total semi-submersible. The drag coefficient shows the same decreasing trend for higher Re as the C_D for a single cylinder. However, the drag coefficient only decreases with 7.2% from $Re = 3.06 \times 10^6$ to $Re = 1.58 \times 10^7$ so the slop is small. A larger difference is observed in the lift coefficient and a 55.87% increase in $C_{L_{rms}}$ is observed between the smallest and largest lift coefficient. This indicate that the total lift force acting on the semi-submersible depends more on the Re than the total drag force.

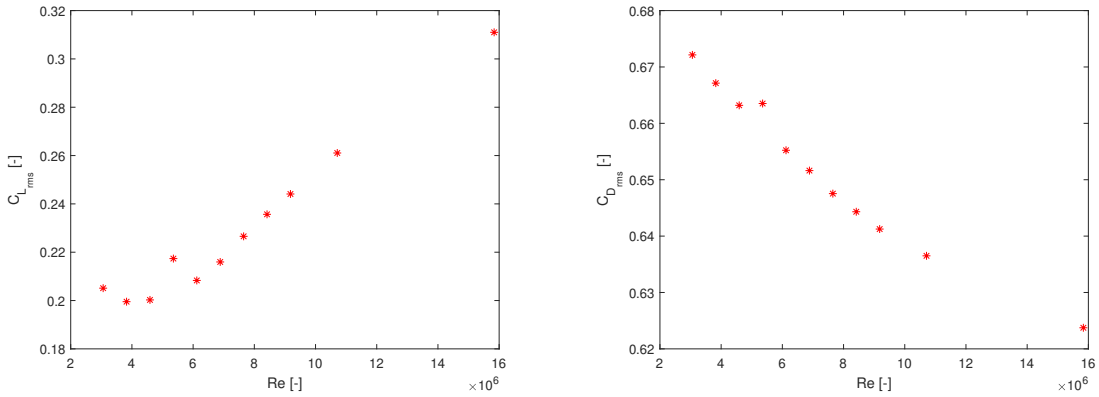

Figure 60: $C_{L_{rms}}$ and $C_{D_{rms}}$ for fixed semi-submersible.

The St for the semi-submersible is given in Fig. 61. The variations in St is small as the smalles St is

0.2886 and the largest is 0.2993, which makes a difference of 3.6%. For the different Re, but a general trend of an increasing St for increasing Re is observed.

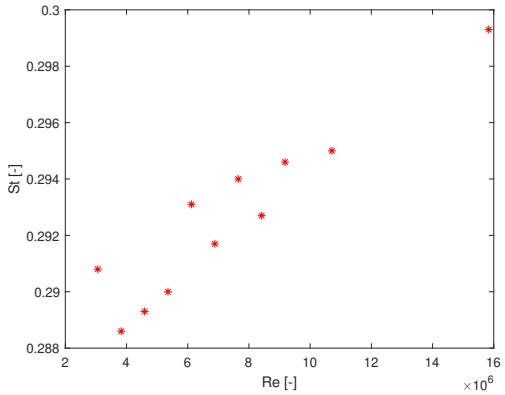

Figure 61: St for fixed semi-submersible.

The plots of the lift and drag coefficients for $U = 1$ m/s are given in Appendix IV. The individual graphs of the lift and drag coefficients for cylinder 1 and 2, given in Fig. 102 to 105, shows that the three cylinders are interacting. In the C_D plot for cylinder 1 and 2 two frequencies of drag force oscillation seems to be present where one seems more dominant and causes larger drag forces than the other. In the drag plot for cylinder 3, two frequencies are also observed. The second frequency seems to occur at the same time as cylinder 2 starts to change vortex shedding phase to be in-phase with cylinder 3. Around time equal $t = 2100$ the two vortex shedding for the side-by-side cylinders starts to be in-phase and Fig. 109 this corresponds to the time where the two frequencies becomes one and steady state is achieved for the total platform.

8.3 Comparison Between Spar and Semi-submersible

Figure 62 shows a comparison between the root-mean-square of the drag and lift coefficients and the St for the fixed spar and the semi-submersible for reduced velocities in the range $3 \leq U_r \leq 9$.

The $C_{L_{rms}}$ for both platforms increases for increasing U_r. The $C_{L_{rms}}$ for the spar is also observed to be larger than the total $C_{L_{rms}}$ for the semi-submersible by a factor of approximately 1.55. A decrease in $C_{D_{rms}}$ for both platforms is observed for increasing U_r. The $C_{D_{rms}}$ for the spar is smaller than the $C_{D_{rms}}$ for the semi-submersible, which is the opposite from what is observed for the $C_{L_{rms}}$.

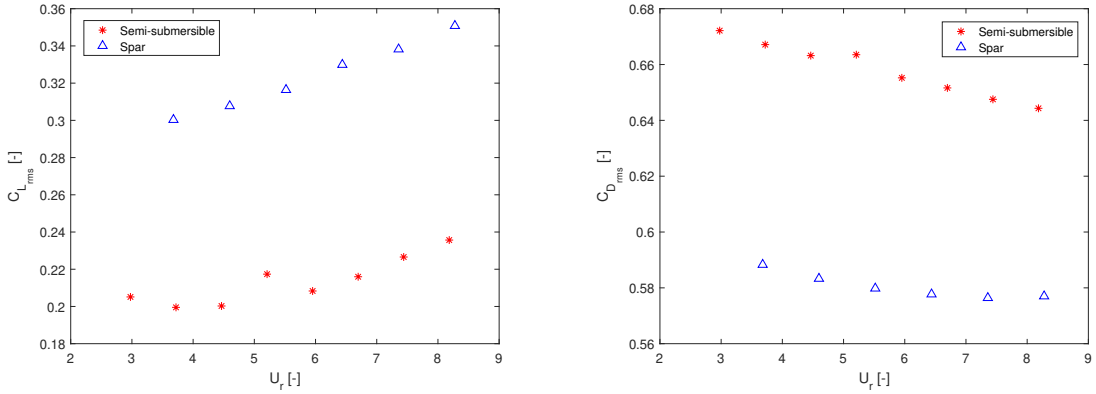

Figure 62: $C_{L_{rms}}$ and $C_{D_{rms}}$ for fixed Spar and Semi-submersible.

Figure 63 shows the St for the two platforms. The St for the two platforms shows an opposite trend, where the St for the spar decreases for increasing U_r while the St for the semi-submersible increases with increasing U_r. The St for the two platforms are also in different range of St. The St for the spar platform are in the range 0.2970-0.3050 and the St for the semi-submersible is in the range 0.2880-0.2945.

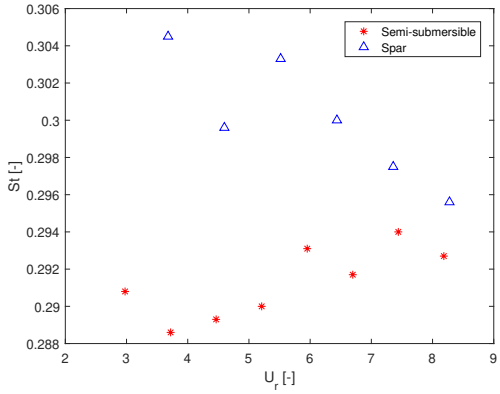

Figure 63: St for fixed spar and semi-submersible.

To understand why the total $C_{L_{rms}}$ decreases and the total $C_{D_{rms}}$ increases for semi-submersible, the total force on one, two and three cylinders are compared. Table 19 shows the total lift and drag coefficient for one, two and three cylinders for $Re = 7.65 \times 10^6$. The results for the single cylinder given in the table are the same results as given in Table 15.

Table 19: Results for the total systems.

Case	$C_{D_{rms}}$ [-]	$C_{L_{rms}}$ [-]	St [-]
Semi-submersible	0.6325	0.2209	0.2940
Side-by-side	0.6221	0.0065	0.3010
Spar	0.5894	0.3631	0.2940

The table shows that the total drag increases with the number of considered cylinders. The total lift is almost zero for two side-by-side cylinders and the value increases when the third cylinder is present

in the flow. The lift and drag coefficients are shown in Fig. 64 and 65 for two side-by-side cylinders.

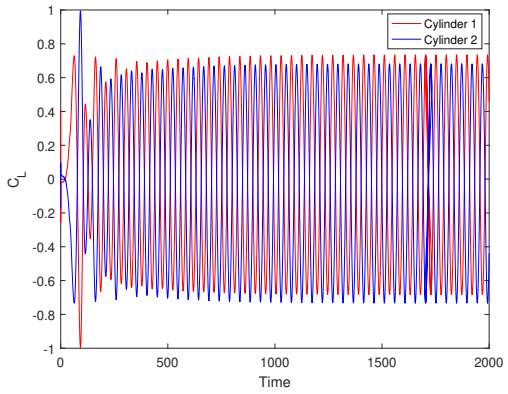

Figure 64: C_L for cylinder 1 and 2.

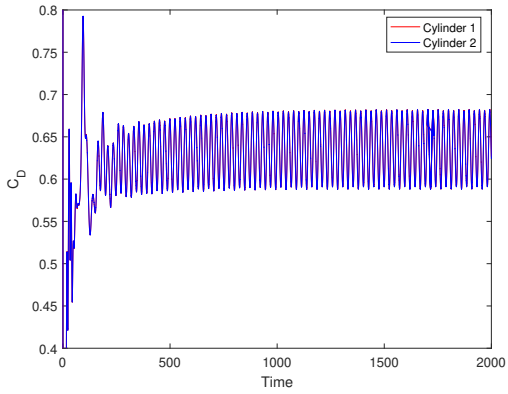

Figure 65: C_D for cylinder 1 and 2.

Figure 65 shows the evolution of the drag coefficient for the two cylinders. The coefficients are in-phase with almost the same amplitude. The total $C_{D_{rms}}$ for two cylinders are almost the same as the $C_{D_{rms}}$ for the individual cylinder. This is expected since the drag force acts in flow direction and no cancelling effects occur.

Figure 64 shows that the evolution of the lift coefficient are in anti-phase and cylinder 1 has a larger amplitude than cylinder 2. The lift force on the two cylinders are acting in opposite direction and the forces will cancel out when added together. This can explain the observed reduction in the lift force for two side-by-side cylinders compared to a single cylinder. The difference in amplitude can explain why the lift force is not exactly zero. Cylinder 1 has a larger positive amplitude than cylinder 2, but cylinder 2 has a larger negative amplitude. This implies that cylinder 1 will have a small positive mean value and cylinder 2 will have a small negative value. $C_{L_{mean}} = 0.0282$ for cylinder 1 and -0.0286 for cylinder 2. These values are not exactly the same and can explain that the total lift is not zero.

When a third cylinder is present in the wake of cylinder 1 and 2, the total drag increases. This is due to the larger drag forces that acts on cylinder 3. The lift increases drastically with the present of the third cylinder, which indicate that the third cylinder is the main contributor to the lift force. This can also been seen in Table 17, which shows that cylinder 3 has the largest lift coefficients.

8.4 Discussion

In this section the results presented in this chapter will be discussed in terms of observed trends and grid.

8.4.1 Spar

An decrease in the root-mean-square of the drag coefficient was observed for increasing Re. The drag is expected to increase with Re in this regime as shown in Fig. 46. M.C. Ong et al. [26] also experienced an decrease in C_D from 0.5174 to 0.4573 as the Re increased from 1×10^6 to 3.6×10^6. They compared their results to the URANS results reported by Catalano et al. [9] who reported a decrease in C_D with increasing Re. Ong et al. suggested that the difference could be in different implementations of the wall function.

The increase in lift coefficient for $Re < 7.65 \times 10^6$ and small decrease for $Re > 7.65 \times 10^6$ is consistent with the results given by Schewe [34] and the Fig. 3.

Figure 58 shows the results for the spar by using three different mesh sizes. The results for the coarser mesh differs significantly from the obtained results. The finer mesh gives results close to the final mesh and indicates that the results have converged. The clock-time increases with over three hours with the use of the finer mesh compared to the initial mesh. When comparing the difference in results, between the finer and the final mesh, with the increase in computational resources the mesh size in the initial mesh is a reasonable size to use. The maximum y^+ value for the initial mesh varies between 132 for $U = 0.4$ m/s to 419 for $U = 1.4$ m/s. The y^+ value for the highest velocity is in the upper region of what is considered reasonable y^+ values. The FLUENT user guide suggest a $30 < y^+ < 300$ when a wall function approach is used while other suggest that y^+ can be as large as 500. The maximum y^+ becomes larger than 300 for $U = 1$ m/s. The high y^+ values occur where the velocities close to the cylinder surface are highest, i.e. upstream for the separation point.

8.4.2 Semi-submersible

The drag coefficient for the semi-submersible shows the same decreasing trend as the spar. If this decreasing $C_{D_{rms}}$ for the spar is caused by the implementation of the wall function then it is expected that this can affect the results for the semi-submersible in the same way, which is consistent with the observations.

The lift coefficient does not show the same decreasing trend for $Re > 7.65 \times 10^6$ as for the spar. This might be due to less cancelling effects as the Re increases.

To save computational time, a refinement region to capture the wake was not used. However, a finer background mesh was used to compensate and the resolution in the wake region is satisfying. The flow features, discussed in Section 7.1, are in agreement with the literature. The effect of removing the refinement region on the results was studied by evaluating the difference between the results for one cylinder with and without the refinement region and it was observed that the results did not differ considerably. The simulation without the refinement region was conducted by removing two of the cylinders in the grid for the semi-submersible. The grid used for the three cylinders are larger than the grid used for the spar and the larger grid could also affect the results. A domain study has done in the previous work and the results for the spar is independent of the domain size based on this study, but small numerical variations can occur.

A convergence study for the mesh size was not conducted for the semi-submersible as the mesh size for this grid is based on the results for the convergence study for the spar. From the tested mesh sizes for the spar only small variations are observed when reducing the mesh size from 0.98 to 0.65. A mesh size of 0.8 was chosen for the background grid for the semi-submersible, which is in between these two. This was done to take into account the results for the spar and because a finer mesh is desirable to compensate for the removal of the refinement region for the wake.

The y^+ value for $U = 2.07$ m/s has a maximum value around 600 which is too high. As previously discussed, the y^+ value becomes considerably large when U approaches 1.4 m/s and a finer grid should be considered. This should especially be considered for the semi-submersible as this platform is exposed to larger current velocities.

Chapter 9

9 Analysis of Dynamic Grid Generation Techniques

In this chapter the implementation of the equation of motion for a spring-mass system, representing a cross-section of the spar platform, will be presented. Two overset grids and one morphing mesh will be analysed and the performance of the grids will be evaluated base on decay tests and forced oscillation tests.

9.1 Equation of Motion - Numerical Model

The physical spar system was modelled as a mass-spring system where the mass represent a strip with thickness Δz. The numerical model of the spar is simplified by considering the spar as a uniform cylinder with $D = 14$ m and draft $d = 105$ m. The mass of this cylinder is equal to the the weight of displace fluid, $M = V\rho$. The added mass for a fully submerged body is equal to the mass of the body. The system is modelled as a spring-mass system as shown in Fig. 66 and the equation of motion for the system is:

$$\frac{M \cdot \Delta z}{d}\ddot{y} + \frac{B \cdot \Delta z}{d}\dot{y} + \frac{C \cdot \Delta z}{d}y = F^{3D}_{strip} \tag{54}$$

where M is the mass of the spar, B is the system damping and C is the system stiffness.

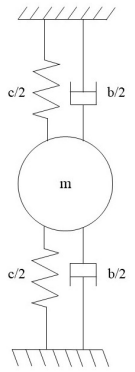

Figure 66: Spring-mass system - simplified model of spar cross-section

In Fig. 66 $m = \frac{M \cdot \Delta z}{d}$ is the mass of a strip, b is the damping for a strip, $b = \frac{B \cdot \Delta z}{d}$, and c is the stiffness for a strip, $c = \frac{C \cdot \Delta z}{d}$. B is calculated as 1% of critical damping, $B_c = 2\sqrt{CM}$.

9.2 Simple Overset Grid

A simple overset grid is created by merging two structural meshes made with blockMesh. The background mesh consists of one rectangular block while the cylinder mesh consists of eight curved blocks. The previous made blockMeshDict was reused for this purpose. The outer blocks were removed and the vertices renumbered. A coarse overset mesh is shown in Fig. 67. The most critical aspect with overset meshing is the interpolation areas between the overset patch and the background mesh. A rule of thumb is to keep the cell size difference of the overset patch and the background where the overset moves not larger than two times. To reduce the interpolation error the cell size difference should be as small as possible.

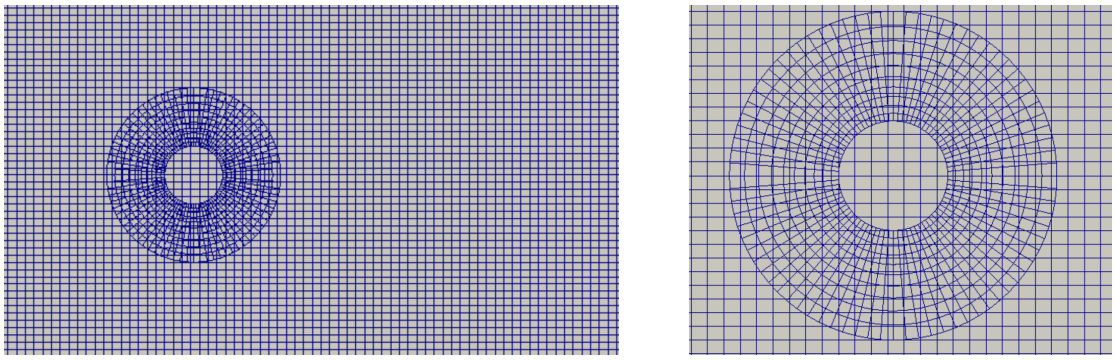

Figure 67: Simple overset grid.

The overset mesh was first tested for a laminar case with a fixed cylinder. This was done to quickly check that the background grid and the overset grid were communicating successfully. The background grid has a cell size of $\Delta x = 2.1$ and $\Delta y = 1.75$. The $C_{D_{rms}} = 1.5449$, $C_{L_{rms}} = 0.2414$ and $St = 0.1750$. The results are consistent with the laminar results obtained with the unstructured mesh. The cell size is larger for the overset grid than the cell size used in for the unstructured grid and a higher $C_{D_{rms}}$ and $C_{L_{rms}}$ are expected.

After the laminar case gave consistent results the mesh was refined and a decay test was first preformed. The system is modelled as shown in Fig 66 and the equation of motion is given by Eq. 54. The simulation parameters are given in Table 20.

Table 20: Simulation parameters for simple overset grid.

T [s]	Δz [m]	d [m]	ρ $[kg/m^3]$	m [kg]	b $[\sqrt{\frac{N \cdot kg}{m}}]$	c [N/m]
128	1	105	1000	153938	0	743.5

The stiffness is found through the relation $T_n = 2\pi\sqrt{(m + m_a)/c}$, where $T_n = 128$ s. The decay test was preformed by introducing a small displacement in negative y-direction. This was done by changing the restLength of the springs in the DynamicMeshDict, letting one of the springs be in compression and one spring be stretched.
Figure 68 shows the displacement in y-direction as a function of time. The motion dies out as time increases.

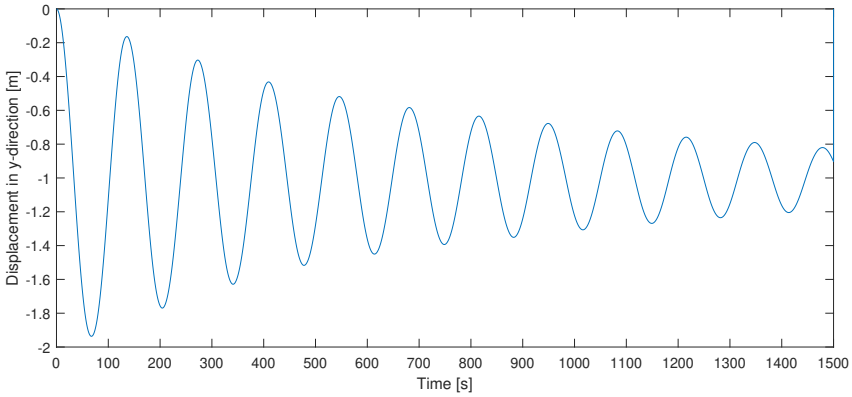

Figure 68: Decay test with simple overset grid.

The natural frequency is found by a fast fourier analysis of the vertical motion and gives $T_n = 136.99$ s. This is a larger period than the one calculated for the physical structure and gives a larger added mass. The added mass for this model is $m_a = 199488.38$ kg. This is 1.3 times larger than the system mass. The force signal obtained from OpenFOAM for the simulations with overset grid is noisy. This is due to the interpolation between the meshes and a butter filter was used before a fast fourier analysis of the force. The force signal before and after filtering is given in Appendix V.

To validate the added mass, a forced motion test was conducted. Changes in the dynamicMeshDict was preformed to use a different body motion solver. The cylinder was forced to move with harmonic motions with amplitude 0.5 and period 136.99 s.

The force signal from this test is also very noisy and this can indicate that the mesh is the interpolation region is too coarse. The filter is used to clean the data before F_a and ϕ was found. The added mass was calculated to be $m_a = 2860022.559$ kg, with $Fa = 330.9$ N and $\phi = -0.020$. This is 1.86 time larger than the mass. The lift force from the forced oscillation test is also given in Appendix V.

As the added mass in the forced oscillation test was almost twice the expected added mass and the noisy force signal indicates a poor mesh. A finer mesh was tested for a fixed turbulent case with uniform inlet velocity, but the computational time increased significantly as the solved used over 200 iterations for the pressure. This grid strategy was decide to be too time consuming to pursue and a morphing mesh was tested.

9.3 Morphing Mesh

A dynamic mesh with snappyHexMesh was tested to evaluate the applicability of this approach for future free motion study. A mesh without a refinement region in the wake was chosen since the wake region will vary as the cylinder moves. A decay test was first preformed to verify that the numerical system has the same natural period as the real system. The simulation parameters used is similar to the ones given in Table 20, except that $\Delta z = 0.1$. This makes $m = 15393.8$ kg and $c = 74.35\ k/s^2$. Figure 69 shows the displacement of the cylinder during the decay test.

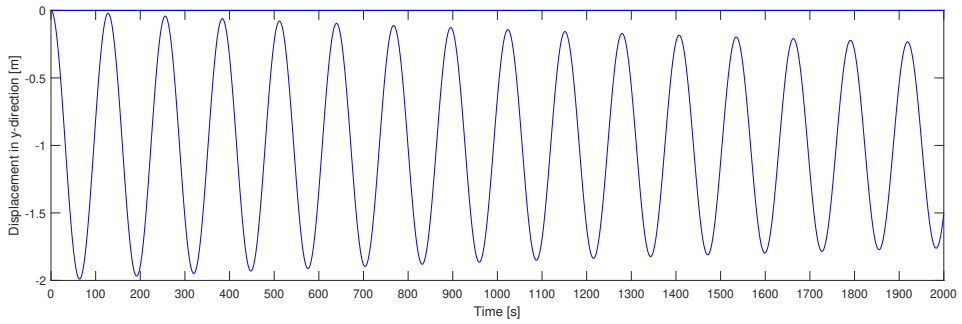

Figure 69: Decay test with morphing mesh.

Figure 114, in Appendix V, shows the lift force acting on the cylinder during the decay test. This force signal is completely smooth, as no interpolation is used and no filtering is needed before the fast fouier analysis. The decay test resulted in a natural period of 125 s for the spring-mass system and an added mass of 14032.88 kg. This added mass is closer to the theoretical added mass than the added mass found with overset.

Forced motion was also conducted to validate the added mass from the free decay test. The cylinder was forced to move with harmonic motions with amplitude 0.5 and period 125 s. The forced body

motion resulted in a force amplitude equal 19.52 and $\phi = -0.017$. Formula gives an added mass equal 15428.05 kg, which is close to the mass of the strip.

The morphing mesh gives better results in terms of natural period and added mass than the overset mesh. Morphing meshes are known to have problems when considering large motions. The system was therefore tested in uniform flow with $U = 1$ m/s. The simulation crashed after 300 s as a result of too deformed cells in the area where the cells are compressed.

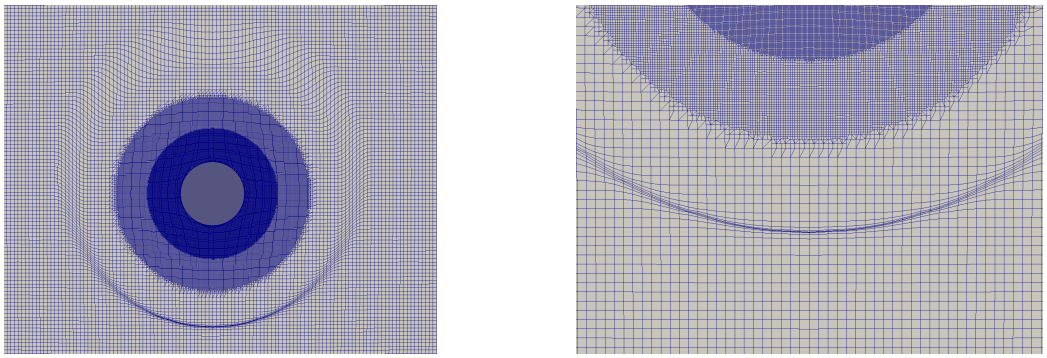

Figure 70: Large motion with morphing mesh.

Figure 70 shows that the deformed region of the grid is too small to handle the motions. The size of the deformed area can be controlled in the DynamicMeshDict and a larger area was allowed to deform to account for the large motion. Although a larger area is allowed to deform and the solution no longer crashes, the morphing cells are heavily deformed. The results for this mesh in uniform flow with $U_r = 3.57$ is presented in Section 10.1. The results are not consistent and the mesh experience too large motions.

9.4 Overset-Snappy

As the simple coarse overset grid with two structural meshes produces bad results and the dynamic mesh with snappy experienced too large motion an overset grid combining snappy and overset was tested.

A square grid 35×35 with cell size $\Delta x = 1.2$ and $\Delta y = 1.2$ was used as the background mesh for the snappy. The total domain is 25Dx20D. The refinement around the cylinder is equal to the refinement used for the morphing mesh, expect the larger cell size. However, the cell size closes to the body, in the boundary layer, is kept the same. To reduced the interpolation error the cell size in the background mesh for the overset is equal to the cell size in the background for snappy. Figure 71 shows the overset grid and the transition between the overset mesh and the background mesh.

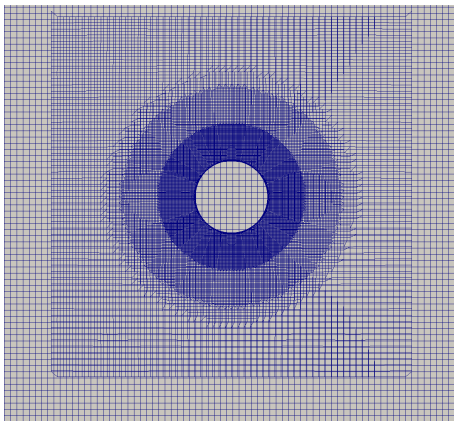

Figure 71: Overset with snappy-grid.

This mesh is a compromise between the two previous tested dynamic meshes. The overset features allows large motions which proved to be an challenge for the morphing mesh. The trade of is a coarser grid than the grid used for the morphing mesh to save time as the overset calculations are more time consuming than the morphing mesh calculations.
A decay test and a forced oscillation test were preformed with this grid. The decay test was preform with the same parameters as the morphing mesh, but a 1% of the critical damping was added. Figure 72 shows the displacement in y-direction for the cylinder during the decay test.

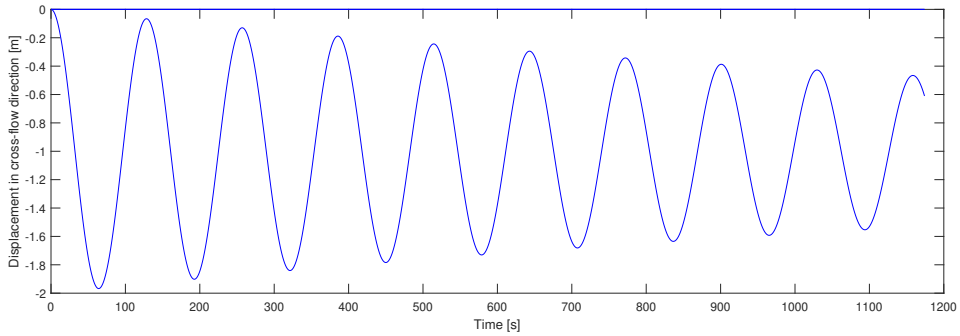

Figure 72: Decay test with overset snappy.

The natural frequency calculated from the lift force is $f_n = 0.0077$ 1/s and gives a natural period of $T_n = 129.87$ s. This gives an added mass of 16297.84 kg. The forced oscillation test was performed with same procedure as previously described and resulted in an added mass of 17114.49 kg. The difference in added mass for free decay test and forced oscillation test is 5.01% and the difference in added mass for free decay test and theoretical added mass is 6.15%.

The lift force is from the two tests are given in Appendix VII and the reduction in noisy is large compared to the simple overset grid. This indicates that the interpolation error are reduced with this grid.

9.5 Summary and Discussion

This section gives a brief summary and discussion of the previously presented results. Table 21 gives a summary of the natural periods and the added mass from the decay tests and forced oscillation tests

for the different grids. The wanted natural period is 128 s and the theoretical 2D added mass is 153938 kg.

Table 21: Summary of the results for the different dynamic grid generation techniques.

Grid	T [s]	m_a^{2D} [kg] Decay	m_a^{2D} [kg] Forced motion
Theoretical	128	153938	153938
Simple overset	136.99	199488.38	2860022.6
Morphing	125	140338.8	154280.5
Overset snappy	129.87	162978.4	171144.9

The simple overset grid preformed poorly both in terms of the calculated natural period obtained from the decay test and the too large added mass obtained from the forced oscillation test. The force signals were considerably noisy and a finer mesh is too time consuming. This mesh was therefore considered unsuitable for further study.

The morphing mesh preformed significantly better, both in terms of natural period and added mass, than the simple overset grid. Interpolation errors are avoid with this mesh, but deformation of the mesh is expected to reduce the accuracy of the results when larger motions are considered.

The overset mesh with snappy resulted in a natural period closer to the wanted natural period than the morphing mesh resulted in. The added mass are accordingly larger for this mesh than for the morphing mesh. This mesh suffers from less interpolation error than the simple overset grid as the force signals are less noisy. The accuracy of this grid might be less than the morphing grid as this mesh is coarser to save computational time as overset grids requires more CPU time than morphing grids. However, this mesh is expected to preform better than the morphing mesh when larger motions are considered.

Both the morphing mesh and the overset mesh with snappy will be tested with uniform inflow velocity and there performance will be evaluated in the next chapter.

Chapter 10

10 Cross-flow VIM Analysis of Spar

10.1 Morphing Mesh

The morphing mesh technique was one of the dynamic grids chosen for further study. The system was first tested for $U = 0.4$ m/s, which corresponds to a $U_r = 3.57$. This is a U_r in the lower range where VIV is expected. The results are examined in terms of forces, displacement and vortex shedding frequency.

Figure 73 and 75 shows the lift and drag force on the cylinder in uniform flow with $U = 0.4$ m/s. The red rectangles shows the steady state part of the forces that is used to compute the power spectrum. The oscillation frequencies of the forces are found from the power spectrum.

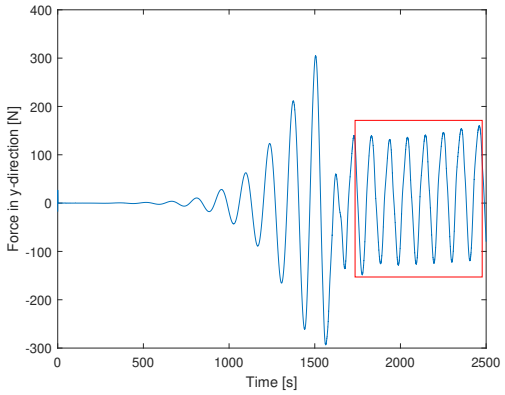

Figure 73: Steady part of lift force-morphing mesh.

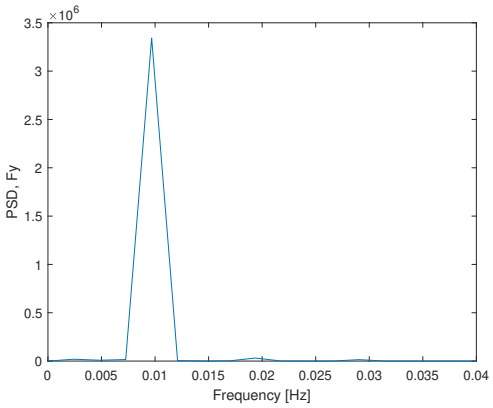

Figure 74: PDS of steady part of lift force-morphing mesh.

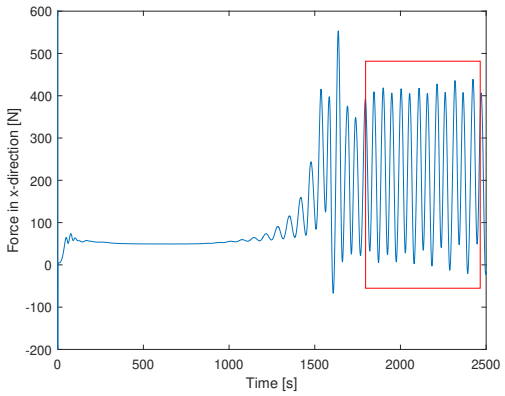

Figure 75: Steady part of lift force-morphing mesh.

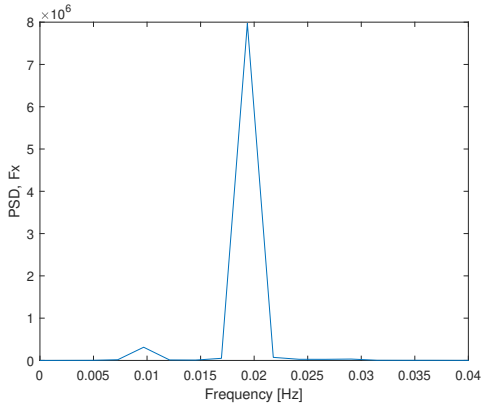

Figure 76: PDS of steady part of drag force-morphing mesh.

The correct window of the force signal has to be considered when computing the power spectrum. The window has to be taken from the steady state part of the solution and ensure a periodic signal. The

window for lift and drag force has to be the same.
The lift force is oscillating with a period of $T_L = 103.09$ s and the drag force is oscillating with a period equal $T_D = 51.55$ s. The lift force has exactly twice the period of the drag. According to the theory, the lift force on a fixed cylinder in uniform flow will oscillate with the same period as the vortex shedding period and the drag force will oscillate with half the period. This indicates that the vortex shedding period in this case is $Tv = 103.09$ s. These results are also consistent with the vortex shedding period, $T_v = 116.8$ s, observed for the fixed case at $U = 0.4$ m/s.
The cylinder is constrained to only move in cross-flow direction. The displacement of the cylinder is given in in Fig. 77. The cross-flow VIV amplitude, given as displacement divided by diameter, is plotted on the y-axis and time on x-axis.

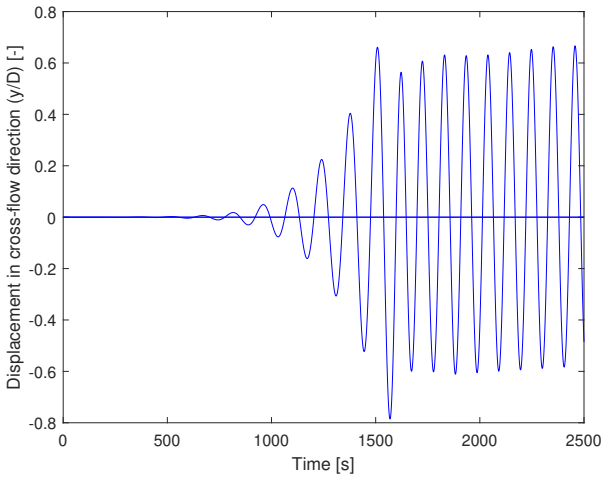

Figure 77: Cross-Flow displacement amplitude (y/D) - morphing mesh.

The amplitude of oscillation is $A = 0.65D$ when only the steady state is considered. This is twice the cross-flow VIV amplitude given by the DNV guidelines for this U_r which is around $A_{DNV} = 0.3$.
The cylinder is oscillating with a period of 104 s. This is close to the vortex shedding period and indicates VIV. The system is oscillating with a lower period than the natural period and the added mass is reduced. The added mass obtained from the decay test was 14032.9 kg, while the added mass in this case is 4976.05 kg.

Figure 78 - 83 shows the flow features for this case. A steady laminar wake is shown in Fig. 78. In Fig. 78 the turbulent transition has narrowed the wake and the wake has also become unsteady. Figure 80 shows the flow features in the transient state where the beginning of cylinder oscillations starts. The last two figure 82 and 83 shows the flow features in steady state conditions.

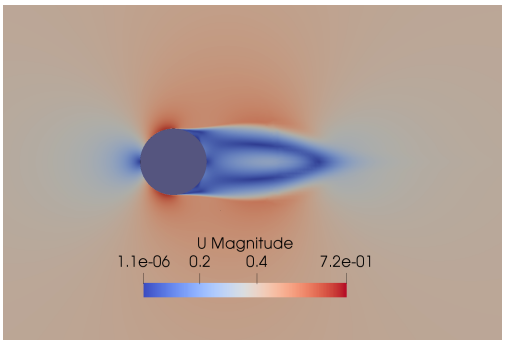

Figure 78: T=300 s - laminar wake.

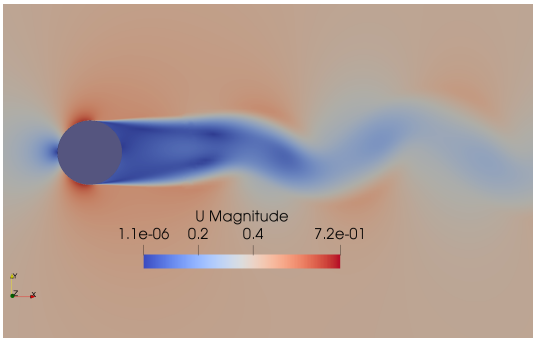

Figure 79: T=900 s - turbulent wake.

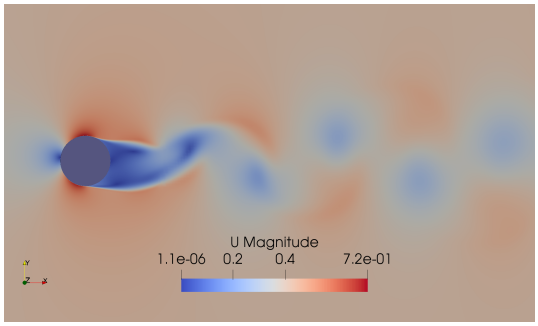

Figure 80: T=1200 s - transition state.

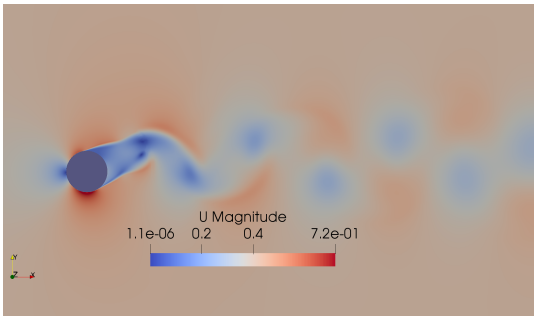

Figure 81: T=1300 s - transition state.

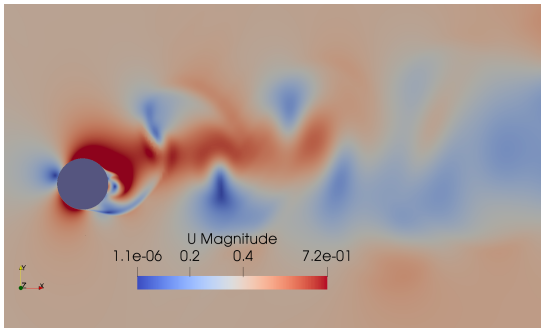

Figure 82: T=1900 s - steady state.

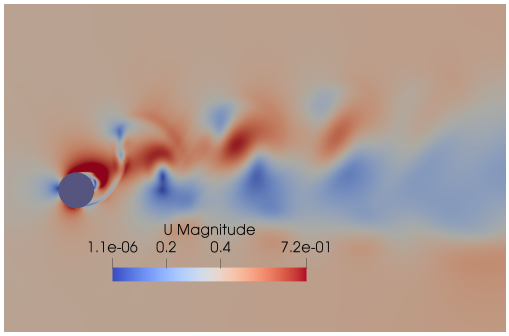

Figure 83: T=2300 s - steady state.

10.2 Overset with Snappy

The overset with snappy was first tested with uniform inlet velocity, $U = 0.4$ m/s and reduced velocity, $U_r = 3.71$. The lift and drag forces are analyst in the same way as described in the previous section and the time development of the forces are given in Fig. 84. The lift and drag oscillation frequencies are $f_L = 0.0093$ 1/s and $f_D = 0.0186$ 1/s. The corresponding periods are $T_L = 107.52$ s and $T_D = 53.76$ s.

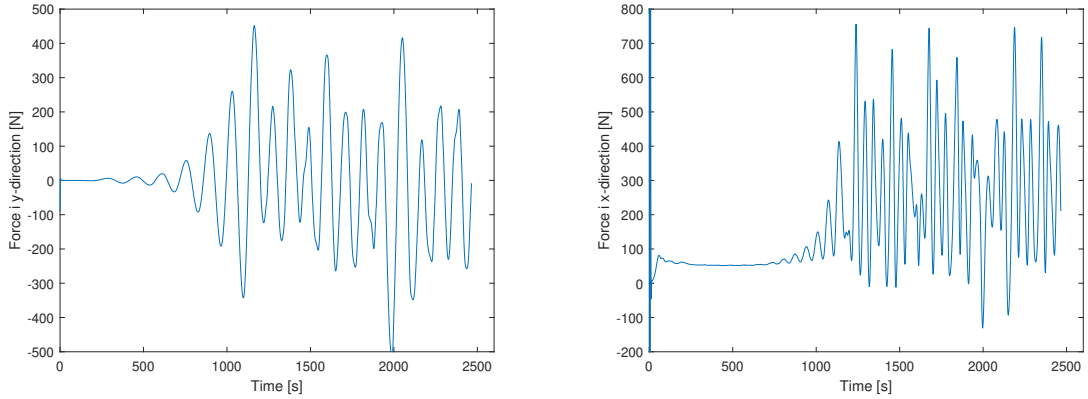

Figure 84: Lift and drag forces - overset Snappy, $U = 0.4$ m/s.

Figure 85 shows the dimensionless cylinder displacement as a function of time. The lift force oscillates with a varying amplitude and this is reflected in the amplitude of oscillation for the cylinder as the cylinder is oscillating with a varying amplitude. The cylinder oscillates with a period around 109 s and the amplitude of oscillation varies between 0.6D and 0.8D. An average value of 0.7D will be considered.

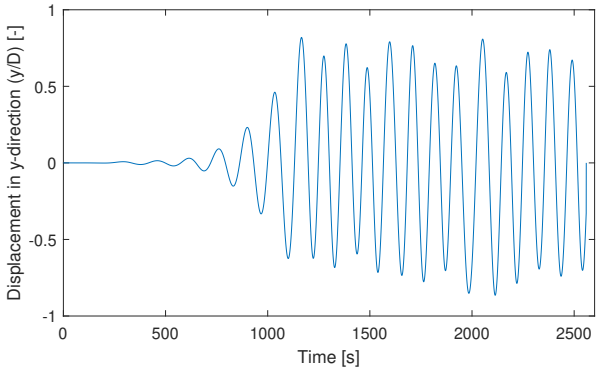

Figure 85: Cross-Flow displacement amplitude (y/D) - overset snappy.

The cylinder oscillates with a period close to the vortex shedding period and this period is close to the cylinders natural period. This indicates that the cylinder is in the lock-in region at this reduced velocity and large motions are expected to occur.

According to DNV guidelines the amplitude at $U_r = 3.7$ is expected to be around 0.2D and a amplitude between 0.6D - 0.8D is expected for U_r between 5-12. The results does not agree with the DNV guidelines and two smaller U_r, that, according to theory, should be outside the synchronization region was tested. An inlet velocity of $U = 0.1$ m/s and $U = 0.2$ m/s were tested to verify that a $U_r = 0.93$ and 1.85 will give oscillations outside the resonance region. These simulation resulted in a cross-flow amplitude of 0.0048D and 0.032D which is almost equal zero. The oscillation period are 525 s and 256 s and for both velocities, the cylinder is oscillating with the vortex shedding frequency.

Two unrealistic high velocities of $U = 1.8$ m/s and $U = 2.5$ m/s were tested to check if the upper outside region of lock-in could be identified. These velocities corresponds to reduced velocity $U_r = 16.70$ and $U_r = 29.19$. For $U_r = 16.70$ the period of oscillation is 86.96 s and equal to the vortex shedding

period. This period is much smaller than the natural period and the cylinder is outside the lock-in region. For $U_r = 29.19$ a smaller oscillation period of 71.94 s is observed. This oscillation period is also equal to the vortex shedding period and even further away from the natural period. The amplitude of oscillation are unrealistic large for these simulations. Figure 119 in Appendix VIII shows the amplitude of oscillation for $U = 1.8$ m/s. In both cases a large lift force is observed at the transient state of the simulations are this force is assume to trigger the large motions. This means that these large amplitude are not assumed to be connected to VIM. Figure 120 shows the lift force for $U = 1.8$ m/s and the large transient lift force is highlighted in the figure. To check this a ramp function was tested for $U = 1.8$ m/s. The ramp uses a linear function with slop 0.18. This allows for an increase in inlet velocity as a function of time. The velocity is increasing from 0-1.8 m/s over 100 s. However, large motions are also observed for this case, but the amplitude of oscillations varies from 0.75D-1.25D. The PSD of the lift force shows three peaks and the largest one is taken as the vortex shedding frequency. These variations were not observed for the case without the ramp function. 2% of the critical damping was introduced to the system together with the ramp function. A steady amplitude of oscillation just below 1D is observed and only one peak in the PSD is present. This is shown in Fig. 125 and 127 in Appendix VIII.

The summary of the results are given in Table 22 and 23. Table 22 shows results for the different uniform inlet velocity. Table 22 shows results for $U = 1.8$ m/s with the ramp function with and without 2% of critical damping.

Table 22: Results for spar in uniform flow.

U [m/s]	0.1	0.2	0.4	1.8	2.5
U_r [-]	0.93	1.86	3.71	16.70	29.19
y/D [-]	0.0048	0.032	0.7	1.3	0.852
T_osc [s]	525	256	109	86.96	71.94
T_v [s]	526.32	256.4	107.52	86.93	71.84

Table 23: Ramp function simulation with and without damping.

	U [m/s]	U_r [-]	y/D [-]	T_{osc} [s]	$T_v[s]$
ramp	1.8	16.7	0.75-1.25	75.19	75.24
ramp+damp	1.8	16.7	1	57.3	57.3

10.3 Discussion

10.3.1 Morphing Mesh

Results inside the synchronization region was obtained with the morphing grid. This is consistent with the U_r used in the simulation. However, the amplitude of oscillations is too high compared to DNV guidelines. The deformation of cells in a morphing mesh is know to affect the results when the motions are large and cell deformation severe.

The flow features are clearly affected by the deformation of the morphing mesh. The affected area of the solution is shown by the two red rectangles to the left in Fig. 86. The left and right regions in the left pictures are refereed to as region 1 and 2, as the number in the figure indicate. The cells in these regions are stretched as the cylinder moves in vertical direction and this causes the stripes in lighter shades in the figure. These stripes indicates that the grid experiences too large motions. The picture to the right in same figure shows the cells in region 1. The cells are deformed, but not has heavily as the picture to the left might indicate.

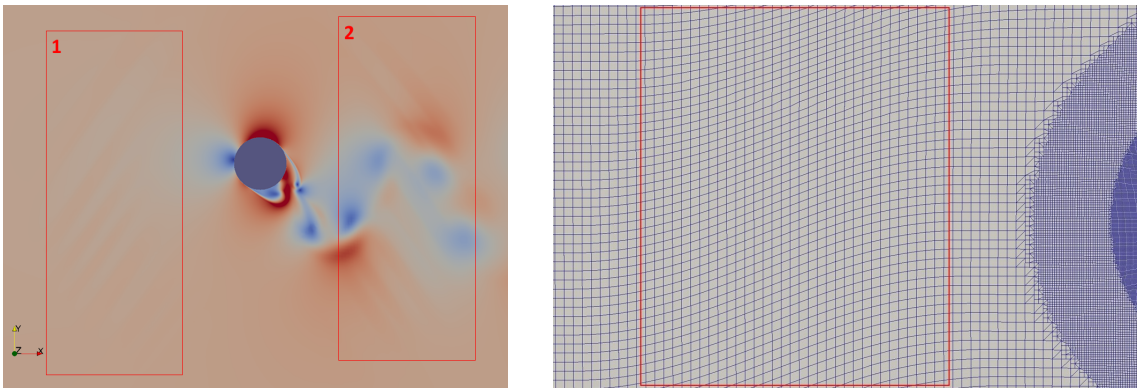

Figure 86: Deformation of the morphing mesh.

Figure 86 shows that the cell deformation is occurring some distance from the body and by studying the wake in Fig. 82 and 83 the deformed cells does not seems to affect the wake significantly. The results with the morphing grid proved to be consistent with the results obtained with the overset. This might indicate that deformed cells does not affect the results as much as first assumed.

10.3.2 Overset Snappy

Five velocities in the reduced velocity range 0.93-29.19 have been tested with the overset with snappy. The results are consistent in terms of period of oscillation and vortex shedding period. The periods are decreasing with higher velocities and for the reduced velocity in the lock-in range the cylinder is oscillation with a period close to the natural period. For reduced velocities outside the lock-in region the cylinder is oscillating with a period far from the natural period.

The amplitudes of oscillations for the $U_r = 0.93$ m/s and $U_r = 0.2$ m/s are as expected for these reduced velocities, but for higher U_r the amplitudes are too high compared to the DNV guidelines. For $U_r = 3.71$ the amplitude of oscillation is similar as the one observed with the morphing mesh.

Many references uses $St = 0.2$ or $St = 0.25$ when discussing VIV and DNV guidelines was suspected to also uses these standard values for St. The results from the simulations with a fixed cylinder gave a St in the range 0.2927-0.3045 and a higher St range is true for these simulations. For a fixed cylinder an inlet velocity of $U = 0.4$ m/s resulted in $St = 0.3045$. From the condition $U_r = 1/St = 5$, a $St = 0.3045$ gives a $U_r = 3.38$ which is close to the reduced velocity in this case. This indicates that for this study where higher St are considered, the range where the largest cross-flow VIV amplitudes are observed can occur for smaller reduced velocities. Kawamura et al. [22] studied the effect of the Strouhal number on the lock-in region for a circular cylinder in supercritical Re regions. They observed that the reduced velocity at the beginning of synchronization decreased for higher St. Figure 128 in Appendix 9 shows that in supercritical Re and $St = 0.29$ the lock-in vibration in lift direction start at a reduced velocity around 2.8. However, according to DNV guidelines the lock-in region ranges from $2 < U_r < 16$ and proves that the guidelines are consistent with the theory at least for the lower range. It also has to be considered that the DNV guidelines refereed to in this theses are for pipelines as vortex induced resonance mostly are studied for flexible slender structures. These structures are also exposed to to lower Re and this should be taken into account when applying these standards.

For $U_r > 1.86$ large lift forces are observed in the transient state of the simulation and it is suspected that this can trigger large motions at the beginning of the simulation that will be dominating throughout the simulation. For $U = 0.4$ m/s a large force around 400-500 N is observed at t=1200 s. For a fixed cylinder the force was not larger than 50-60 N at transient or steady state. A large lift force is also

observed in the transient state for $U = 1.8$ m/s and $U = 2.5$ m/s. Appendix shows the large lift force at $t \approx 100$ s for $U = 1.8$ m/s. This force occurs at the same time as the cylinder moves down almost 1D.

To avoid this large lift force at the beginning of the simulation a ramp function is used. The ramp function is used to increase the velocity linearly from 0 to 1.8 m/s over a time period of 100 s. The large peak in the lift force deduced with the use of the ramp function and are more varied amplitude of oscillation is observed. However, large peaks are still observed at e.g. 1.23D. In the plot of the PSD for the whole flit force three major peaks are observed. The largest peak was taken at the vortex shedding frequency as this frequency matches the oscillation frequency, but the origin of these frequencies can not be detected just from inspection of the PSD. However, the spring mass system is expected to have natural period and there is a possibility of the springs affecting the solution at these high velocities. As structural damping usually is present, 2% structural damping was applied together with the ramp function for $U = 1.8$ m/s. This resulted in a more steady oscillation with an amplitude around 1D. The lift force is also more steady and the high peaks in the force is avoided. The PSD of the lift force gives only one peak when damping is applied. The plot of the motion for this case is more similar to the plot given in Fig. 119, in Appendix VIII, but is more physical. The large force in transient state is avoided and the first displacement is reduced with around 0.5D. This implies that a ramp function and damping should be applied for higher velocities. The slope of the ramp function should be tested more and a smaller slope might give better results. The amount of damping should also be evaluated in more depth.

The mesh and flow features are studied for further understanding of the results. For small motions the wake is similar to that of a fixed cylinder as shown in Fig. 87. The figure shows the vortex shedding as the cylinder is exposed to an inlet velocity of $U = 0.1$ m/s.

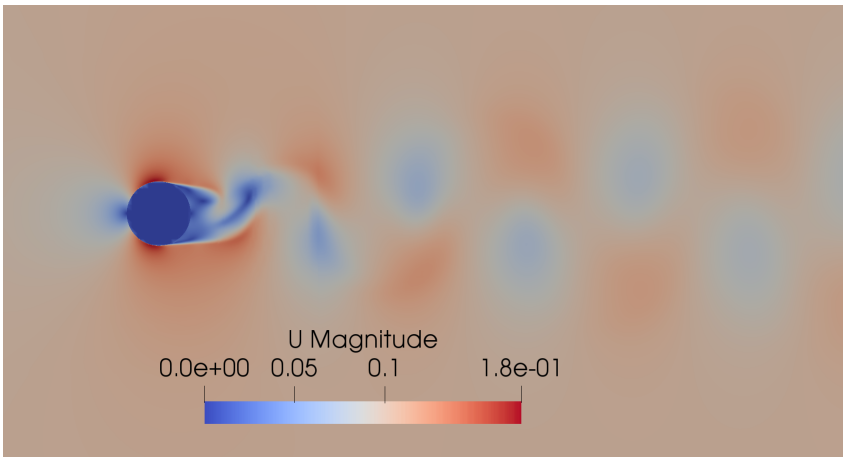

Figure 87: Steady wake at steady state for $U = 0.1$ m/s.

Pressure calculation is observed inside the cylinder when the pressure filed is visualized. This is shown in Fig. 88. This issue was observed in all simulations conducted with overset grid. For higher velocities and larger motions the overset grid faces some numerical issues in the interpolation region. Figure 89 shows the vortex shedding as the cylinder is exposed to an inlet velocity of $U = 1.8$ m/s. The information about the velocity is not transferred between the overset patch and background grid in a satisfying way. This can cause a lag in information transport and reflection. This seems to be an issue for all velocities, but the effect increases with the velocity and amplitude of motion. By close inspection, some lagging is observe in the pressure in Fig. 88 also.

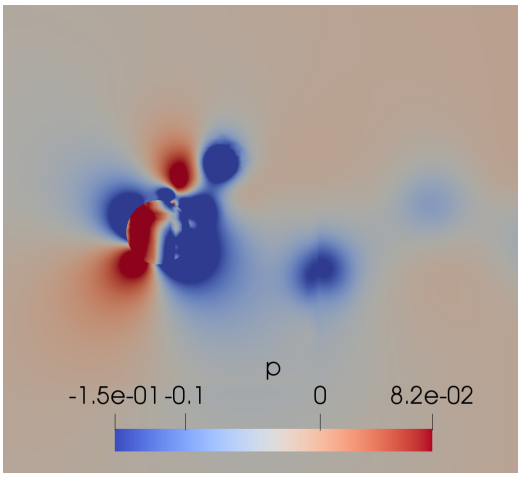

Figure 88: U=0.4 m/s - pressure inside cylinder between background mesh and overset patch.

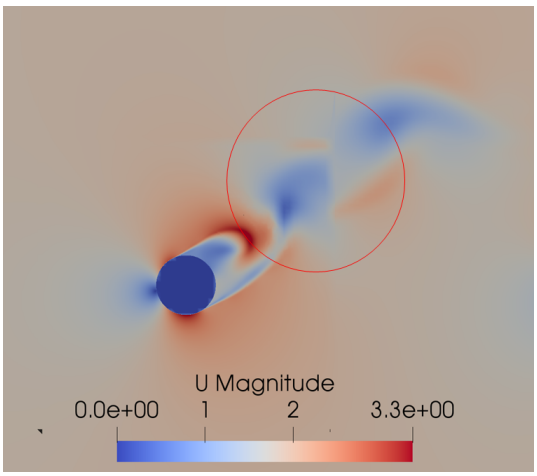

Figure 89: U=1.8 m/s - lag in communication between background mesh and overset patch for the velocity.

The overset grid with snappy also faced some issues in the corners of the overset patch. This is shown in Fig. 90. To the left in the figure, the right down corner cell is stretched as the grid moves up and to the right in the figure, the right top corner cell is stretched downwards as the mesh moves up.

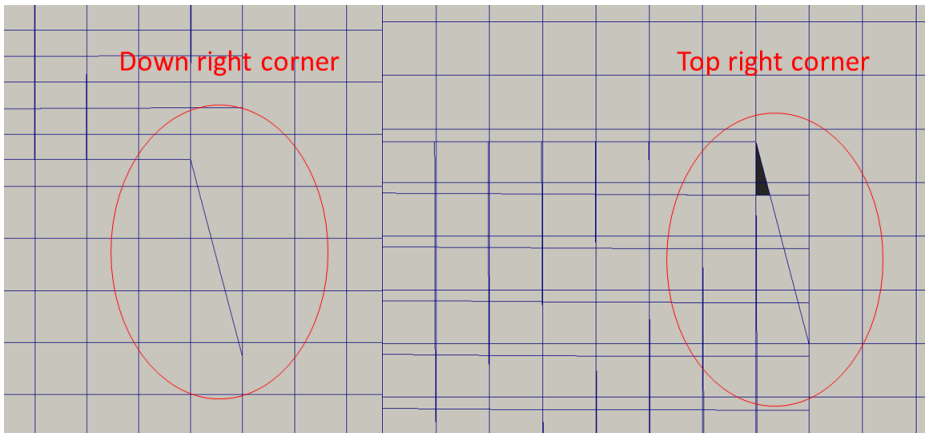

Figure 90: Overset patch sticking to background grid.

A larger background mesh is chosen for the overset grid with snappy. This was needed due to the large overset patch and the large motions. With large motions the overset patch will move closer to the domain boundary and reflection can occur. However, the motions are larger than first expected and a larger boundary should be considered. This was not done in this simulation due to the time limitation as the computational time is larger for the overset grid than with the morphing mesh. This is because for every time step hole, fringe and donor cells have to be identified. This time will increased with the number of cells present in the domain. A small domain and a coarse mesh was therefore used.

The y^+ values are too large for the simulations with $U = 1.8$ m/s and $U = 2.5$ m/s. The maximum y^+ values for these velocities are approximately 700 and 760. This is too high compared to the suggested range by ANSYS FLUENT (30-300). Smaller cells close to the body and a finer grid are necessary for the results to be accurate.

The presented issues with the grid needs to be resolved and a grid convergence study should be preformed before reliable results can be obtained. However, the implementation of the overset grid technique proved to be more challenging than expected and this presents the preliminary results in this study of moving mesh.

Chapter 11

11 Discussion

In this chapter a discussion of the assumptions and approach of this study will be presented.

11.1 2D Simulations

A clear flaw in this study is the use of 2D simulations when considering a 3D flow. The spanwise variations are not captured together with the end effects. The considered flow is turbulent and turbulence itself is a 3D phenomena. Turbulent energy cascade in 3D and 2D are also completely different. In 3D there is a direct cascade i.e. the turbulent scales becomes smaller and are dissipated though the viscosity, most at the Kolmogorov scale. In 2D there is a inverse cascade i.e. energy is transferred from smaller to larger scales. This can affect both the range where the results are expected and the trend for increasing Re.

Although 3D simualtions represents the physics of the problem better, 2D simulations has practical advantages in terms of reduced computational time. Vaz et al. [41] studied 2D and 3D flow around a circular cylinder in $Re = 9.3 \times 10^4$ and $Re = 5.5 \times 10^5$. They highlight the significant increase in computational demand that is needed to move from 2D to 3D simulations. For the $k - \omega$ simulations, the CPU Time for the 3D simulations was more than twice the CPU Time for 2D simulations.

For inexperienced users that in many cases use the trial and error approach, 2D simulations is a good place to start before moving over to 3D simulations. In this case 2D simulations was also chosen due to the physics of the studied phenomena. An increase in correlation length is assumed when VIM occurs and a reduction in spanwise variations allows of a strip theory approach. This assumption introduces an error in this work and 3D simulations should be preformed for further validation of this approach.

11.2 Turbulence Model

A RANS simulations with a $k - \omega$ SST turbulence model was used. RANS simulations was chosen due to the significant difference in computational cost. The free-stream turbulence profile is also easier to prescribe in RANS models. LES and DNS require special steps to prescribe the free stream turbulence, while the RANS models allows straightforward values to be imposed on the free-stream boundary condition. Turbulent intensities are assumed to be isotropic with RANS.
$k - \omega$ was chosen over $k - \epsilon$ as $k - \epsilon$ does not allow direct integration through the boundary layer and it over-produces the turbulence turbulence kinetic energy that may affect the flow patterns.
Most two-equation RANS models assumes isotropic turbulence and 3D simulations of some bluff bodies will inevitably loss the 3D vortical structure in spanwise direction. The 3D simulation will the give same results as 2D. 2D RANS simulations differs from the 2D laminar model as the spanwise momentum diffusion are accounted for and the solution contain 3D effects and is physical [39].

Wall functions are used to treat the physics near the wall. This is done in order to have a coarser grid near the wall and reduce the computational cost. However, the implementation of the wall function seems to affect the drag force as an increasing drag coefficient is observed for an increasing Re. The drag is decreasing with a small slope and the wall functions might not affect the solution significantly, but some simulations with near wall treatment could have been preformed to verify if the problem is caused by the wall functions.

The same values for k and ω have been used for all simulations with inlet velocity. This is wrong as k depends on the inlet velocity and ω depends on k. The k and omega used in the simulations

corresponds to an inlet velocity $U = 1$ m/s. This means that for all simulations with $U \neq 1$ m/s the k and ω values are wrong. This error was discovered too late to rerun all the simulations, but some of the simulations with the fixed spar and semi-submersible was redone to evaluate how much this mistake affects the results.

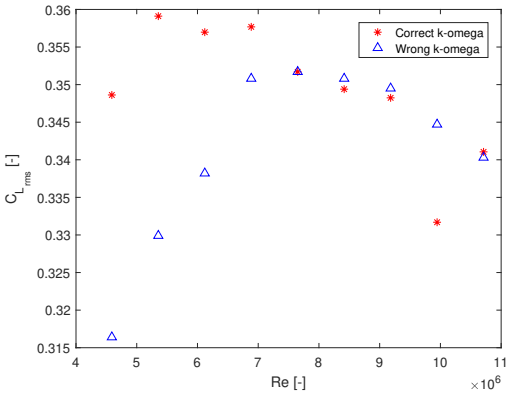

Figure 91: $C_{L_{rms}}$ for fixed spar with wrong and corrected $k - \omega$ values.

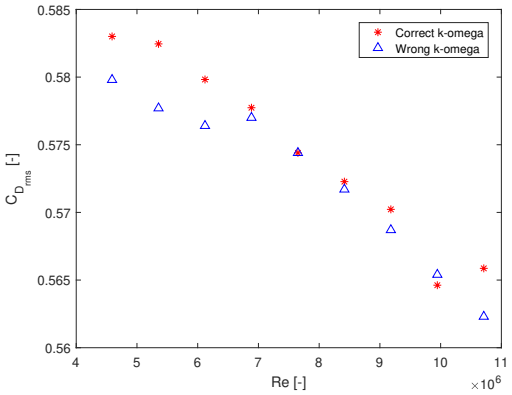

Figure 92: $C_{L_{rms}}$ for fixed spar with wrong and corrected $k - \omega$ values.

Figure 91 and 92 shows a comparison between the presented results and simulations with corrected turbulent boundary conditions. The largest differences are found in the $C_{L_{rms}}$ and indicate that the lift force is more sensitive to the turbulence modelling than the drag force. The largest difference in the lift force is observed for $Re = 4.59 \times 10^6$ and are 12.14%. The largest difference in drag is observed for $Re = 5.36 \times 10^6$ and the difference is 3.29%. The difference for the drag is small, but the differences observed in the lift is more of concern. The difference is decreasing for higher Re and the solution seems more affected when too large values for k and ω is used for lower Re than to small k and ω is used for higher Re. This is understandable as the effect of turbulence is larger for lower Re.

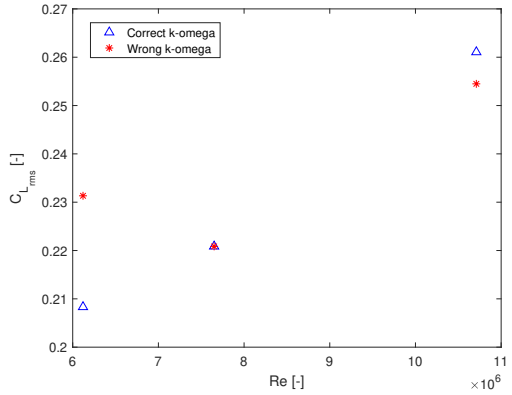

Figure 93: $C_{L_{rms}}$ for fixed semi-submersible with wrong and corrected $k - \omega$ values.

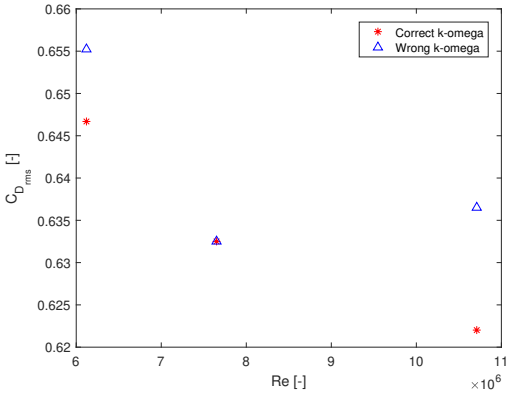

Figure 94: $C_{L_{rms}}$ for fixed semi-submersible with wrong and corrected $k - \omega$ values.

Only two simulations were tested with the right k and ω values for the semi-submersible. This is due to the limited time. The largest difference is still observed in the lift with a difference of 10.47%. The

largest difference in the drag is 2.3%.

11.3 Parallel Computing

The supercomputer Vilje is used for the simulations and the effect of parallel computing of especially the cases with overset grids are yet to be studied in detailed. The advantages of parallel computing is the possibility to divide the domain and distribute it to different processors. This makes the simulations faster, but the accuracy of the solution depends on how good the communication between the processors. For an overset grid it is crucial that the cells are identified correctly at all time step and this might be a challenge if the domain is divided into numerous sub-domains and distributed on different processors.

Chapter 12

12 Conclusion

This thesis has presented some of the numerical issues regarding numerical simulations of flow past a fixed spar and semi-submersible in supercritial Re. The results has been discussed in terms of hydrodynamic quantities. Hydrodynamic interaction between the cylindrical parts of the semi-submersible and Cross-flow VIM occurrence of the spar has also been studied.

The flow regime studied is in the transcritical regime as $Re > 3 \times 10^6$. The lack of good numerical and experimental references in this regime is sever and highlights the need for more research on higher Re. This is especially important for practical hydrodynamic problems where the Re is high. Many of the experiments for high Re is conducted in wind tunnels where the added mass effect is not as important as it is for experiments conducted in water. Research on VIV and VIM in this Re regime for cylinders with larger diameter is also needed as most of the literature are considering pipes. This has made the validation of the results challenging.

Grid generation has been a major part of this work. A structured mesh generated with blockMesh was first used during the project and provided good results during a laminar convergence study at $Re = 100$. However, a turbulent convergence study for transcritical Re, $Re > 10^6$, proved to be a challenge. The multiple blocks and different variables that needs to be manually changed were difficult for an inexperienced user. During the turbulent convergence study with the unstructured mesh it was discovered that the computed maximum Courant number in OpenFOAM does not consider high local velocities and a smaller timestep was needed. An unstructured mesh with snappyHexMesh was chosen as an alternative to the unstructured mesh. This option was chosen as less user interaction is needed and the method is more suitable for multiple cylinders. This grid shows good performance for transcritical flows for a fixed single cylinder representing a spar cross-section, two fixed side-by-side cylinders and three fixed cylinders representing a cross-section of the semi-submersible.

The two side-by-side cylinders experiences a mirrored, anti-phase vortex shedding and the same is observed in the transient state of the vortex shedding of the semi-submersible. A transition from anti-phase to in-phase vortex shedding is observed for the two side-by-side cylinders on the semi-submersible as steady state is reached. $C_{D_{rms}}$, $C_{L_{rms}}$ and St are presented for $3.06 \times 10^6 \leqslant Re \leqslant 1.07 \times 10^7$ for the spar for $3.06 \times 10^6 \leqslant Re \leqslant 1.58 \times 10^7$ for the semi-submersible. The two platforms are compared for the same range or reduced velocity. The $C_{D_{rms}}$, $C_{L_{rms}}$ and St for $U = 1$ m/s for the spar and semis-submersible are summarized in the table below. The semi-submersible experiences a higher drag force than the spar and the third down stream cylinder experiences the highest drag force. The lift force is higher for the spar since the lift force on the two side-by-side cylinders on the semi-submersible are acting in opposite direction and a cancelling effect occurs. The downstream cylinder is therefore also the main contributor to the lift force on the semi-submersible. This may indicate that this is the cylinder that most likely will trigger cross-flow resonance for this structure.

Table 24: Summary of the results for a fixed spar and semis-submersible.

Case	$C_{D_{rms}}$ [-]	$C_{L_{rms}}$ [-]	St [-]
Spar	0.5894	0.3631	0.2940
Semi-submersible	0.6325	0.2209	0.2940

Cross-flow VIM was only studied for the spar platform as time did not allow for a study of the semi-submersible. Two overset grids and one morphing grid was tested. The spar was modelled as a spring-mass system and only allowed to move in cross-flow direction. Decay tests and forced oscillation

tests were preformed to identify the natural period and added mass of the system. The morphing mesh and the overset with an unstructured overset patch preformed well and was chosen for a further study with uniform inlet velocity. Both the morphing mesh and the overset grid was tested with a inlet velocity of $U = 0.4$ m/s which corresponds to a reduce velocity around 3.6 for both cases. Resonance was observe in both cases as the cylinder oscillates with a period close to the natural period, however the amplitude of oscillation is around 0.7D and higher than expected. The lower out-of-lock-in region has been captured and reasonable oscillation amplitudes were obtained. More research is needed on the upper out-of-lock-in region. Two high velocities were tested, but unrealistic high cross-flow amplitudes were observed, due to a large lift force in the transient state. A ramp function and damping was tested and a reduction in the amplitude was observed. However, numerical challenges has been reported on the grid and further adjustments and a grid convergence study should be preformed before the results can be reliable and validated further.

Chapter 13

13 Further work

This section propose further work based on the findings and challenges presented in this thesis.

- Resolve the numerical issues connected with the overset grid and conduct a convergence study for this grid.
- Study the effect of using a ramp function and introducing damping to the system.
- Identify the lower and upper lock-in region for the spar platform. Possibly by using a ramp function with velocities from 0.1 m/s - 1.4 m/s.
- Study the system as a two DoF system and analyse the combination of cross-flow and in-line VIM.
- Make a dynamic grid for the semi-submersible, preform a grid convergence stud and identify the lower and upper lock-in region.

References

[1] Offshoe wind in europe: Key trends and statistics 2018, 2018.

[2] Achenbach, E. Influence of surface roughness on the cross-flow around a circular cylinder. *Journal of fluid mechanics 46*, 2 (1971), 321–335.

[3] Achenbach, E., and Heinecke, E. On vortex shedding from smooth and rough cylinders in the range of reynolds numbers 6×10^3 to 5×10^6. *Journal of fluid mechanics 109* (1981), 239–251.

[4] Alam, M. M., Moriya, M., and Sakamoto, H. Aerodynamic characteristics of two side-by-side circular cylinders and application of wavelet analysis on the switching phenomenon. *Journal of Fluids and Structures 18*, 3-4 (2003), 325–346.

[5] Bak, C., Zahle, F., Bitsche, R., Kim, T., Yde, A., Henriksen, L., Andersen, P. B., Natarajan, A., and Hansen, M. H. Design and performance of a 10 mw wind turbine. *Wind Energy 124* (2013).

[6] Basu, R. I. Aerodynamic forces on structures of circular cross-section. part 1. model-scale data obtained under two-dimensional conditions in low-turbulence streams. *Journal of Wind Engineering and Industrial Aerodynamics 21*, 3 (1985), 273–294.

[7] Bloor, M. S. The transition to turbulence in the wake of a circular cylinder. *Journal of Fluid Mechanics 19*, 2 (1964), 290–304.

[8] capacity highlights, R. Tech. rep., International Renewable Energy Agency, 2019.

[9] Catalano, P., Wang, M., Iaccarino, G., and Moin, P. Numerical simulation of the flow around a circular cylinder at high reynolds numbers. *International Journal of Heat and Fluid Flow 24*, 4 (2003), 463–469.

[10] Cheung, J., and Melbourne, W. Turbulence effects on some aerodynamic parameters of a circular cylinder at supercritical reynolds numbers. *Journal of Wind Engineering and Industrial Aerodynamics 14*, 1-3 (1983), 399–410.

[11] DNV, G. Free spanning pipelines (dnv-rp-f105). *Det Norske Veritas AS, Oslo* (2006).

[12] DNV, G. Design of offshore wind turbine structures (dnv-osj101), 2013.

[13] DNV, G. Enviromental conditions and enviromental loads (dnv-rp-c205). *Det Norske Veritas AS, Oslo* (2014).

[14] Faltinsen, O. M. *Sea loads on ships and offshore structures*, vol. 1. Cambridge university press, 1993.

[15] Gomez P., Sanches G., L. A. G. G. Qualification of innovative floating substructures for 10mw wind turbines and water depths greater than 50m, 2015.

[16] Hirabayashi, S. Numerical analysis of vortex-induced motion of two-dimensional circular cylinder by lattice boltzmann method. *Journal of Marine Science and Technology 21*, 3 (2016), 426–433.

[17] HSE. Environmental considerations. offshore technology report. Tech. rep., Health and Safety Executive, 2002.

[18] Johannessen, M. Concept study and design of floating offshore wind turbine support structure, 2017.

[19] Jones, G. W., Walker, R. W., and Cincotta, J. Aerodynamic forces on a stationary and oscillating circular cylinder at high reynolds numbers, 1969.

[20] Journée, J. M., and Massie, W. *Offshore hydromechanics*. TU Delft, 2000.

[21] Jung, M. S., and Kwon, O. J. A parallel unstructured overset mesh technique for unsteady flow simulations. In *Computational Fluid Dynamics 2006*. Springer, 2009, pp. 317–322.

[22] Kawamura, T., Nakao, T., Hayashi, M., and Murayama, K. Strouhal number effect on synchronized vibration range of a circular cylinder in cross flow. *JSME International Journal Series B Fluids and Thermal Engineering 44*, 4 (2001), 729–737.

[23] Lam, K., and Cheung, W. Phenomena of vortex shedding and flow interference of three cylinders in different equilateral arrangements. *Journal of fluid mechanics 196* (1988), 1–26.

[24] Menter, F. R. Improved two-equation k-εturbulence models for aerodynamic flows. *NASA Technical Memorandum 103975* (1992).

[25] Novak, M., and Tanaka, H. Pressure correlations on a vibrating cylinder. *Proceedings of the 4th International Conference on Wind Effects on Buildings and Structures* (01 1975), 227–232.

[26] Ong, M. C., Utnes, T., Holmedal, L. E., Myrhaug, D., and Pettersen, B. Numerical simulation of flow around a smooth circular cylinder at very high reynolds numbers. *Marine Structures 22*, 2 (2009), 142–153.

[27] Park, J., Kwon, K., and Choi, H. Numerical solutions of flow past a circular cylinder at reynolds numbers up to 160. *KSME international Journal 12*, 6 (1998), 1200–1205.

[28] R, J., and C, R. M. Floating offshore wind: Market and technology review, 2015.

[29] Rajani, B., Kandasamy, A., and Majumdar, S. Numerical simulation of laminar flow past a circular cylinder. *Applied Mathematical Modelling 33*, 3 (2009), 1228–1247.

[30] Robertson, A., Jonkman, J., Masciola, M., Song, H., Goupee, A., Coulling, A., and Luan, C. Definition of the semisubmersible floating system for phase ii of oc4. Tech. rep., National Renewable Energy Lab.(NREL), Golden, CO (United States), 2014.

[31] Rodrigo, J. State-of-the-art of wind resource assessment. *Waudit Deliv D 7* (2010).

[32] Rosetti, G. F., Vaz, G., and Fujarra, A. L. Urans calculations for smooth circular cylinder flow in a wide range of reynolds numbers: solution verification and validation. *Journal of Fluids Engineering 134*, 12 (2012), 121103.

[33] Roshko, A. Experiments on the flow past a circular cylinder at very high reynolds number. *Journal of Fluid Mechanics 10*, 3 (1961), 345–356.

[34] Schewe, G. On the force fluctuations acting on a circular cylinder in crossflow from subcritical up to transcritical reynolds numbers. *Journal of fluid mechanics 133* (1983), 265–285.

[35] Shih, W., Wang, C., Coles, D., and Roshko, A. Experiments on flow past rough circular cylinders at large reynolds numbers. *Journal of Wind Engineering and Industrial Aerodynamics 49*, 1-3 (1993), 351–368.

[36] Singh, S., and Mittal, S. Flow past a cylinder: shear layer instability and drag crisis. *International journal for numerical methods in fluids 47*, 1 (2005), 75–98.

[37] Squires, K. D., Krishnan, V., and Forsythe, J. R. Prediction of the flow over a circular cylinder at high reynolds number using detached-eddy simulation. *Journal of Wind Engineering and Industrial Aerodynamics 96*, 10-11 (2008), 1528–1536.

[38] Sumner, D., Wong, S., Price, S., and Paidoussis, M. Fluid behaviour of side-by-side circular cylinders in steady cross-flow. *Journal of Fluids and Structures 13*, 3 (1999), 309–338.

[39] Sun, D., Owen, J., and Wright, N. Application of the k–ω turbulence model for a wind-induced vibration study of 2d bluff bodies. *Journal of Wind Engineering and Industrial Aerodynamics 97*, 2 (2009), 77–87.

[40] Tang, Y., Li, Y., Liu, L., Jin, W., and Qu, X. Study on influence of vortex induced loads on the motion of spar-type wind turbine based on aero-hydro-vortex-mooring coupled model. In *ASME 2017 36th International Conference on Ocean, Offshore and Arctic Engineering* (2017), American Society of Mechanical Engineers, pp. V010T09A058–V010T09A058.

[41] Vaz, G., Mabilat, C., van der Wal, R., and Gallagher, P. Viscous flow computations on a smooth cylinders: a detailed numerical study with validation. In *ASME 2007 26th International Conference on Offshore Mechanics and Arctic Engineering* (2007), American Society of Mechanical Engineers, pp. 849–860.

[42] Williamson, C. Evolution of a single wake behind a pair of bluff bodies. *Journal of Fluid Mechanics 159* (1985), 1–18.

[43] Williamson, C. Oblique and parallel modes of vortex shedding in the wake of a circular cylinder at low reynolds numbers. *Journal of Fluid Mechanics 206* (1989), 579–627.

[44] Zdravkovich, M. Flow induced oscillations of two interfering circular cylinders. *Journal of Sound and Vibration 101*, 4 (1985), 511–521.

[45] Zdravkovich, M. The effects of interference between circular cylinders in cross flow. *Journal of fluids and structures 1*, 2 (1987), 239–261.

[46] Zdravkovich, M. *Flow around Circular Cylinders: Volume 2: Applications*, vol. 2. Oxford university press, 1997.

Appendix I

The mass, added mass and stiffness matrices for the spar system is given in this Appendix.

```
M =

   1.0e+11 *

    0.0002         0         0         0   -0.0107         0
         0    0.0002         0    0.0107         0         0
         0         0    0.0002         0         0         0
         0    0.0107         0    1.1570         0         0
   -0.0107         0         0         0    1.1570         0
         0         0         0         0         0    0.0040
```

Figure 95: Mass matrix for spar

```
A =

   1.0e+10 *

    0.0016         0         0         0   -0.0865         0
         0    0.0016         0    0.0865         0         0
         0         0    0.0016         0         0         0
         0    0.0865         0    6.0844         0         0
   -0.0865         0         0         0    6.0844         0
         0         0         0         0         0         0
```

Figure 96: Added mass matrix for spar

```
C =

   1.0e+09 *

    0.0001         0         0         0   -0.0052         0
         0    0.0001         0    0.0052         0         0
         0         0    0.0000         0         0         0
         0    0.0052         0    2.5954         0         0
   -0.0052         0         0         0    2.5954         0
         0         0         0         0         0    0.1480
```

Figure 97: Stiffness matrix for spar

Appendix II

This Appendix shows the two unstructured grids with SnappyHexMesh for a fixed cylinder.

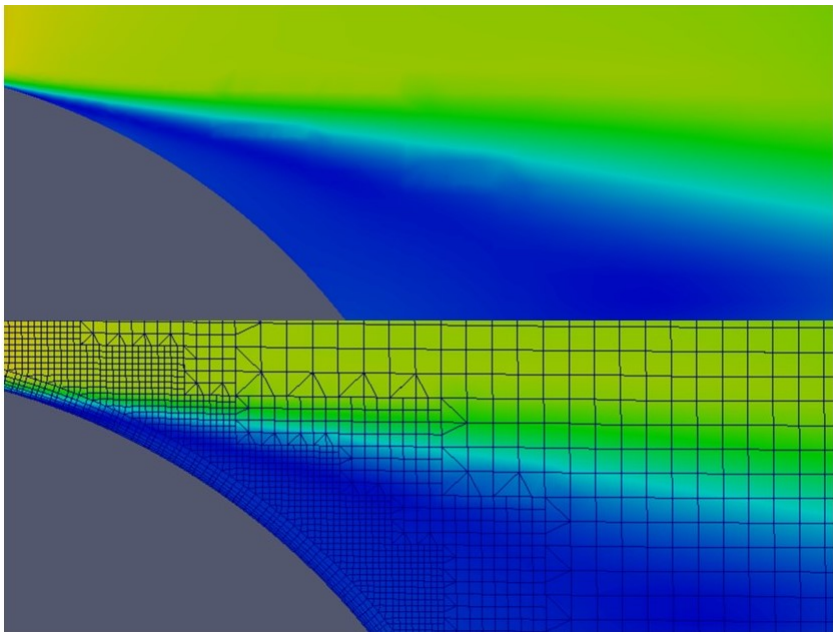

Figure 98: Flow resolution close to the cylinder - grid No. 1.

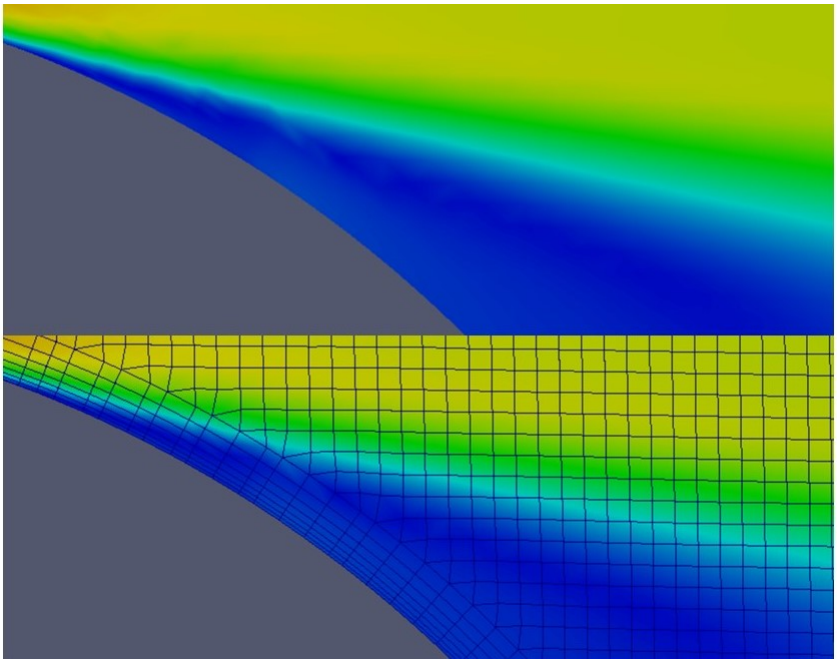

Figure 99: Flow resolution close to the cylinder - grid No. 2.

Appendix III

This Appendix shows flow regime classifications for side-by-side and tandem cylinders.

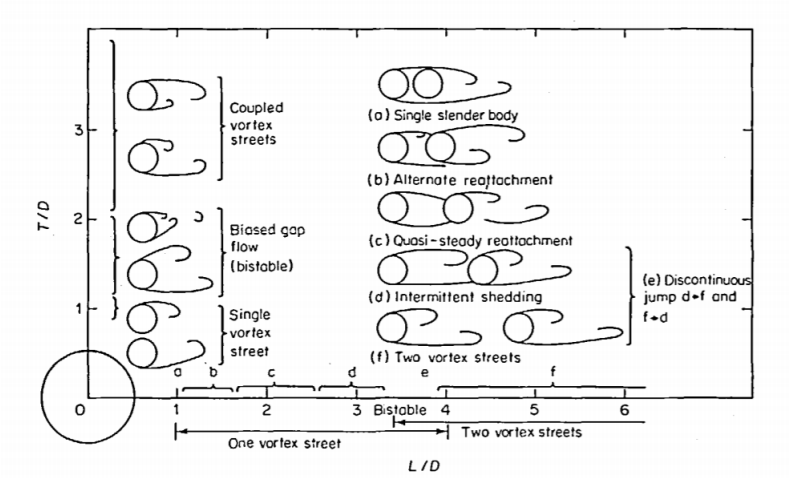

Figure 100: Classification of flow regimes in side-by-side and tandem arrangements for stationary cylinders [44].

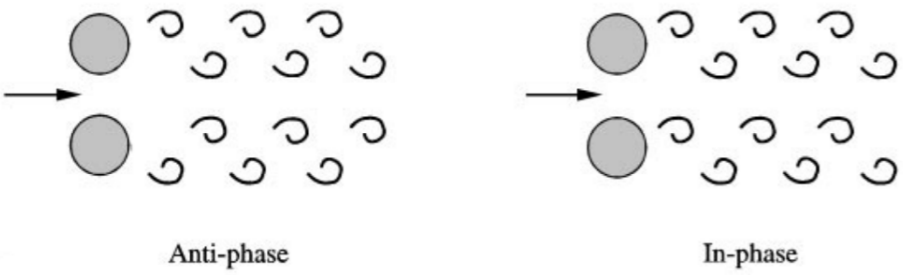

Figure 101: Anti-phase and in-phase vortex street synchronization [38].

Appendix IV

This Appendix shows the lift and drag coefficient for the three individual cylinders in the semi-submersible and the lift and drag coefficient for the total system (the three cylinders combined).

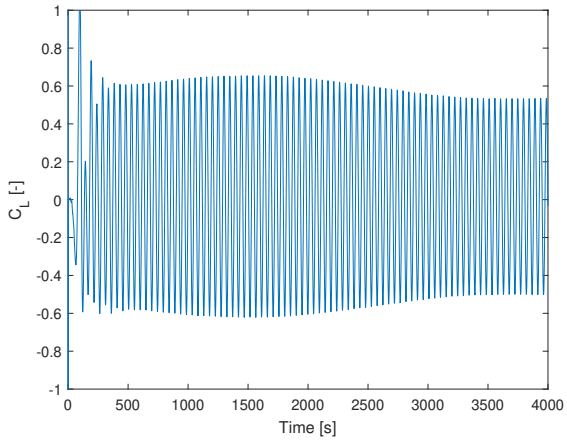

Figure 102: C_L for fixed semi-submersible: Cylinder 1.

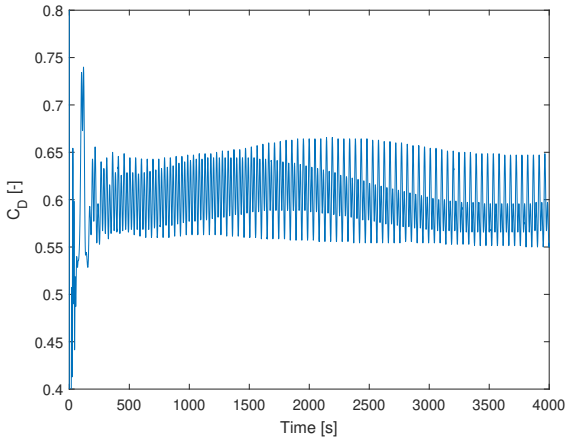

Figure 103: C_D for fixed semi-submersible: Cylinder 1.

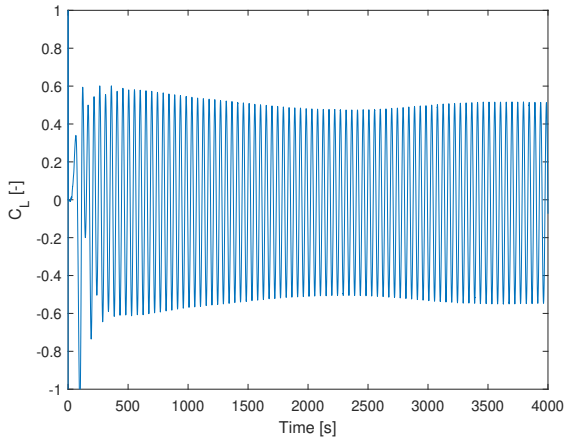

Figure 104: C_L for fixed semi-submersible: Cylinder 2.

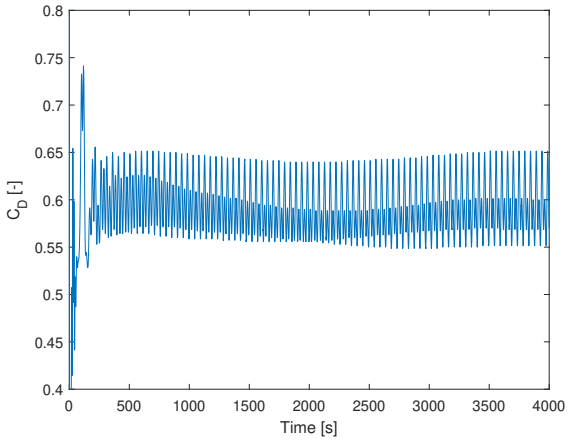

Figure 105: C_D for fixed semi-submersible: Cylinder 2.

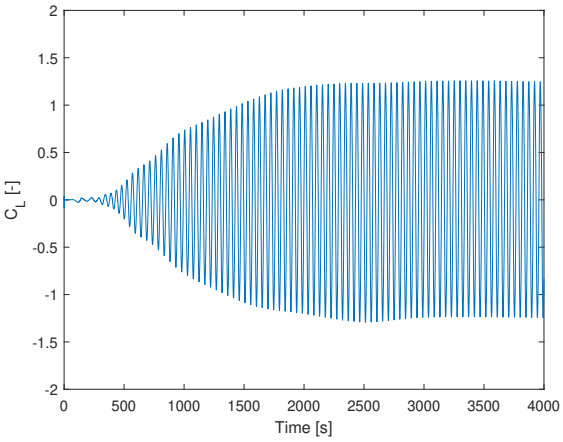

Figure 106: C_L for fixed semi-submersible: Cylinder 3.

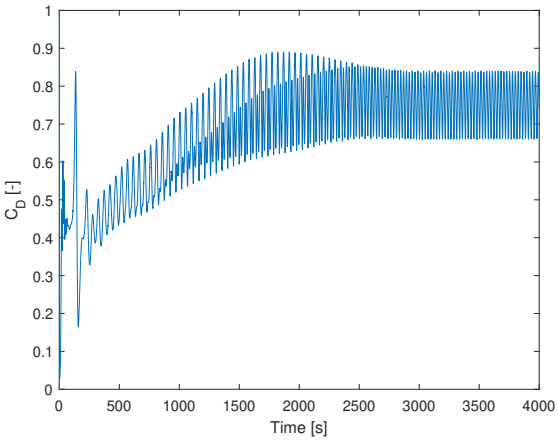

Figure 107: C_L for fixed semi-submersible: Cylinder 3.

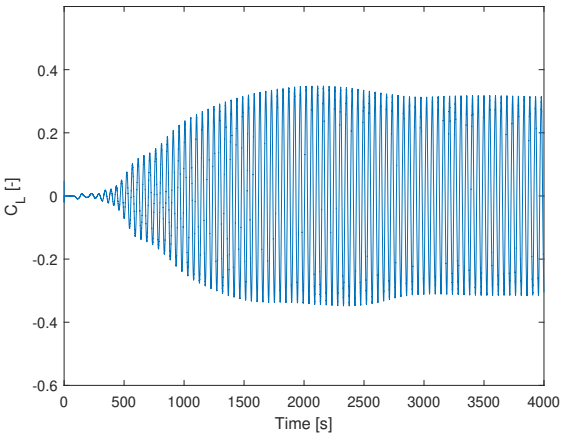

Figure 108: C_L for fixed semi-submersible.

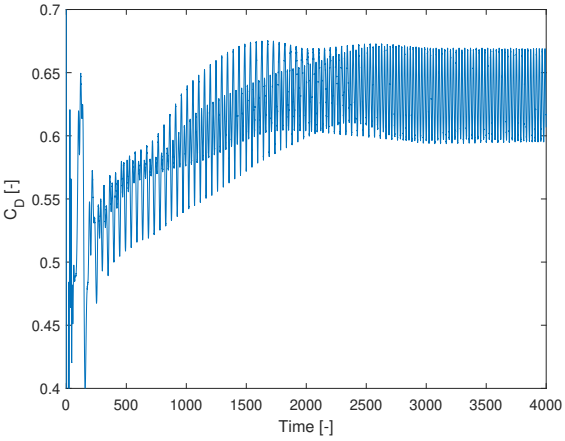

Figure 109: C_D for fixed semi-submersible.

Appendix V

This Appendix shows the results from the decay test and forced oscillation test with the simple overset grid.

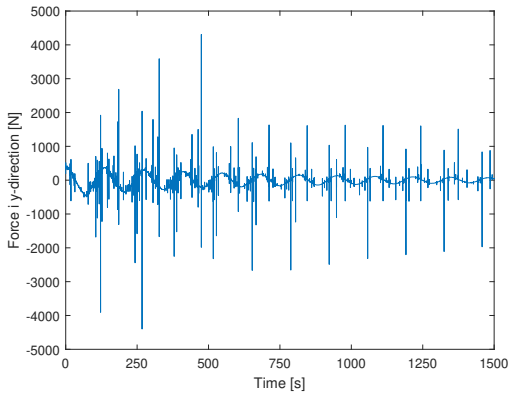

Figure 110: Unfiltered lift force-simple overset decay test.

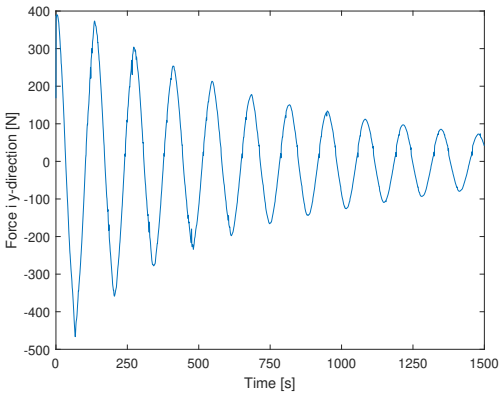

Figure 111: Filtered lift force-simple overset decay test.

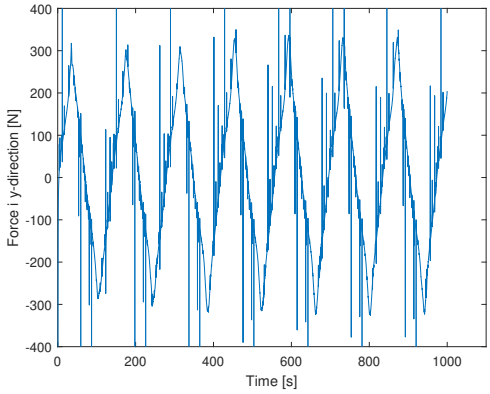

Figure 112: Unfiltered lift force-simple overset forced oscillation test.

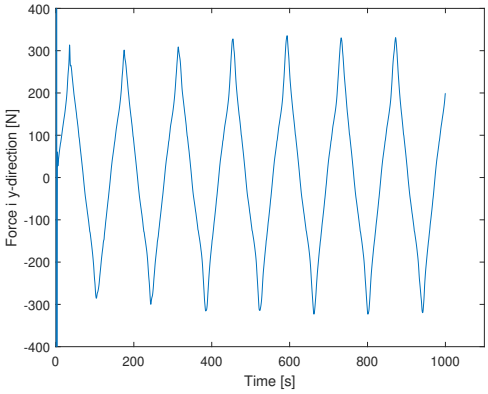

Figure 113: Filtered lift force-simple overset forced oscillation test.

Appendix VI

This Appendix shows the lift force on the cylinder during the decay test with the morphing mesh.

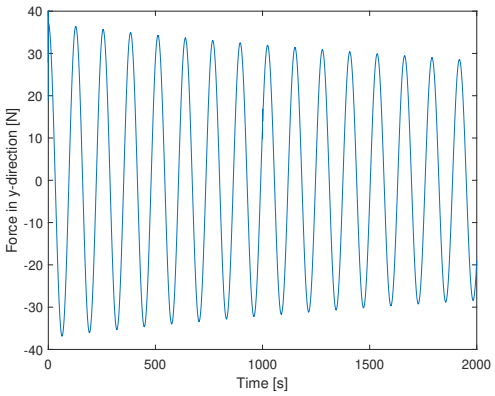

Figure 114: Lift force on cylinder in decay test with a morphing mesh.

Appendix VII

This Appendix shows the results from the decay test and forced oscillation test with the overset grid with snappy.

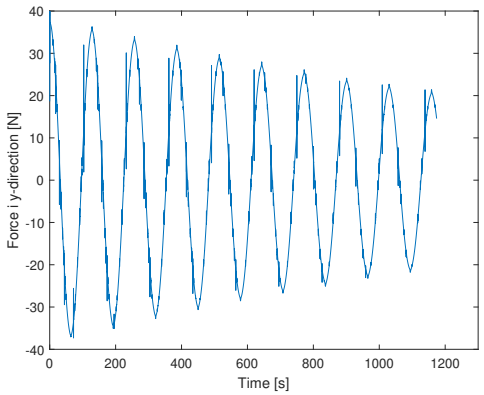

Figure 115: Filtered lift force-overset with snappy decay test.

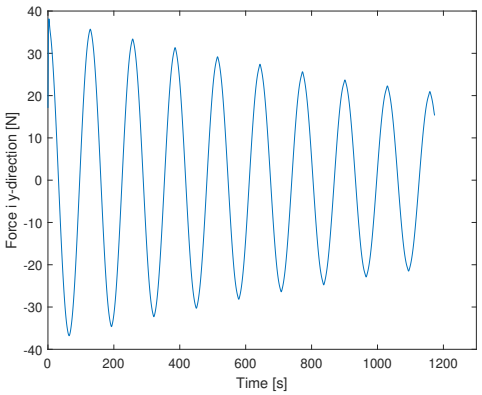

Figure 116: Filtered lift force-overset with snappy decay test.

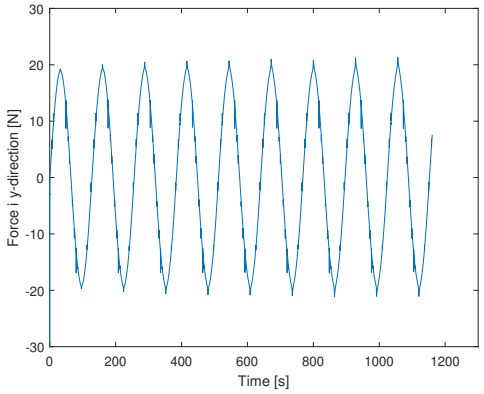

Figure 117: Unfiltered lift force-overset with snappy forced oscillation test.

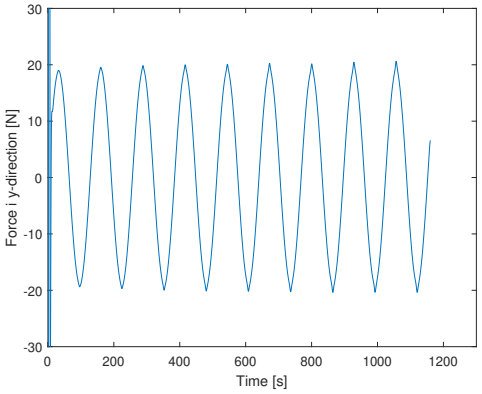

Figure 118: Filtered lift force-overset with snappy forced oscillation test.

Appendix VIII

This Appendix shows some of the results for $U = 1.8$ m/s. The initial results are first given before the results with a ramp function is presented. The results for a ramp function and damping is also given. The results are given in terms of plots of the dimensionless cross-flow amplitude, lift and drag force and PSD plots of the lift force.

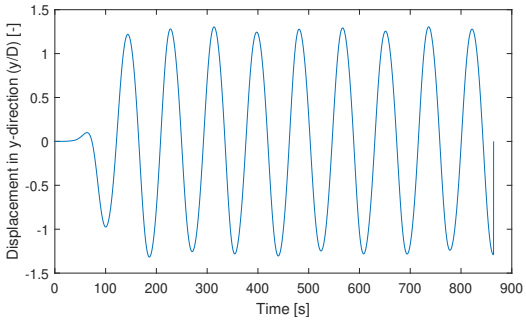

Figure 119: Cross-flow amplitude over time $U = 1.8$ m/s.

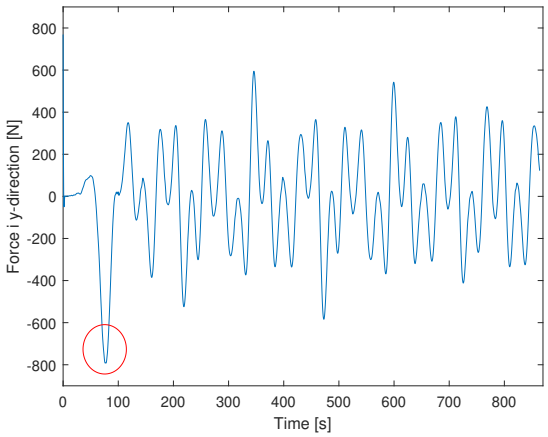

Figure 120: Cross-flow amplitude over time $U = 1.8$ m/s.

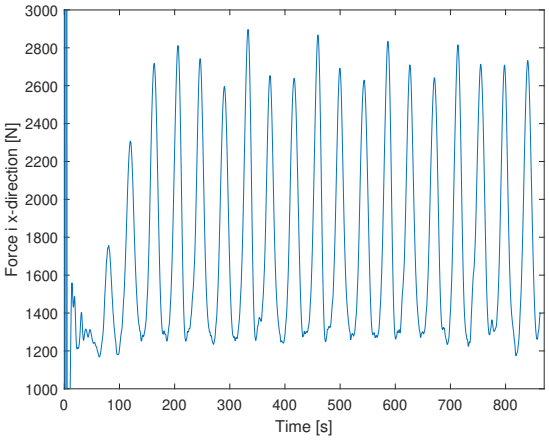

Figure 121: Cross-flow amplitude over time $U = 1.8$ m/s.

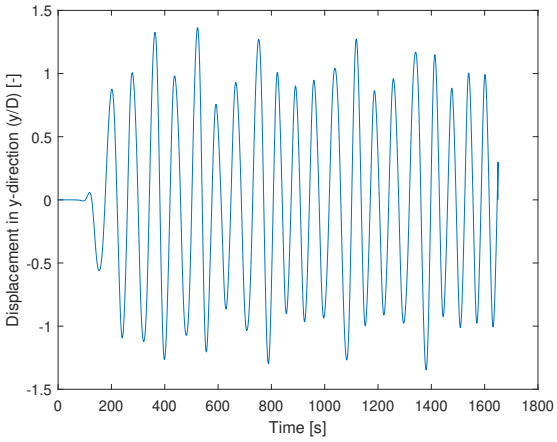

Figure 122: Cross-flow amplitude over time $U = 1.8$ m/s - ramp.

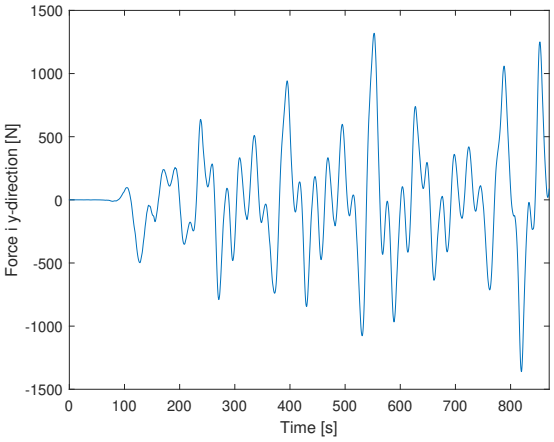

Figure 123: Lift force over time $U = 1.8$ m/s - ramp.

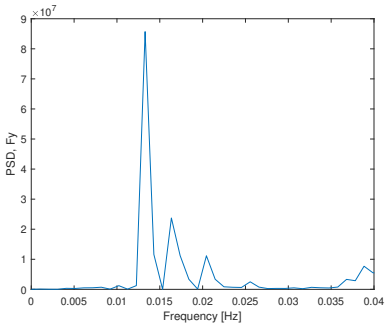

Figure 124: PSD of lift force $U = 1.8$ m/s - ramp.

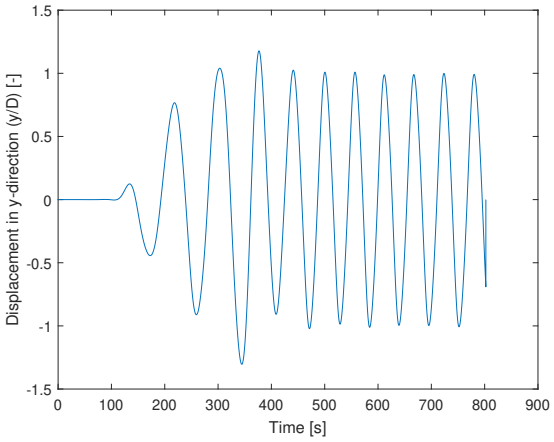

Figure 125: Cross-flow amplitude over time $U = 1.8$ m/s - ramp+damping.

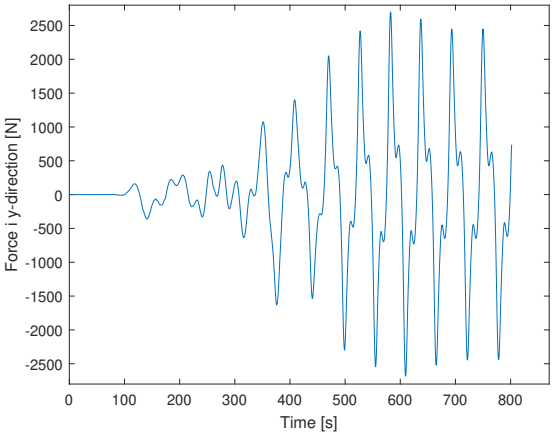

Figure 126: Cross-flow amplitude over time $U = 1.8$ m/s - ramp+damping.

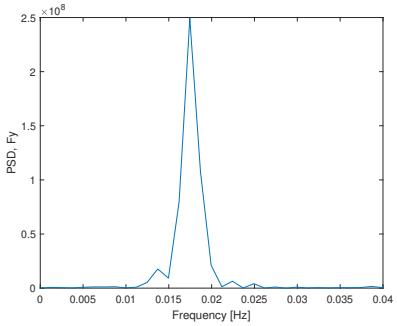

Figure 127: PSD of lift force $U = 1.8$ m/s - ramp+damping.

Appendix IX

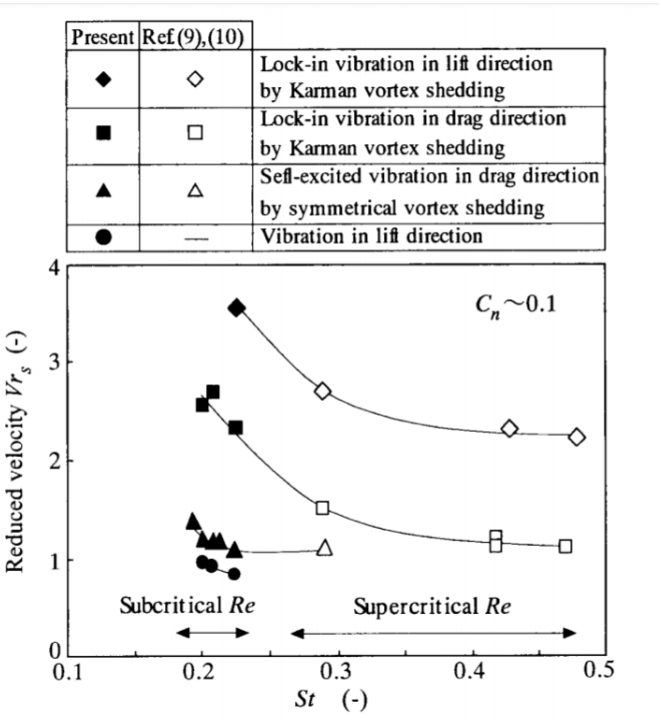

Figure 128: Reduced velocity at beginning of synchronization [22].

Appendix X

Run script

```
#!/bin/bash -l
#PBS -N overSapU02
#PBS -S /bin/bash
#PBS -A nn9592k
#PBS -l select=2:ncpus=32:mpiprocs=16
#PBS -l walltime=90:00:00

source /usr/share/modules/init/bash

cd $PBS_O_WORKDIR

module load m4/1.4.16
module load gcc/6.2.0 mpt/2.14
module load openfoam/v1806

cd cylinder
blockMesh >blockMesh.log
surfaceFeatureExtract >surfaceFeatureExtract.log
snappyHexMesh -overwrite >snappyHexMesh.log
extrudeMesh >extrudeMesh.log
cd ..

cd all
blockMesh >blockMesh.log
mergeMeshes . ../cylinder -overwrite >mergeMeshes.log

cp -r 0_org 0

checkMesh >checkMesh.log
setFields >setFields.log
topoSet -dict system/topoSetDict_movingZone >topoSet.log
changeDictionary -noFunctionObjects >changeDictionary.log
renumberMesh -overwrite >renumberMesh.log

decomposePar >decomposePar.log
mpiexec_mpt -np 32 overPimpleDyMFoam -parallel >output.log
reconstructPar >reconstructPar.log
```

controlDict

```
/*--------------------------------*- C++ -*----------------------------------*\
| =========                      |                                            |
|
| \\      /  F ield              | OpenFOAM: The Open Source CFD Toolbox
|
|  \\    /   O peration          | Version:  plus
|
|   \\  /    A nd                | Web:      www.OpenFOAM.com
|
|    \\/     M anipulation       |
|
\*---------------------------------------------------------------------------*/
FoamFile
{
    version     2.0;
    format      ascii;
    class       dictionary;
    location    "system";
    object      controlDict;
}
// * * * * * * * * * * * * * * * * * * * * * * * * * * * * * * * * * * * * * //


libs            ("liboverset.so");

application     overPimpleDyMFoam;

startFrom       startTime;

startTime       0;

stopAt          endTime;

endTime         9000;

deltaT          0.03;

writeControl    timeStep;

writeInterval   10000;

purgeWrite      0;

writeFormat     ascii;

writePrecision  8;

writeCompression off;

timeFormat      general;
```

```
timePrecision   6;

runTimeModifiable false;

adjustTimeStep  no;

// ************************************************************************* //

functions
{
    forceCoeffs
    {
        type                    forceCoeffs;
        functionObjectLibs      ("libforces.so");
        writeControl            timeStep;
        writeInterval           10000;
        patches                 ( cylinder );
        pName                   p;
        UName                   U;
        rho                     rhoInf;
        rhoInf                  1000;
        magUInf                 0.2;
        log                     true;
        liftDir                 (0 1 0);
        dragDir                 (1 0 0);
        CofR                    (0 0 0);
        pitchAxis               (0 0 1);
        lRef                    14;
        Aref                    1.4;
    }
        forces
        {
                type                                    forces;
                functionObjectLibs              ("libforces.so");
                patches                                 (cylinder);
                pName                                   p;
                UName                                   U;
                rho                                     rhoInf;
                rhoInf                                  1000;
                CofR                                    (0 0 0);
        writeControl            timeStep;
        writeInterval           10000;
        }
        shearStress
        {
                type                                    wallShearStress;
                functionObjectLibs              ("libfieldFunctionObjects.so");
                patches                                 (cylinder);
        writeControl            timeStep;
        writeInterval           10000;
        }
```

```
    yPlus1
    {
        type                yPlus;
        functionObjectLibs  ("libfieldFunctionObjects.so");
    patches                 ( cylinder );
        writeControl        timeStep;
        writeInterval       10000;
    }
}
```

snappyHexMeshDict

```
/*--------------------------------*- C++ -*----------------------------------*\
| =========                      |                                            |
|                                |                                            |
| \\      /  F ield              | OpenFOAM: The Open Source CFD Toolbox      |
|                                |                                            |
|  \\    /   O peration          | Version:  2.4.0                            |
|                                |                                            |
|   \\  /    A nd                | Web:      www.OpenFOAM.org                 |
|                                |                                            |
|    \\/     M anipulation       |                                            |
|                                |                                            |
\*---------------------------------------------------------------------------*/
FoamFile
{
    version     2.0;
    format      ascii;
    class       dictionary;
    object      snappyHexMeshDict;
}

// * * * * * * * * * * * * * * * * * * * * * * * * * * * * * * * * * * * * * * * //

// Which of the steps to run
castellatedMesh true;
snap            true;
addLayers       true;


// Geometry. Definition of all surfaces. All surfaces are of class
// searchableSurface.
// Surfaces are used
// - to specify refinement for any mesh cell intersecting it
// - to specify refinement for any mesh cell inside/outside/near
// - to 'snap' the mesh boundary to the surface
geometry
{
    cylinder.stl
    {
        type triSurfaceMesh;
        name cylinder;
    }

    //- Refine a bit extra around the small centre hole
     refinementBox
    {
        type    searchableCylinder;
        point1 (0 0 -0.5);
        point2 (0 0 0.5);
        radius 14;
    }
```

```
    refinementBox1
    {
        type    searchableCylinder;
        point1 (0 0 -0.5);
        point2 (0 0 0.5);
        radius 21;
    }

};



// Settings for the castellatedMesh generation.
castellatedMeshControls
{

    // Refinement parameters
    // ~~~~~~~~~~~~~~~~~~~~~

    // If local number of cells is >= maxLocalCells on any processor
    // switches from from refinement followed by balancing
    // (current method) to (weighted) balancing before refinement.
    maxLocalCells 1000000;

    // Overall cell limit (approximately). Refinement will stop immediately
    // upon reaching this number so a refinement level might not complete.
    // Note that this is the number of cells before removing the part which
    // is not 'visible' from the keepPoint. The final number of cells might
    // actually be a lot less.
    maxGlobalCells 2000000;

    // The surface refinement loop might spend lots of iterations refining just a
    // few cells. This setting will cause refinement to stop if <= minimumRefine
    // are selected for refinement. Note: it will at least do one iteration
    // (unless the number of cells to refine is 0)
    minRefinementCells 0;

    // Number of buffer layers between different levels.
    // 1 means normal 2:1 refinement restriction, larger means slower
    // refinement.
    nCellsBetweenLevels 6;



    // Explicit feature edge refinement
    // ~~~~~~~~~~~~~~~~~~~~~~~~~~~~~~~~

    features
    (
        { file "cylinder.eMesh"; level 1; }
    );
```

```
    // Surface based refinement
    // ~~~~~~~~~~~~~~~~~~~~~~~~

    // Specifies two levels for every surface. The first is the minimum level,
    // every cell intersecting a surface gets refined up to the minimum level.
    // The second level is the maximum level. Cells that 'see' multiple
    // intersections where the intersections make an
    // angle > resolveFeatureAngle get refined up to the maximum level.

    refinementSurfaces
    {
        cylinder
        {
            // Surface-wise min and max refinement level
            level (2 2);
patchInfo { type wall; }
        }
    }

    resolveFeatureAngle 30;


    // Region-wise refinement
    // ~~~~~~~~~~~~~~~~~~~~~~

    // Specifies refinement level for cells in relation to a surface. One of
    // three modes
    // - distance. 'levels' specifies per distance to the surface the
    //   wanted refinement level. The distances need to be specified in
    //   descending order.
    // - inside. 'levels' is only one entry and only the level is used. All
    //   cells inside the surface get refined up to the level. The surface
    //   needs to be closed for this to be possible.
    // - outside. Same but cells outside.

    refinementRegions
    {
        refinementBox
        {
            mode inside;
            levels ((100 3));
        }
        refinementBox1
        {
            mode inside;
            levels ((10 2));
        }
    }
```

```
    // Mesh selection
    // ~~~~~~~~~~~~~~

    // After refinement patches get added for all refinementSurfaces and
    // all cells intersecting the surfaces get put into these patches. The
    // section reachable from the locationInMesh is kept.
    // NOTE: This point should never be on a face, always inside a cell, even
    // after refinement.
    // This is an outside point locationInMesh (-0.033 -0.033 0.0033);
    locationInMesh (-35 -35 -0.5); // Inside point

    // Whether any faceZones (as specified in the refinementSurfaces)
    // are only on the boundary of corresponding cellZones or also allow
    // free-standing zone faces. Not used if there are no faceZones.
    allowFreeStandingZoneFaces true;
}



// Settings for the snapping.
snapControls
{
    //- Number of patch smoothing iterations before finding correspondence
    //  to surface
    nSmoothPatch 3;
    //nSmoothPatch 5;

    //- Relative distance for points to be attracted by surface feature point
    //  or edge. True distance is this factor times local
    //  maximum edge length.
    tolerance 1.0;

    //- Number of mesh displacement relaxation iterations.
    nSolveIter 300;

    //- Maximum number of snapping relaxation iterations. Should stop
    //  before upon reaching a correct mesh.
    nRelaxIter 5;
    //nRelaxIter 10;

    // Feature snapping

        //- Number of feature edge snapping iterations.
        //  Leave out altogether to disable.
        nFeatureSnapIter 10;

        //- Detect (geometric) features by sampling the surface
        implicitFeatureSnap false;

        //- Use castellatedMeshControls::features
        explicitFeatureSnap true;
```

```
        //- Detect features between multiple surfaces
        //  (only for explicitFeatureSnap, default = false)
        multiRegionFeatureSnap true;
}



// Settings for the layer addition.
addLayersControls
{
    // Are the thickness parameters below relative to the undistorted
    // size of the refined cell outside layer (true) or absolute sizes (false).
    relativeSizes false;

    // Per final patch (so not geometry!) the layer information
    layers
    {
        cylinder
        {
            nSurfaceLayers 7;
        }
    }

    // Expansion factor for layer mesh
    // expansionRatio 1.2;
        expansionRatio 1.3;


    // Wanted thickness of final added cell layer. If multiple layers
    // is the thickness of the layer furthest away from the wall.
    // Relative to undistorted size of cell outside layer.
    // See relativeSizes parameter.
    //finalLayerThickness 0.8;
          firstLayerThickness 0.017;

    // Minimum thickness of cell layer. If for any reason layer
    // cannot be above minThickness do not add layer.
    // See relativeSizes parameter.
    minThickness 0.01;

    // If points get not extruded do nGrow layers of connected faces that are
    // also not grown. This helps convergence of the layer addition process
    // close to features.
    nGrow 0;


    // Advanced settings

    // When not to extrude surface. 0 is flat surface, 90 is when two faces
    // are perpendicular
    featureAngle 30;
```

```
    // Maximum number of snapping relaxation iterations. Should stop
    // before upon reaching a correct mesh.
    nRelaxIter 5;

    // Number of smoothing iterations of surface normals
    nSmoothSurfaceNormals 1;

    // Number of smoothing iterations of interior mesh movement direction
    nSmoothNormals 3;

    // Smooth layer thickness over surface patches
    nSmoothThickness 10;

    // Stop layer growth on highly warped cells
    maxFaceThicknessRatio 0.5;

    // Reduce layer growth where ratio thickness to medial
    // distance is large
    maxThicknessToMedialRatio 0.3;

    // Angle used to pick up medial axis points
    minMedianAxisAngle 90;

    // Create buffer region for new layer terminations
    nBufferCellsNoExtrude 0;


    // Overall max number of layer addition iterations. The mesher will exit
    // if it reaches this number of iterations; possibly with an illegal
    // mesh.
    nLayerIter 50;

    // Max number of iterations after which relaxed meshQuality controls
    // get used. Up to nRelaxIter it uses the settings in meshQualityControls,
    // after nRelaxIter it uses the values in meshQualityControls::relaxed.
    nRelaxedIter 20;
}



// Generic mesh quality settings. At any undoable phase these determine
// where to undo.
meshQualityControls
{
    #include "meshQualityDict"

    // Optional : some meshing phases allow usage of relaxed rules.
    // See e.g. addLayersControls::nRelaxedIter.
    relaxed
    {
        //- Maximum non-orthogonality allowed. Set to 180 to disable.
        maxNonOrtho 75;
```

```
    }

    // Advanced

    //- Number of error distribution iterations
    nSmoothScale 4;
    //- amount to scale back displacement at error points
    errorReduction 0.75;
}


// Advanced

// Write flags
writeFlags
(
    scalarLevels    // write volScalarField with cellLevel for postprocessing
    layerSets       // write cellSets, faceSets of faces in layer
    layerFields     // write volScalarField for layer coverage
);


// Merge tolerance. Is fraction of overall bounding box of initial mesh.
// Note: the write tolerance needs to be higher than this.
mergeTolerance 1E-5;


// ************************************************************************* //
```

dynamicMeshDict-Free motion

```
/*--------------------------------* C++ -*----------------------------------*\
| =========                 |                                                 |
|
| \\      /  F ield         | OpenFOAM: The Open Source CFD Toolbox
|
|  \\    /   O peration     | Version:  v1806
|
|   \\  /    A nd           | Web:      www.OpenFOAM.com
|
|    \\/     M anipulation  |
|
\*---------------------------------------------------------------------------*/
FoamFile
{
    version     2.0;
    format      ascii;
    class       dictionary;
    object      dynamicMeshDict;
}
// * * * * * * * * * * * * * * * * * * * * * * * * * * * * * * * * * * * * //


dynamicFvMesh       dynamicOversetFvMesh;

motionSolverLibs    ("libsixDoFRigidBodyMotion.so");

motionSolver    sixDoFRigidBodyMotion;


//sixDoFRigidBodyMotionCoeffs


patches         (cylinder);
innerDistance   42.0;
outerDistance   43.0;

centreOfMass   (0 0 0);
mass            15393.8; //146190; //295885.7; 1.541e07;
momentOfInertia (1.102e9 1.102e9 3.81e6);

//angularMomentum (0 0 -2);
g               (0 0 0);
rho             rhoInf;
rhoInf          1000;
report          on;
reportToFile    on;


        solver
    {
```

```
        type Newmark;
    }

    constraints
    {

//only let cylinder move in y-direction
        fixedLine
        {
            sixDoFRigidBodyMotionConstraint line;
            //centreOfRotation (0.5 0.45 0.1);
            direction (0 1 0);
        }

//eliminates any rotational motion
                noRotation
                {
                        sixDoFRigidBodyMotionConstraint orientation;
                        centreOfRotation        (0 0 0);
                }

    }

        restraints
{
    S1
    {
        sixDoFRigidBodyMotionRestraint linearSpring;

        anchor          (0 70 0); //Top Spring
        refAttachmentPt (0 7 0);
        stiffness       37.176;
        damping         0;
        restLength      63;
    }

    S2
    {
        sixDoFRigidBodyMotionRestraint linearSpring;

        anchor          (0 -70 0); //Bottom spring
        refAttachmentPt (0 -7 0);
        stiffness       37.176;
        damping         0;
        restLength      63;
    }
}

// ************************************************************************* //
```

dynamicMeshDict-Forced Motion

```
/*--------------------------------*- C++ -*----------------------------------*\
| =========                      |                                            |
|                                |                                            |
| \\      /  F ield              | OpenFOAM: The Open Source CFD Toolbox      |
|                                |                                            |
|  \\    /   O peration          | Version:  v1806                            |
|                                |                                            |
|   \\  /    A nd                | Web:      www.OpenFOAM.com                 |
|                                |                                            |
|    \\/     M anipulation       |                                            |
|                                |                                            |
\*---------------------------------------------------------------------------*/
FoamFile
{
    version     2.0;
    format      ascii;
    class       dictionary;
    object      dynamicMeshDict;
}
// * * * * * * * * * * * * * * * * * * * * * * * * * * * * * * * * * * * * * //


dynamicFvMesh       dynamicOversetFvMesh;

dynamicOversetFvMeshCoeffs
{

}

solver          multiSolidBodyMotionSolver;

multiSolidBodyMotionSolverCoeffs
{
    cylinderZone
   {
        solidBodyMotionFunction oscillatingLinearMotion;

amplitude (0 0.5 0);
omega 0.049087;

    }
}
```